Doctoral Dissertation

Fundamental Studies on New Silicides-based Accident Tolerant Fuel

[シリサイドをベースとした新しい事故耐性燃料に関する基礎研究]

Afiqa Binti Mohamad

January 2019

Division of Sustainable Energy and Environmental Engineering

Graduate School of Engineering,

Osaka University

Contents Page

Abstract

In the current light water reactors, UO_2 is used for fuels and Zr based alloys are used for cladding. For the enhancement of the tolerance to severe accidents, it is a promising way to replace Zr based alloys by another material having higher resistivity to steam oxidation and higher mechanical strength that allows fuels to keep the integrity at elevated temperature. In order to compensate for the neutronic inefficiency of advanced cladding materials, UO_2 should also be replaced by another material having higher U density. Besides, higher thermal conductivity is preferred since it will improve the heat removal efficiency when the reactor loses the coolant. Such fuel that has high tolerance to accidents is called accident-tolerant fuel (ATF). This study is intended to propose a new ATF: U-silicide fuel with Mo claddings coated with Mo silicide. In order to get a fundamental information on the candidate materials, their thermal and mechanical properties were evaluated.

Chapter 1 starts from explaining problems on fuels occurred during Fukushima Nuclear Power Plant accident. From this accident, developing ATFs has become an important issue that needs to be given attention. After reviewing the current development status of ATFs, the new ATF concept is proposed. The purpose of this study is mentioned in this chapter.

Chapter 2, the experimental methods are described. The synthesis method of the samples and the measurement techniques of thermal and mechanical properties used in this study are explained.

Chapter 3 explains the advantages of the Mo cladding and the challenge for utilizing it. While Mo has several advantages, Mo has a problem on corrosion and oxidation. This problem

can be solved by coating the outer surface of Mo cladding. As a candidate for the coating material, $MoSi_2$ is selected. The oxidation resistance of $MoSi_2$ under steam atmosphere and compatibility of $MoSi_2$-Mo are evaluated. For the compatibility, the thermal stress between $MoSi_2$ and Mo are calculated based on the physical properties.

In chapter 4, U-silicides are discussed in order to select the best U-silicide for the fuel. Since the available information on the physical properties of them is limited, the physical properties of them were measured. Among U-silicides, U_3Si_2, U_3Si, and USi_3 were selected, and dense specimens without impurities were fabricated. Next, the basic properties such as crystal structures, thermal, and mechanical properties were investigated. The measured data are compared with literature values and other compounds such as U_3Si_5 and USi. Based on the compared physical properties, one compound is chosen as the most promising fuel in the U-Si system.

Chapter 5 summarizes the proposed coating/Mo cladding/U-silicide fuel system. It is shown that the selected materials exhibit good performance in the important parameters. It is concluded that the proposed ATF has a potential as an ATF and should be studied further.

Chapter 1

Introduction

1.1 Overview of Accident Tolerant Fuel

Nuclear energy is one of the renewable energy that split the uranium atom to heat the water become a steam, then turn a turbine to generate energy. Nuclear energy emits low carbon dioxide to the environment to produce electricity and cost effective for large scale electricity; which become the second largest source of low carbon power. The first commercial nuclear power plant station started to operate was in 1950s. Nuclear energy provide 11 % of the electricity around the world. Presently, almost 16 countries rely on the nuclear power such as Sweden, Switzerland, and Japan. Previously, around 30 % of electricity come from the nuclear energy, however, after Fukushima Nuclear Power Plant Station shutdown, only 4 % of energy used for supplied electricity in Japan [1].

Recently, nuclear energy become a hot topic again around the world after Fukushima Nuclear Power Station 1F, and previously Three Mile Island severe accident. From the both accident, Zr alloy cladding fail to function at high temperature when react with the steam, and lead to the hydrogen generation, resulting of explosion. Redesign for the alternative nuclear fuel system and design become interest topic among researcher recently. Before redesign a new system and design, identify any lack or disadvantage of the current fuel design or system is necessary. The most obvious problem need to solve is more reluctant to the failure and hydrogen. A future fuel

design and system essential to be more applicable with the current fuel design and system if it will be utilizing in light water reactor (LWR).

Fukushima Nuclear Power Station 1F severe accident on March 2011 get attention around the world due to the Tsunami around magnitude 9. Even though the reactor was shut down after the accident, the decay heat still generated. The Station Blackout come along with a failure of power supply. Then, the isolation pump could not work continually and resulting in pump stop. The decay heat was continuing to produce, in addition, steam also produce in reactor pressure vessel (RPV). The liquid level in a pressure fall and core was exposed. This develop the rise in fuel clad temperature. The temperature of Zry cladding exceeds 900 ˚C, resulting clad failure and release of fission products (FP's) from rods. After 75% core was exposed, the cladding temperature exceeds 1200 ˚C and metal of Zr react with steam as follow [2]:

$$Zr+H_2O \rightarrow ZrO_2+H_2+Heat \quad (1.1)$$

From the reaction in equation 1, the heat was released and generate hydrogen as shown in equation 1.1. The produced hydrogen enters the wet well vacuum, which lead to the melting of Zry and Stainless steel (SS) at 1880 ˚C. The fuel rod disrupts at 2500 ˚C and the formation of debris

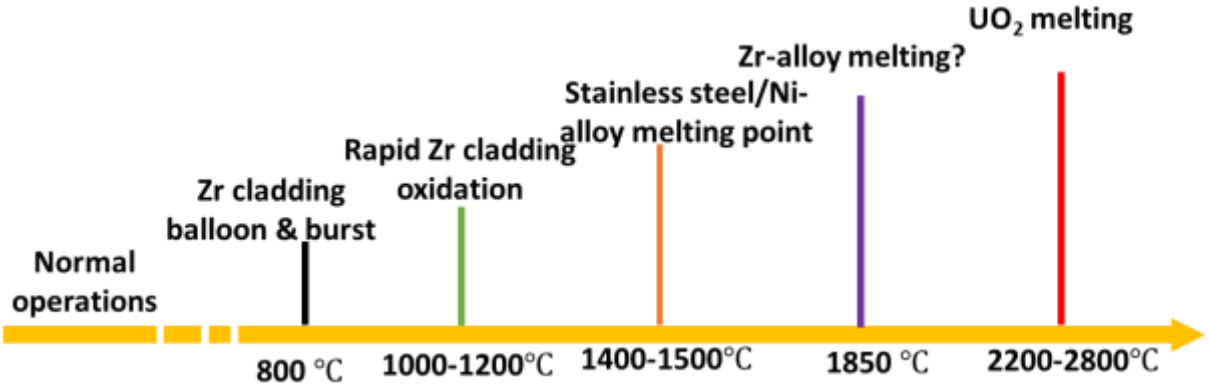

Figure 1.1 Overview of Fukushima Nuclear Power Station limited accident for LWR.

occurred. At 2700 ℃, further U-Zr melting eutectics was occurred and the core was meltdown that could cause the cladding fuel failure. Thus, the FP was released into the environment and actinide remain in the core. The general overview of the LOCA during Fukushima severe accident is shown in Figure 1.1 [3, 4].

Almost 60 years Zry-UO_2 fuel system had been used till now. After Fukushima severe accident, U.S department of energy (DOE) acknowledge there is necessary to evaluate light water reactor (LWR) and develop enhancement of accident tolerant fuel (ATF) [5]. For the ATF design fuels:

i. Nuclear power plant could be operating more "coping time" when the natural disaster (i.e., tsunami, earthquake, etc.,) occur
ii. Could be deployable to 2022
iii. Maintain or improve the reactor during normal operation

As mention above, 3 important points need to be highlight for the development of ATF.

The easiest way to enhance the accident tolerant fuel is make a minor modification to the current cladding and fuel system such as coating on Zry cladding with excellent oxidation resistance at high temperature. Even though in the ATF program, enhance the cladding Zry with coating other material one of the solution, the dramatic improvement could be difficult. This is due to the formation of hydride on Zr lead to degeneration of Zry toughness; which restrain fuel time period life as well as affect the loss of coolant accident (LOCA), reactivity initiated accident (RIA), and emergency core cooling system (ECCS). Thus, there are a few scenarios have been approach for the development of the fuel-cladding with enhance accident tolerant fuel [6];

i. Modified Zr-alloy with coating layer that could improve the oxidation resistance

ii. Replace Zry cladding with an alternative material that own high oxidation resistance in high temperature steam

iii. Improve or change with better performance of fuel

iv. Keep the security of fuel under regular operation of light water reactor (LWR)

v. Interrupt the fission products release and fuel failure under off-normal operation

vi. Retain acceptable strength to maintain the fuel design

ATF concepts goal to reduce the oxidation rate at high temperature and interrupt the ballooning and burst of the cladding material, also increase coping time to fuel melt. So that, the burden on the reactor safety structure could be reduce and manage during acknowledge the accident. A new fuel system should support safety margins and conceivably to prevent core deterioration under beyond design basis accident scenario (BDBA).

1.2 Alternative Candidates for ATF

Firstly, in the ATF program, the general approach are (i) strength the current Zry with improve the oxidation resistance of Zry by coating (ii) replacement of the Zr alloy cladding with better materials that possess excellent oxidation rate at high temperature (iii) alternative fuel forms [6].

The uncomplicated way to enhance accident of the cladding are (i) improve current material performance and oxidation kinetics with coating or (ii) Utilize other than Zr alloy with high performance of oxidation resistance under steam atmosphere [7]. For the alternative cladding material, there are many candidates for the advanced cladding materials that showed excellent/good oxidation rate to steam at high temperature such as FeCrAl, refractory alloy (Mo, Nb, W and etc.,), stainless steel based alloys, and Silicon carbide (SiC) [3, 8, 9]. The natural forming surface protective coating such as Al_2O_3 (2345 K) [10], Cr_2O_3 (2708 K) [11] and SiO_2 (1983 K) [12] own high melting point which the main reason why the state candidates become the alternative candidates. The most important is these candidates could tolerate the oxidation resistance better than Zry under steam atmosphere at high temperature or could reduce heating and hydrogen generation rates.

For the fuel, the main focus on the material that could enhance the ability and extent the release of fission product. Generally, the low thermal conductivity of UO_2 also become problem in the nuclear reactor system during the accident. Thus, for the alternative fuels, high thermal conductivity of fuel become the preference. So far, metallic uranium become the most favourable candidates for substitute current fuel, UO_2. In addition, high enrichment of uranium materials also

become the essential parameter for the candidates which give significant advantage in term of economy.

Table 1 Cladding and fuel materials that become the candidates for the accident tolerant fuel, ATF.

Cladding	**Fuel**
FeCrAl	Metallic uranium
SiC	UO_2 graphene
Refractory alloy	Micro encapsulated
Cr-coated	UO_2 composite
MAX phase	

Come out with the ATF program, the nuclear authority members hope the safety and economy of the nuclear power plant will be improved. Despite, many concepts and material candidates have been introduced for the ATF, there is no specific concept that decided will utilize for the light water reactor. What the most important for this program among nuclear researchers and authority, call attention to select the most practical use candidate of ATF in LWR after bring to successful conclusion a common understanding for each ATF candidates either for the fuel or cladding material. Thus elucidate the basic properties for the selected candidates become the most important step before decide the actual concept. The details of the candidates for the cladding and fuel materials will be explained in the Chapter 3 and 4.

1.3 Proposal for the new ATF concepts

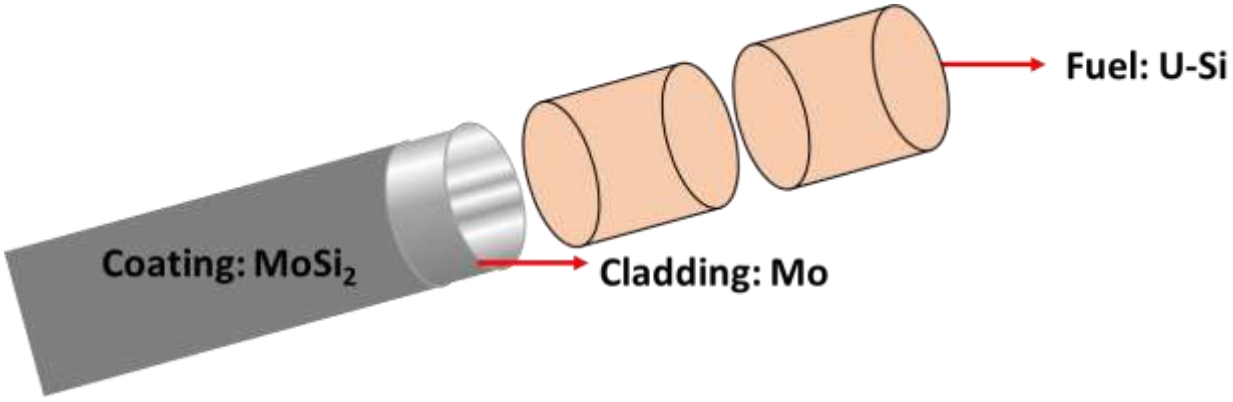

Figure 1.2 New concept of coating/cladding/fuel for the accident tolerant fuel.

In the term of enhance accident tolerant fuel, the Zry cladding should be replace with better oxidation resistance material and good mechanical properties candidate material. Recently, advanced cladding of SiC and FeCrAl attract attention among researchers. However, there is not many evaluation has been made on the advanced cladding of Mo. Thus, in the present study, we would like to select Mo as one of the ATF cladding candidate, for replacement current cladding material, Zircaloy. Even though Mo own excellent mechanical properties, Mo could react with the steam. To solve this problem, the approach we consider in the present study is try to coating outer surface of Mo cladding with the $MoSi_2$ material.

$MoSi_2$ own excellent oxidation resistance at high temperature and high melting point. The second problem of Mo if compared with Zry, own high neutron absorption value. Thus, the cladding thickness should be very thin to allow efficient neutronic. A higher uranium density of fuel is necessary to compensate the neutronic efficiency of Mo cladding. U-Si system material was

selected due to exhibit great thermal conductivity and uranium density if compared with that present UO_2.

In the present study, like shown in Figure 1.2, $MoSi_2$ was selected as an outer surface coating material; Mo as a cladding material; and U-Si system as fuel material. The details of the reason why each material were chosen will be explained in the Chapter 3 and 4. Thus, in the present study we would like to propose a new material system that could be considered as ATF candidates. The main purpose in the present study are:

(i) Evaluate the concept introduce in the present study (Fig. 3) could be considered or not for the alternative concept of accident tolerant fuel

(ii) Carry out characterization of basic properties such as thermal and mechanical properties for each materials part (coating/cladding/fuel) in the introduce concept

(iii) Determine and evaluate the important parameter such as thermal stress, oxidation resistance and thermal conductivity that necessary to utilize this concept in the future

Analyses were carried out to contribute preliminary insight into the alternative fuel-cladding concepts for the light water reactor. This is allowing researchers to evaluate the fuel performance and efficiency. Despite numerous alternate fuel-clad matters have been evaluated as accident tolerant fuel candidates' concept, in this study we would like to focusses on specific $MoSi_2$ coating, Mo-based alloy cladding, and U-Si fuel options. From the results, we will conclude either the suggested concept could be considered in the future nuclear reactor. The details of the results on Mo cladding and $MoSi_2$ coating will be explained in the Chapter 3, and investigation on the basic properties of U-Si system compounds will be explained in the Chapter 4.

The properties of each proposed materials are crucial for the evaluation of the effectiveness of coating/cladding/fuel system on the fuel performance of the light water reactors. The obtained data from the measurement will allow to design or modelling the future system fuel.

Chapter 2
Experimental methods and analyses

In the present study, the specimens of $MoSi_2$ and U-Si compounds were made solid state reaction using arc-melting and then synthesize used spark plasma sintering. To make sure the ingot obtained after the sintering, the specimens were annealed at selected temperature for 72 h.

The characterization of each specimen was carried out as:

i. X-ray diffraction analysis (XRD) to analyse crystal structure and phase
ii. Mechanical properties: Sound alarm and Vickers hardness
iii. Thermal property: Physical Property Measurement System, Differential Scanning Calorimetry, Dilatometer, Laser Flash method

The details of the analysis methods state in (i) to (iii) will be explained as below:

2.1 Sample preparation

2.1.1 Arc-melting

Arc melting is a furnace where heat is produced by means of electrical arcing for melting certain metal without changing electro-chemical properties of metal. Electric is produced through electrode as shown in Figure 2.1. The electric is used for melting the metal. The current flows from cathode to anode for the Direct current arc melting furnace. This furnace has only a single graphite electrode at the bottom of the furnace.

During the meltdown period, the electrodes are moved down onto the scrap. Then arc is produced between the electrode and metal. By considering the evaporation of specimens, low voltage is selected. After the arc is shielded by electrodes, the voltage output is increased for speeding up the melting process.

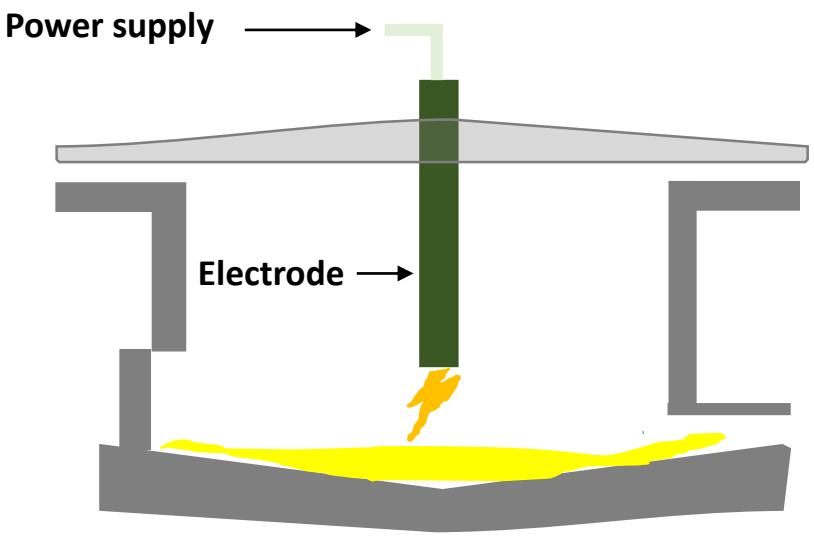

Figure 2.1 Schematic diagram of arc melting process.

2.1.2 Spark Plasma Sintering

Spark plasma sintering (SPS) is a direct heating to the powder under melting temperature. A simultaneous temperature and pressure were applied during sintering to allow a diffusion of atoms. First, the electric current produced contact with the powder and generate electric charge. The joule heating generates from the current loss at grain boundaries diffuse through the powder particles and strengthen the structure densification. As shown in the Figure 2.1, the pulse current flowing through the centre of the pressed powder and that flowing is larger at the surface powders compare to other parts. The direct heating on the powder allows high heating rate and cooling which improve the densification of the specimen. In addition, holding time, applied pressure and particle size of the starting materials are also become the important parameter need to be consider to achieve high relative density of specimen.

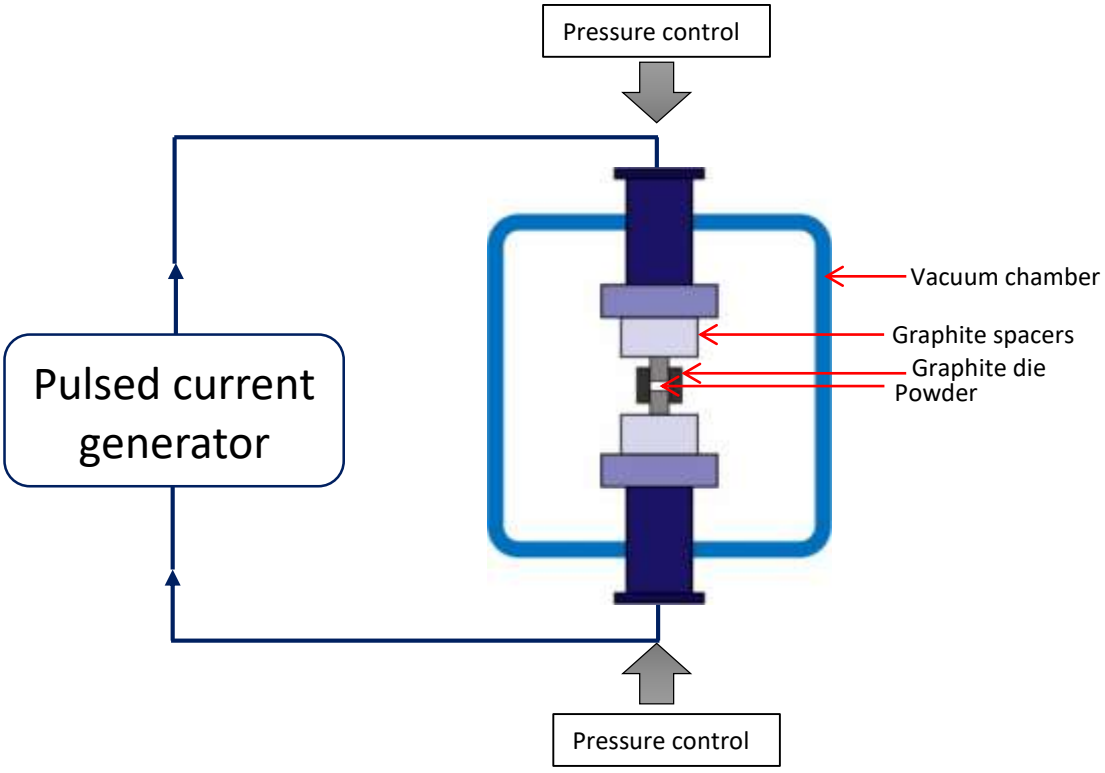

Figure 2.2 Schematic diagram of specimen during synthesized in Spark plasma sintering.

2.2 Characterization methods

2.2.1 X-ray diffraction (XRD)

Phase identification was identified using X-ray diffraction (XRD) analysis. The specimens were determined in powder/bulk and the analysis was carried out. X-ray was generated by cathode X-ray tube by heating a filament and produced electron. Applied voltage will accelerate the produced electron and attack the target material. After gain sufficient energy, electron will replace inner shell of target material. The characteristic X-ray spectra will be produced. Generally the spectra exhibit κ_α and κ_β spectra. Semiconductor detector such as Cu, Fe, Mo will use for the X-ray diffraction. Cu κ_α rad=1.5418 Å.

When the sample and detector rotated, the intensity will record. The interaction of incident law and sample produced constructive interference ad diffracted ray called as Bragg's Law. The equation of Bragg's Law can be expressed as:

$$n\lambda = 2dSin\theta \tag{2.1}$$

where λ is the wavelength, and d is the lattice spacing. The schematic diagram of Bragg's Law was shown like in the Figure 2.2.

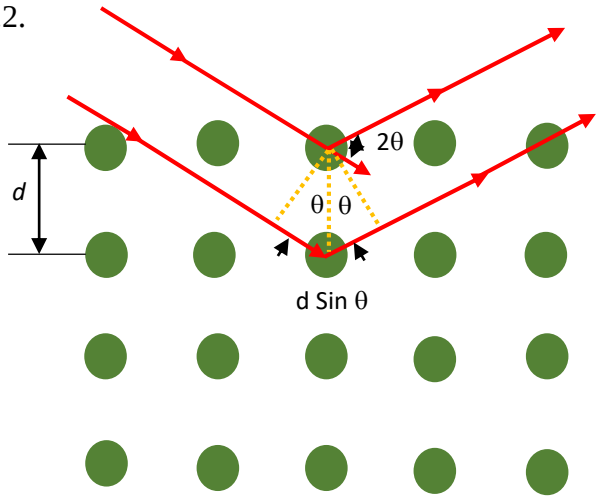

Figure 2.3 Schematic diagram of the Bragg's Law.

2.2.2 Sound velocity

Sound wave can produce 4 modes based on the method of particles oscillate. The 4 modes are longitudinal sound wave, shear sound wave, surface sound wave, and plate sound wave. In ultrasonic testing, longitudinal sound wave and shear sound wave are generally produced. The longitudinal sound wave and shear sound wave of particle movement is shown in the Figure 2.3. The wavelength, λ can be determined from the movement of the sound wave from the peak to peak. The sound wavelength is vice versa proportionate to the frequency.

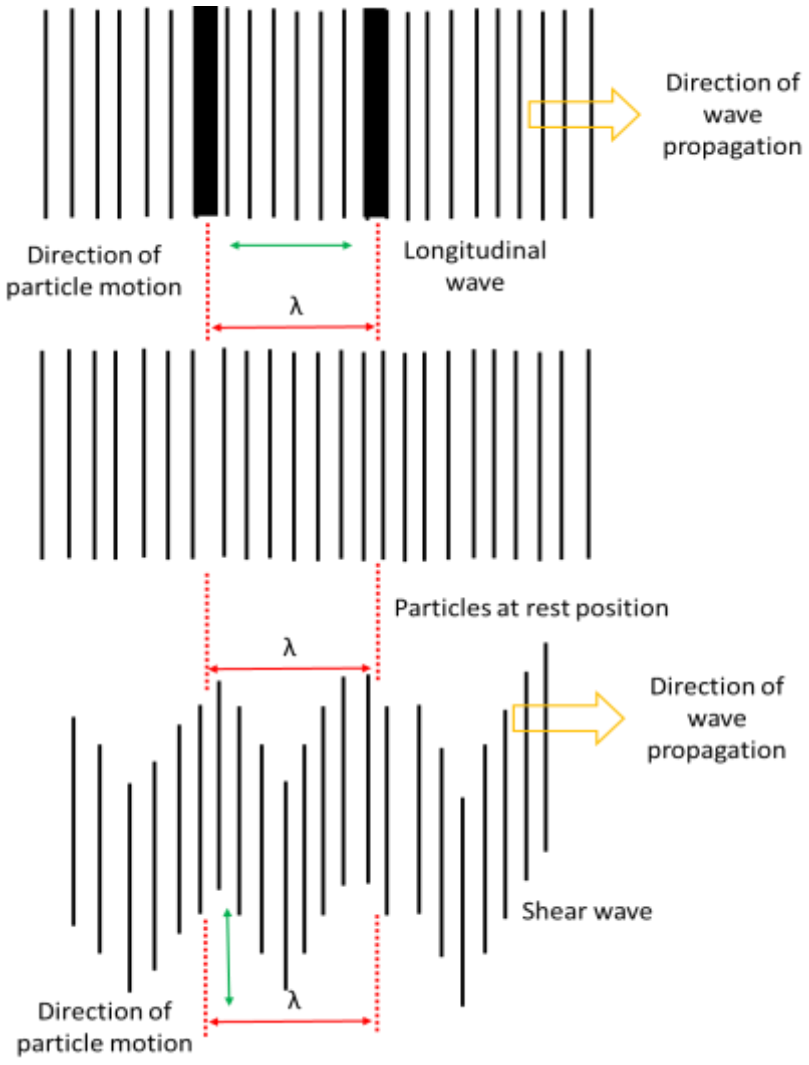

Figure 2.4 Schematic diagram sound wave principle.

Ultrasonic waves are produced when pass through a straight line with consistent speed until lay into surface. The wave energy will reflect and transmitted when lay on the material surface, which the info about size of reflector can be known. From this, the travel time and distance of sound movement can be deliberate.

In pulse echo examination as shown in the Figure 2.4, a transducer sends out a pulse of energy and the same or second transducer listens for reflector energy. Reflection occur due to the presence of discontinuous and the surface. The info regarding the size and position of the reflect sound can be understanding from the reflected wave energy which is presented against time. The longitudinal and transverse sound wave velocity are written as:

$$v_L = \frac{2L}{t_2 - t_1} \tag{2.2}$$

$$v_s = [(\frac{t_3 - t_2}{D})^{1/2} + (\frac{t_2 - t_1}{2L})^{1/2}]^{-1/2} \tag{2.3}$$

where D is the specimen diameter, L is the specimen length, t_1 is the reflection time for the longitudinal wave velocity from the inferior surface of the specimen, t_2 is the reflection time for the longitudinal wave velocity from the uppermost surface of the specimen, and t_3 is the reflection time for the shear wave velocity from the uppermost surface of the specimen.

The elastic modulus and Debye temperature can be evaluated from the longitudinal (V_l) and shear wave velocity (V_s) values. The longitudinal wave velocity (V_L) and shear wave velocity (V_S) were determined, and then the elastic constants were evaluated as below:

$$G = \rho V_S^2 \tag{2.4}$$

$$E = \frac{G(3V_L^2 - 4V_S^2)}{(V_L^2 - V_S^2)} \tag{2.5}$$

$$B = d(V_L^2 - \frac{4}{3}V_S^2) \tag{2.6}$$

$$\nu = \frac{1}{2}\frac{V_L^2 - 2V_S^2}{V_L^2 - V_S^2} \tag{2.7}$$

$$V_m = \left[\frac{1}{3}(\frac{2}{V_S^3} + \frac{1}{V_L{}^3})\right]^{-1/3} \tag{2.8}$$

$$\theta_D = \frac{h}{k_B}\left[\frac{3n}{4\pi}(\frac{N_A\rho}{M})\right]^{1/3} V_m \tag{2.9}$$

h is the Planck constant, k is the Boltzmann's constant, N_A is the Avogadro's number, d is the measured density, n is the number of atoms in the molecule, and M is the molecular weight.

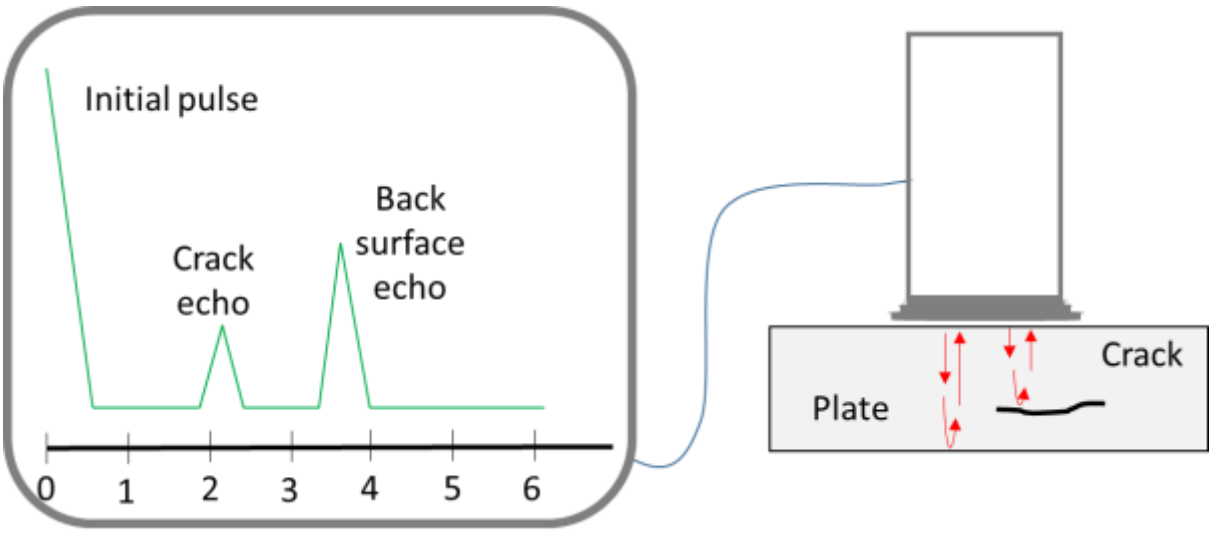

Figure 2.5 Schematic diagram of pulse echo examination.

2.2.3 Hardness

Hardness is a test to determine the material resistance by measuring the depth of the indentation. the pyramid diamond indenter was used in the present study. Generally, the Vickers angle is 136˚ which form a diamond shape indent. First, the indenter is pushed into the specimen surface by test force. The test force used was 9.8 N and 49 N. The force is maintained for the 10 seconds. After the indenter is removed, the appears diamond shape formed on the surface. The size of the indent was determined suing laser microscopy. The image of the shape indenter on the specimen surface was shown in the Figure 2.5. The average of the two diagonals (*d*1, *d*2) are used to determine the Vickers hardness.

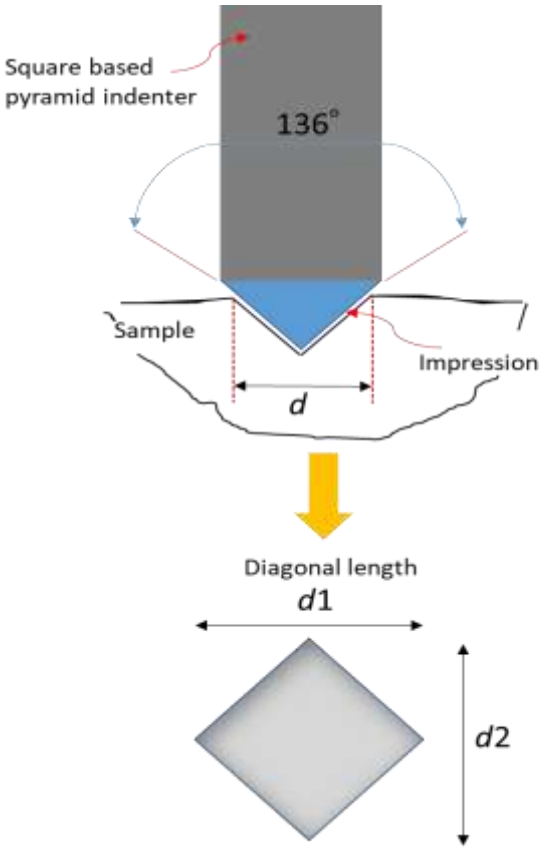

Figure 2.6 Schematic diagram of basic principle of Vickers hardness.

2.2.4 Thermal diffusivity

Thermal diffusivity (D) is used to determine a material transfer heat and react to the changes in temperature. thermal diffusivity is a ratio how much the heat stored in the specimen. Likewise, thermal conductivity (λ), also describe how much the heat is transferred through a specimen due to the temperature gradient. The thermal conductivity can be determined from a relationship of the specific heat capacity (C_p), density (ρ), and thermal diffusivity (D).

Thermal diffusivity often measured by laser flash analysis as shown in the Figure 2.6 (a, b). In this technique, a sample is heated on one side by pulsing it with a laser inducing a temperature gradient which is then measured with respect to time. A laser with power around 15 joules per pulse provides energy pulse to the bottom face of the sample. An infrared detector above the upper surface of the sample registers the change in temperature with time after each laser pulse. From the thickness of the specimen and time function that characterize the procreation of the heat release from the front face to the back face. The thermal diffusivity can be estimated as below:

$$D = 0.1388 * \frac{d^2}{t_{1/2}} \tag{2.10}$$

(a)

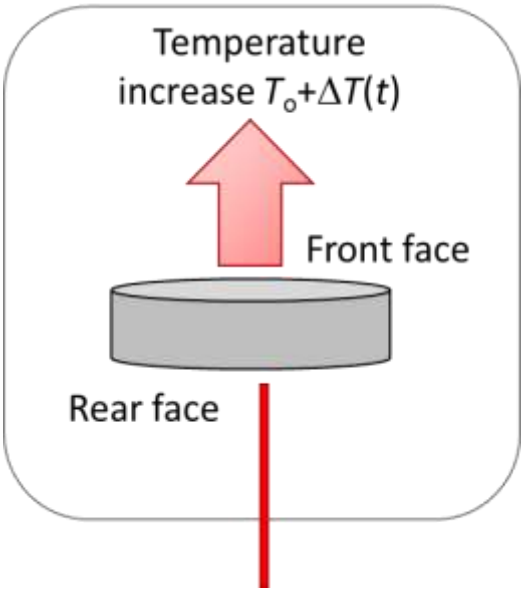

(b)

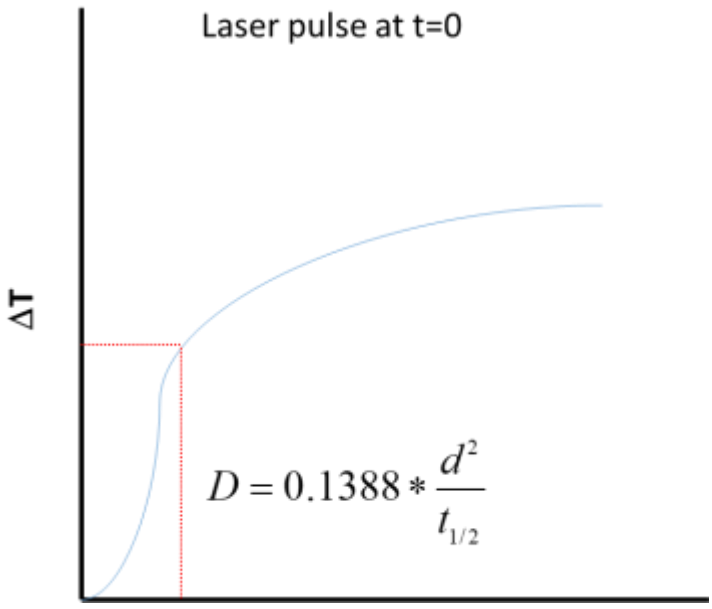

Figure 2.7 (a) Schematic diagram of laser flash principle. **(b)** Schematic diagram of common produced curve from the laser flash.

2.2.5 Physical Property Measurement Spectrum (PPMS)

Physical Property Measurement Spectrum (PPMS) is a device to measure heat capacity or thermal properties at low temperature as shown in the Figure 2.7. In the present study, the PPMS was used to measure the heat capacity at low temperature. The measured temperature was varied from 1.9 K to 300 K. The heat capacity was determined at constant pressure, C_p. The Quantum Design Heat Capacity used relaxation method. This method combines the measurement accuracy with robust analysis technique.

For the analysis, during the measurement, the specimen and specimen platform contact are in acceptable connection. The equation for the specific heat capacity from PPMS is determined as:

$$C_{\text{total}} \frac{dT}{dt} = -K_w(T - T_b) + P(t) \tag{2.11}$$

where K_w is the heat transfer though the connection wire, T_b is the thermal batch temperature, and P_t is the power supplied for the heater.

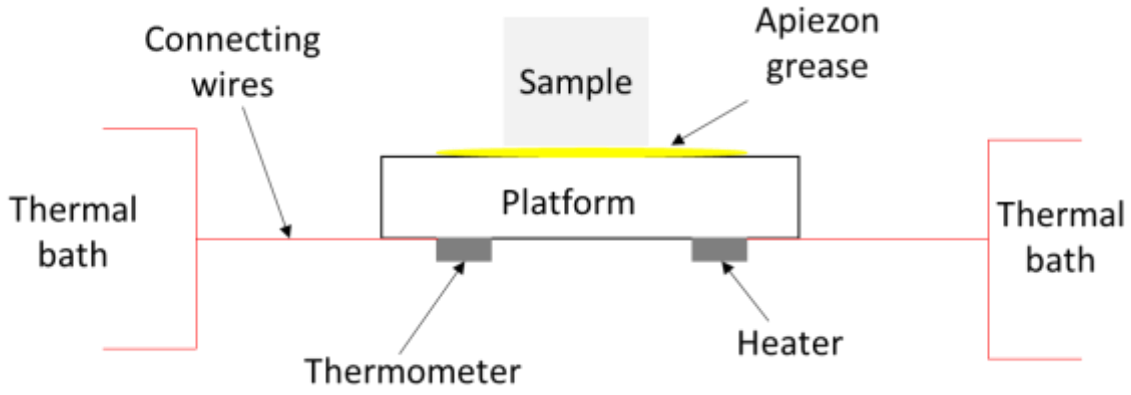

Figure 2.8 Schematic diagram of PPMS instrument.

2.2.6 Differential Scanning Calorimetry (DSC)

Differential scanning calorimetry (DSC) is a technique to regulate an inequality of the quantity of heat necessary to gain the temperature of the specimen together with reference sample. The schematic diagram of the DSC as shown in the Figure 2.8. Generally, the blank crucible as a baseline (Al_2O_3), crucible contained sapphire for the reference and prepared specimen were fixed at same temperature range under constant Argon flow. High purity of Ar was flowing at rate 30 mL/min. The energy change of blank crucible and crucible contained sapphire were recorded for the analysis. The DSC device produced elaborated heat flows for the specimens and reference sample of sapphire. The elaborated values were obtained by subtracting both values from the blank crucible. The specific heat capacity of measured specimens are written as:

$$Cp = \frac{m_{sapphire}}{m_{sample}} \times \frac{H_{sample}}{H_{sapphire}} \times C_{p,sapphire} \tag{2.12}$$

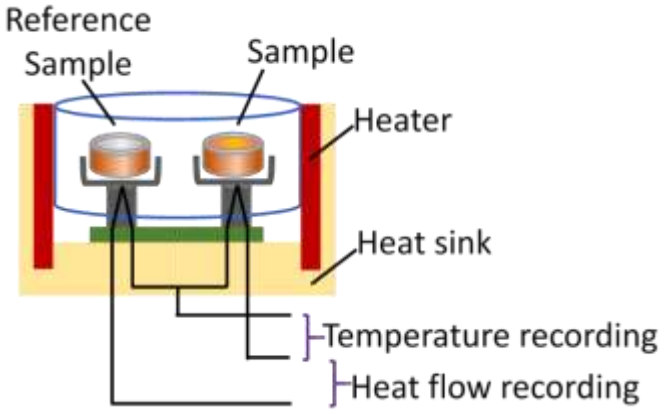

Figure 2.9 Schematic diagram of DSC instrument with the illusion of specimen and reference sample.

2.2.7 Dilatometer

Dilatometer is a thermos-analytical technique to measure the expansion of materials during heating or cooling. For the analysis, as shown in the Figure 2.9 (a) the specimen and alumina reference were placed directly against the push-rod. The sample length change based on the temperature setting transmit the change values to the linear variable displacement transducer. The temperature is command by thermocouple. The measured length change was included by the length change of the holder and specimen. The measurement is corrected by the alumina reference sample. The coefficient of thermal expansion is determined by:

$$\alpha_1 = \frac{1}{L_0}\frac{(L - L_0)}{(T - T_0)} \tag{2.13}$$

where L_O is the initial length at initial temperature T_O, and L is the length change due to the specimen expand at change temperature T. The schematic diagram of the length change as a function of temperature is shown like in the Figure 2.9 (b).

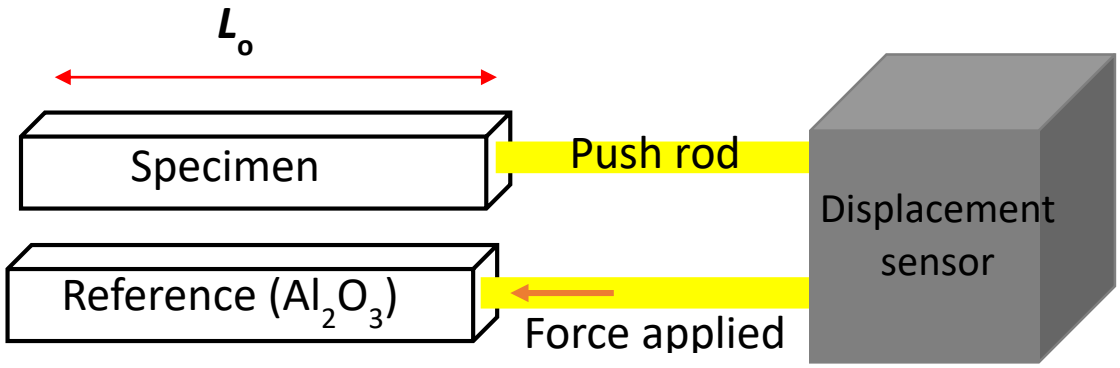

Figure 2.10 Schematic diagram of (a) dilatometer device.

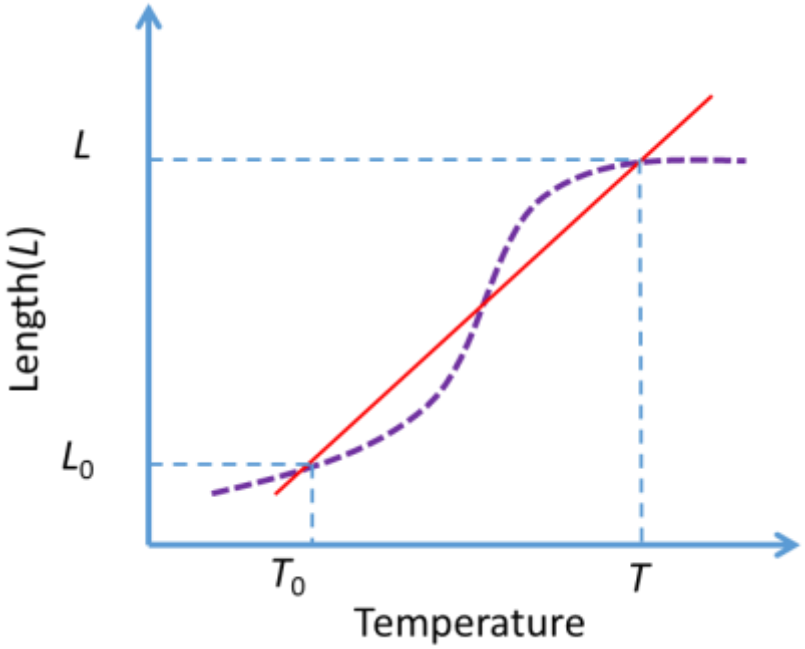

Figure 2.10 (b) Length change to determine thermal expansion coefficient.

2.2.8 Thermogravimetry(TG) and Differential Thermal Analysis(DTA)

Thermogravimetry (TG) and differential thermal analysis (DTA) could be measured simultaneously by TG-DTA analysis. TG is a method to evaluate the oxidation, evaporation, or decomposition of the specimens with due to the temperature change effects. The mass change can be either mass gain or mass lost to evaluate what kind of phenomena occurred on the prepare specimen under constant atmosphere and controlled temperature. In the Figure 2.10, the beams for the specimen and reference (Al_2O_3) are placed in a furnace. The mass change of the specimen and Al_2O_3 powders are measured by sensitivity-calibrated drive coils separately. The TG signal is used to send the signal for the mass change. The heat amount released or absorbed can be evaluate by DTA. The technique used for DTA analysis by evaluate the difference in temperature between specimen and reference specimen.

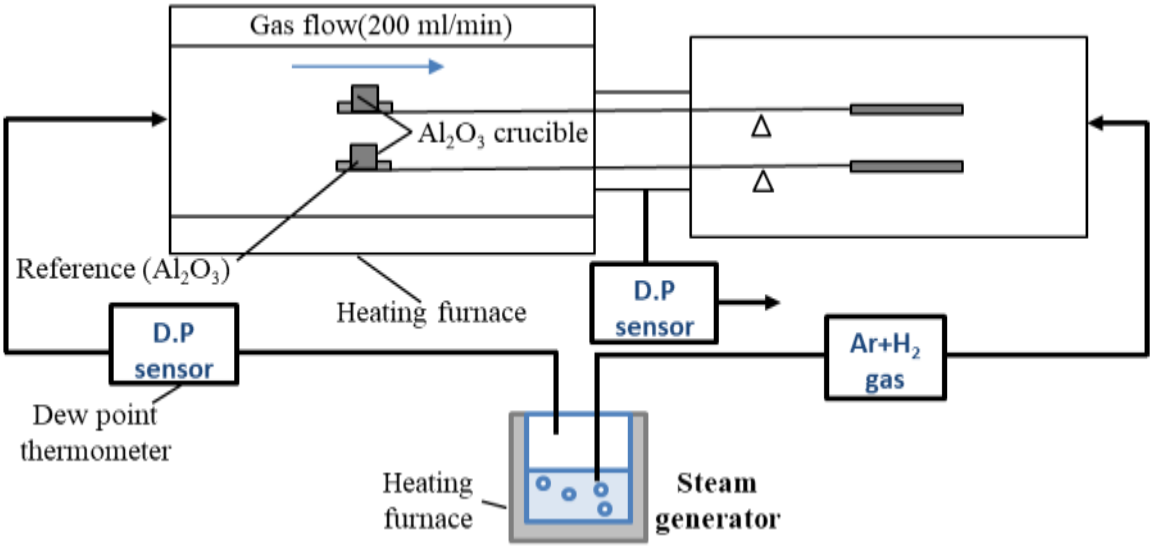

Figure 2.11 Schematic diagram of TG analysis equipped with the steam generator.

Chapter 3

Coating on the Mo cladding

3.1 Advanced cladding material candidates

The incentive for develop advanced new cladding materials is significantly focus on reducing the load on the emergency core cooling system (ECCS) during the severe accident as happen during Fukushima Nuclear Power Station, 1F especially reduce the oxidation rate and heat generated from cladding in steam atmosphere at high temperature. In the accident tolerant fuel (ATF) program, looking for the new material that better than current cladding Zircaloy (Zry) at high temperature T>1200℃ in steam atmosphere become the main interest among nuclear researcher. Others parameters will be considered for the advanced cladding materials candidates are:

i. Excellent temperature properties
   - High melting temperature
   - Good oxidation resistance in steam atmosphere at 1200~1500 ℃
   - Acceptable cladding tensile and creep strength at 1200~1500 ℃

ii. Reasonable economics
   - Acceptable neutronic absorption cross-sections
   - The cost for the materials is reasonable

iii. Fabricable into fuel length cladding tubes
   - Applied for airtight sealed

iv. Adaptable with current light water reactor (LWR) designs and coolant system

v. Good fuel safety under normal operations

vi. No fuel storage and disposal issues

There are several candidates have been considered to replace Zr alloy cladding materials, due to own high oxidation resistance in high temperature steam or air atmosphere. Silicon carbide (SiC), refractory alloy (Mo, W, Nb., etc), iron chromium alloy (FeCrAl), Cr-coated Zry, and Stainless steel (SUS) [13, 14]. Each of these candidates was obtained numerous scale of benefit and challenging to utilize it. The details of the characteristics for each candidate are explained as below;

(i) Iron chromium alloy (FeCrAl)

FeCrAl mainly consists of iron, Chromium (Cr, 10~15 wt %), and Aluminum (Al, 3~6 wt %). No phase transformation suggested from liquidus temperature (~1723 K) [15] to room temperature due to the strong body-cantered-cubic structure, BCC. Due to the protective layer of aluminium oxide, Al_2O_3, FeCrAl showing superior oxidation resistance to steam at high temperature [16, 17]. A high neutron absorption cross-section, which is 10 times higher than Zry would be figure out by reduce the thickness to makeup the neutronic penalty. Historically, it was proved from the stainless steel used in light water reactor [18]. On the other hand, a good mechanical property such as high stiffness [19] and yield stress [20] make FeCrAl leading as an alternative cladding candidate.

(ii) SiC composite

Ceramic based Silicon carbide, SiC has high sublimation temperature almost 2973 K and could endure temperature to 2773 K. SiC had been used in highly demanding in the application of

the commercial jet engine [21]. On the other hand, in the nuclear technology production, SiC had not develop yet. Just recently, due to the SiC owing excellent oxidation resistance up to 1973 K under steam atmosphere [22], SiC has been consider as an alternative clad material. However, the disadvantage of SiC is brittle behaviour; which need to improve strength and toughness for the fabrication. The neutron absorption cross-sectional of SiC is 0.09 (shown in Table 3.1) which is lower than Zry. Thermal conductivity of SiC almost same with Zr alloy.

(iii) Refractory alloys-Mo

Refractory alloy one of the new generation of the alternative cladding material also become another optional for the fuel-clad alternate material. Refractory alloy such as Mo and Nb could service up to 1123 K and the melting temperature above 2123 K as shown in Table 3.1. It has been reported that Mo obtain superior creep resistance and possess foremost mechanical strength at high temperature [23, 24]. This material become challenging for utilize as a cladding material, due to the neutron absorption cross-section value was higher than Zr. Historically, Strasser had reported a high neutron absorption of the cladding material could overcome with thinner cladding [18]. In addition, Mo has low oxidation resistance with acceptable radiation embrittlement which cause the difficulties in fabrication [14, 25]. On the other hand, Mo has good mechanical behaviour at high temperature [26] (shown in Figure 3.1) and high thermal conductivity (shown in Table 3.1).

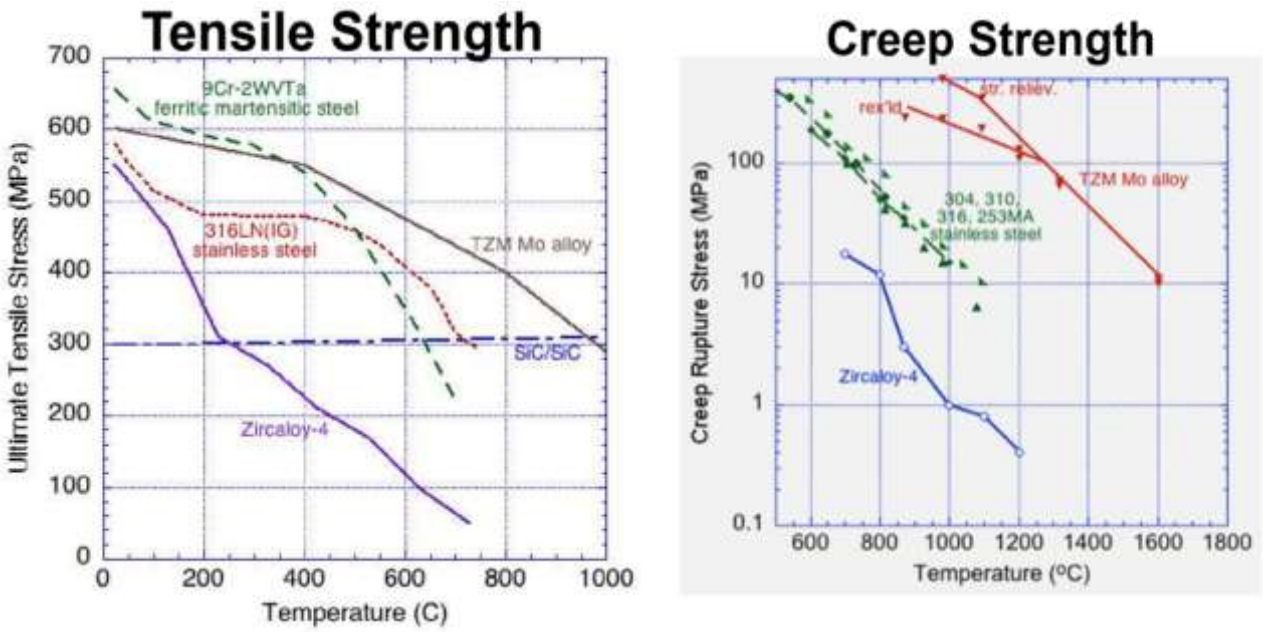

Figure 3.1 Tensile strength and creep strength of Mo with other cladding candidate's dependence with temperature.

Table 3.1 Melting temperature, neutron absorption cross-section, and thermal conductivity of the Zr with candidates of the cladding material.

Material	Melting temperature/K	Neutron absorption cross-section/barns	Thermal conductivity/$Wm^{-1}K^{-1}$
Zr alloys	~2073	~0.19	22
Austenitic stainless steel	~1673	~2.6-2.8	16
Inconel/Ni alloy	~1673	~4.0-4.2	-
Iron-Chromium-Aluminum	~1813	~1.9	22
SiC	2973	0.09	20
Mo alloys	2896	2.6	138
Nb	2750	1.15	53
ZrO_2	2988	-	2

As explained above, each of these candidates own their own advantages and disadvantages. In the present study, the first proposal is replacement of the Zr cladding with the Mo. Mo alloys has unique properties especially excellent mechanical properties at high temperature as well as high melting point compared to others candidate, however, there are a few challenges for the LWR application such as easy to react with oxygen or water [14]. On the other hand, there is lack of data on the embrittlement under irradiation and industry infrastructure not well establish. Thus, in this study the focal point is on how to resolve the reaction of Mo with water or steam by the coating on the outer surface. The details about the coating material on the Mo cladding will be explained in the section 3.2.

3.2 Coating of $MoSi_2$ on Mo-Purpose

As explained in the 3.1, one of the disadvantage of Mo is it would be reacting with oxygen/steam [14] which undesired as cladding material. One of the approach to solve this problem is coated the outer surface of Mo cladding with a material that extend with steam at high temperature. The criteria for the coating material should own:

i. Low oxidation rate
ii. High melting point
iii. Minimum differences of mechanical property with Molybdenum
iv. High eutectic formation temperature with Molybdenum

The initial step of the coating materials is investigating the oxidation rate of selected materials under steam atmosphere and evaluate the compatibility of the coating materials with the cladding. Thus, $MoSi_2$ is selected as a coating material on the Mo cladding. The schematic diagram of the $MoSi_2$ coating on the external surface layer on the Mo cladding is shown in the Figure 3.2. The interest and use of $MoSi_2$ as a high temperature material has received attention in recent year [27-29]. $MoSi_2$ exist between borderline ceramic and intermetallic compound for high temperature structural, thus exhibits ceramic like and metal like properties. Due to the excellent oxidation resistance at high temperature, $MoSi_2$ has been utilize widely in the application of industrial (furnace, power generator components, gas burners, and etc.,), aerospace (turbine aircraft, blades, nozzles, and etc.,) and automotive (turbocharger rotors, turbine engine parts, and etc.,). $MoSi_2$ own high melting point up to 2010 $^{\circ}C$, and excellent resistance to oxidation as the creation of SiO_2 as a possessive layer which a melting point of 1710 $^{\circ}C$. In addition, $MoSi_2$ exhibit good electrical

resistivity and thermodynamically stable, and brittle to ductile transition. Generally, $MoSi_2$ is abundant material, economically low cost, and non-toxic which is environmental friendly.

The goal of these studies are to classify the corrosion resistance of the Mo with $MoSi_2$. First, to evaluate the oxidation resistance of $MoSi_2$, thermogravimetric analysis will carried out in Ar and steam atmosphere at 1100℃. These conditions were selected to resemble the coolant chemistry of light water reactor under off-normal operations. Resistance of material to high temperature oxidation in steam become important key material performance to evaluate the successful of light water reactor (LWR). So far, there is no report or data that concern about the analysis of $MoSi_2$ under steam atmosphere. The detail of this experiments will be explained in details in the Session 3.3. Second, the basic properties such as thermal and mechanical properties of $MoSi_2$ will be evaluated to determine the thermal stress between Mo and $MoSi_2$. Thermal stress one of the important parameter to evaluate the interaction between the coating and cladding material. The oxidation resistance of $MoSi_2$ with various atmosphere will be explained in the Session 3.3, while thermal stress evaluation in the Session 3.4.

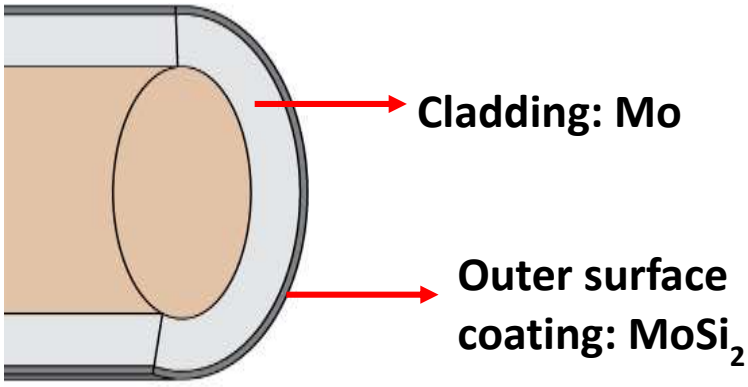

Figure 3.2 Schematic diagram of the $MoSi_2$ coating on the external surface layer of the Mo cladding.

3.3 Oxidation resistance of $MoSi_2$

In this session, the oxidation resistance of $MoSi_2$ will be evaluate with various atmosphere at 1100℃ using thermogravimetric analysis. The obtained data will be compared with the available reports regarding a same analysis on Mo and Zry at high temperature [14].

3.3.1 Experimental method and analysis

Molybdenum silicide, $MoSi_2$ powder (Kojundo Chemical Laboratory Co., Ltd) with a purity of 99.9%. The average of particle size was found to be 5.5 μm measured by laser diffraction method while crystallite size was larger than 200 nm determined from the broaden of XRD peak. The pellet was formed using cold-pressed. The pressure of 100 MPa was applied and hold for 30 minutes. The preparation of sample was carried out in the glove box with Nitrogen flow.

Thermogravimetric and differential thermal analysis (TG-DTA) was carried out using equipment commercial by STLab. Co., Ltd. The schematic diagram of the TG-DTA analysis apparatus was shown in the Figure 3.3. The condition of temperature and atmosphere were shown in the schematic diagram shown in the Figure 3.4. For the steam atmosphere, steam was introduced after 373 K to 1373 K. Al_2O_3 was used as a reference material for the analysis. The dew point is 60℃.

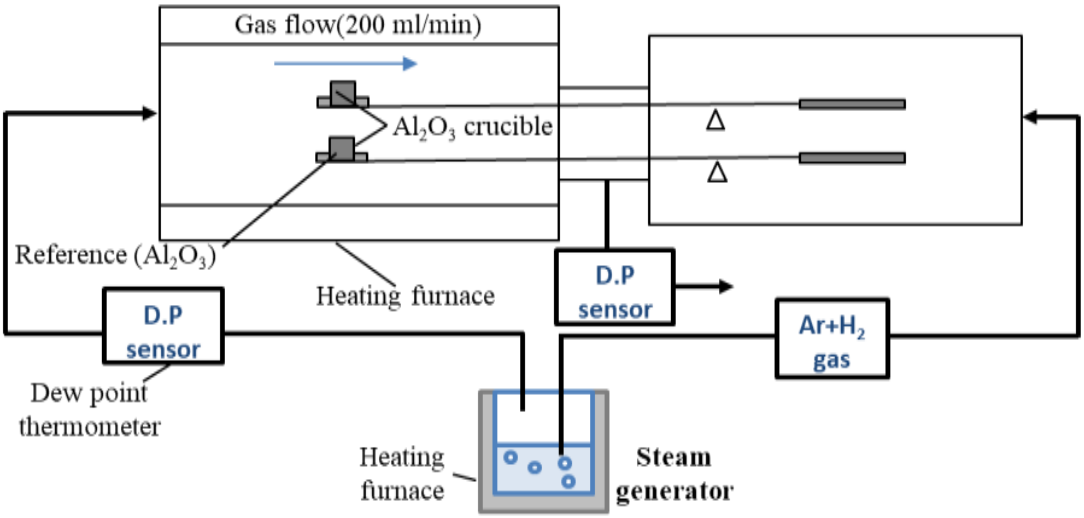

Figure 3.3 Schematic diagram of the TG-DTA device equipped with the steam generator.

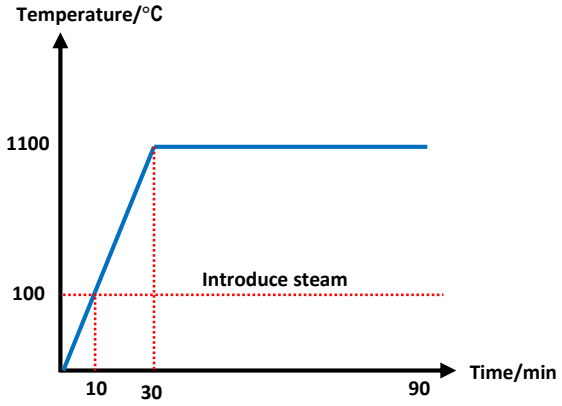

Figure 3.4 Schematic diagram of the condition for the TGA.

3.3.2 Results and discussions - Oxidation test

The results of the oxidation resistance of $MoSi_2$ are shown in the Figure 3.6. First, under Argon atmosphere, there is no mass change is observed at 1100 °C. Then, under $Ar+O_2+H_2O$ atmosphere, there is also no mass change was observed until 90 minutes. The Mo specimen that had been reported by Nelson et al. are also plotted together with the $MoSi_2$ specimen [14]. The study obtained from Nelson's discover that the mass loss was greatly observed after 20 minutes. The volatilization of Mo rapidly attains it steady state with the additional of oxygen. In addition, the oxidation test on Zry as reported from Moalem et al. discover the mass gain of Zry rapidly increase under steam atmosphere. From this results, the oxidation rate of $MoSi_2$ under steam atmosphere is better than Mo. There is no mass gain or mass loss are observed for $MoSi_2$ at 1100 °C.

Figure 3.6 show the oxide layer thickness of Zry, SiC, and FeCrAl. The prediction oxide thickness of FeCrAl and SiC are much lower than Zry, especially under normal operation. As the oxidation test of $MoSi_2$ shown in the Fig. 3.5, there is no reaction of $MoSi_2$ as well as FeCrAl. Thus, due to that, we assume $MoSi_2$ can have same scenario with the FeCrAl. In addition, the melting temperature of $MoSi_2$ is higher than FrCrAl, thus it can be more lasting than FeCrAl.

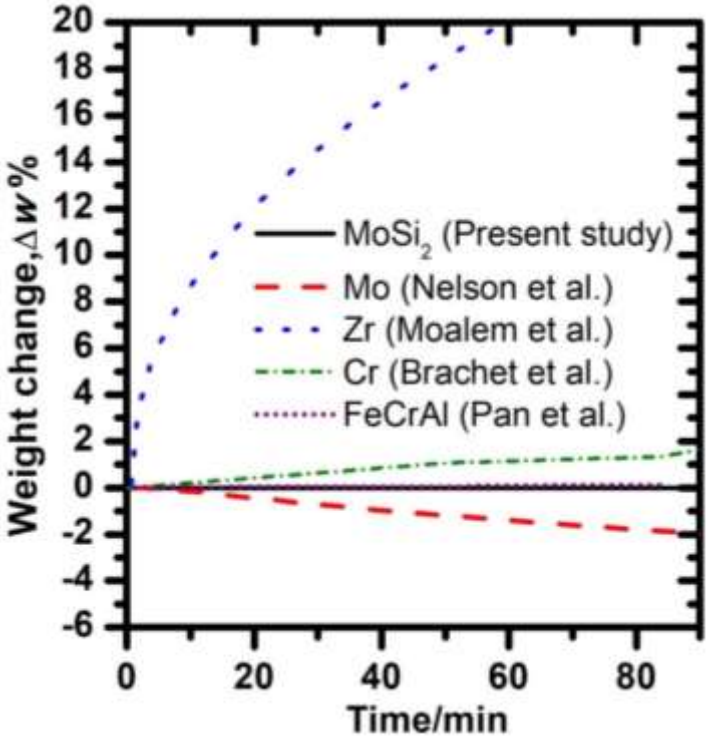

Figure 3.5 Weight change of $MoSi_2$ under steam atmosphere for 90 minutes.

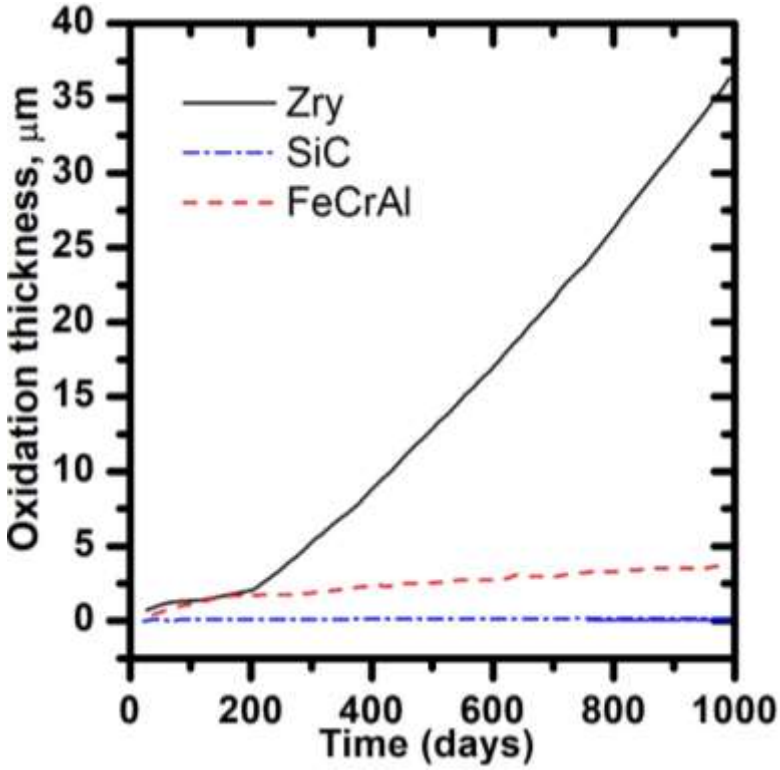

Figure 3.6 Cladding and fuel temperature during normal operation.

3.4 Thermal stress of Mo and $MoSi_2$

Thermal stress one of the important parameter to evaluate the interaction between coating-cladding material. The meaning of thermal stress is a stress formed could lead the material change in shape or size due to the change in temperature to a material. The fracture and plastic deformation of a material would be change if the stress was occurred. Thermal gradient, thermal expansion coefficient and thermal shocks are the properties that would influence the thermal stress of a materials.

In the present study, we would like to determine a thermal stress between Mo and $MoSi_2$. In order to estimate thermal stress, thermal and mechanical properties of $MoSi_2$ will be evaluated. Thermal stress, σ could be determined from the equation 3.1:

$$\sigma = E \times \alpha \times \Delta T \tag{3.1}$$

where E is the Young modulus [MPa], α is the thermal expansion coefficient [K^{-1}] and T is the temperature difference [K]. The parameter necessary for determine thermal stress between Mo and $MoSi_2$ was evaluated from the present study.

3.4.1 Experimental method and analysis

The starting materials powder used in the experiment same like explained in the section 3.3.1. The powder was sintered by spark plasma sintering (SPS) with flowing Ar using furnace (Dr. Sinter SPS-515A, Sumitomo Coal Mining Co., Ltd). The temperature condition, pressure and heating rate was shown like in the Figure 3.7. The cylindrical pellet size is 12.77x1.99 mm was obtained from the SPS. After SPS, the sample was carried out for the annealing at temperature of 1273 K for 12 h in evacuated and sealed SiO_2 tubes. This process necessary to obtained a single and stable of $MoSi_2$ phase for the evaluated other properties.

Crystal structure and phase identification were determined by X-ray diffraction (XRD) analysis using Cu K_α radiation with a Rigaku Ultima IV X-ray diffractometer equipped with a scintillation counter. A high temperature XRD was used to determine a lattice parameters dependence of the temperature. The measurement was carried out under Helium atmosphere from 300 K to 1073 K. The lattice parameter was evaluated by least square method. From the obtained lattice parameters, theoretical density could be obtained, and the measurement density was determined from the mass and volume of the pellet. Relative density was obtained by dividing theoretical density with the measurement density.

The thermal expansion coefficient was determined from (i) volume of the lattice parameters and (ii) dilatometer (Bruker AXS, TD5000SA). The dilatometer measurement was calibrated with the reference sample of Al_2O_3 from room temperature to 1500 K. The specific heat capacity of the α-$MoSi_2$ was measured using differential scanning calorimeter (DSC, Jupiter, STA 449C Netzsch) from 300 K to 1273 K. The measurement was carried out under Ar atmosphere and equipment that contain high purity and the measurement was calibrated with a sapphire standard

sample. Multiplication of the thermal diffusivity [*D*, m/s], measured specific heat capacity [Cp, J/molK^{-1}], and density [*d*, g/cm^{-3}] produced thermal conductivity of α-$MoSi_2$. Laser flash technique was used to measured thermal diffusivity using an LFA-457 (Netzsch) apparatus.

Sing around ultrasonic velocity measurement (Ultrasonic Engineering Co., Ltd UVM-2) was carried out to determine the longitudinal and shear wave velocities. Elastic constants such as Young modulus, bulk modulus, shear modulus, and Debye temperature were estimated from the obtained values of longitudinal and shear sound velocities. Hardness measurement was performed using Vickers hardness tester (Shimadzu HMW-1T) under varies load from 0.098 to 9.8 N with a measurement of 13 times for each load. A 10 s load was applied on the specimen surface.

The electrical properties such as electrical resistivity and Seebeck coefficient were measured using a ZEM3 apparatus (Advanced Riko. Inc.) under He atmosphere. A measurement was carried out using four-point current technique and DC method to determine electrical resistivity and Seebeck coefficient, respectively.

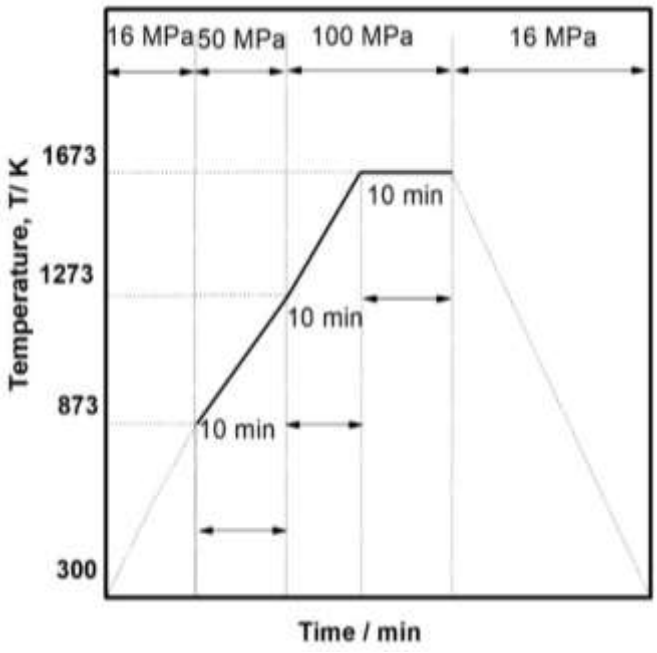

Figure 3.7 Synthesized condition to form a $MoSi_2$ pellet.

3.4.2 Results and discussion

3.4.2.1 Crystal structure

XRD patterns of the starting materials, after SPS and annealing together with reference peak from the literature are shown in the Figure 3.8. Almost all the peaks after SPS and annealing were corresponded to that of tetragonal α-$MoSi_2$ [30].

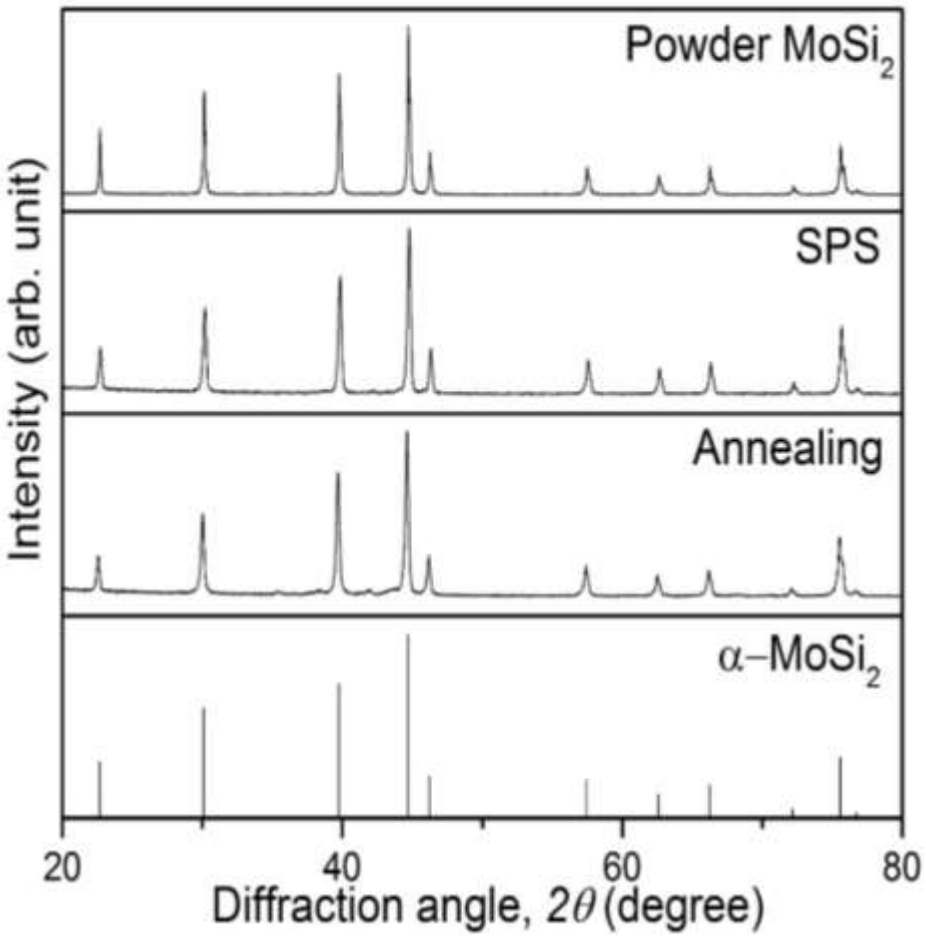

Figure 3.8 XRD patterns of α-$MoSi_2$ starting materials, after SPS, and after annealing, together with the literature data for tetragonal C11b-structured $MoSi_2$.

The lattice parameters at room temperature evaluated from XRD, were *a*-axis=0.3206±0.007 and *c*-axis 0.7854±0.0003 nm, respectively. The obtained lattice parameters for the both axes agreed with the reports and the values were 0.3204 and 0.7848 nm [30]. From the lattice parameter values, a theoretical density could be evaluated. The relative density defined from the measured theoretical density/theoretical density. A high relative density >96 % was obtained from the pellet specimen.

3.4.2.2 Thermophysical Properties

The linear thermal expansion coefficient (*LTEC*) of α-$MoSi_2$ from this study was evaluated with 2 methods such as (i) high temperature XRD (HT-XRD) and dilatometer. The lattice parameters of *a* and *c* axes increased linearly from 300 K to 1150 K, as shown in the Figure 3.9. The fitted linear expressions were:

$$a(\mathrm{T})=0.3201+1.949\times10^{-6}T \quad (3.2)$$

$$c(\mathrm{T})=0.7839+4.735\times^{-6}T \quad (3.3)$$

where T/K is the temperature.

The lattice volume, *V*, obtained from the lattice parameters expressed in the Eq. 3.2 and 3.3, the volume thermal expansion coefficient (β) could be determined by the relationship of:

$$\beta = \frac{1}{V}\left(\frac{dV}{dT}\right) \quad (3.4)$$

Thus, the linear thermal expansion coefficient (α_l) was evaluated by:

$$\beta=3\ \alpha_l \quad (3.5)$$

The value obtained from HT-XRD measurement was $5.66\pm0.20\times10^{-6}$ K^{-1}.

The linear thermal expansion coefficient is also measured from the dilatometer. The length change (dL/L_0) and linear thermal expansion coefficient (α_l) of α-$MoSi_2$ over a temperature range of 300-1500 K are shown in the Figure 3.10 (a, b). Length change and *LTEC* were increased with increasing temperature. The average LTEC obtained from the HT-RD was $8.10\pm0.36\times10^{-6}$ K^{-1} over a temperature range of 300-1500 K. In the Figure 3.10 (b) *LTEC* of α-$MoSi_2$ was plotted together with the *LTEC* (HT-XRD) and other references too. The LTEC obtained from HT-XRD was slightly lower than LTEC obtained from the dilatometer. The reason why this difference observed is still unclear. Deve et al. reported a value of LTEC was 8.73×10^{-6} K^{-1} over a temperature range of 473-1873K [31], Vasudevan et al. reported 8.93×10^{-6} K^{-1} over a temperature range of 473-1800 K [32], and Bose et al. 8.20×10^{-6} K^{-1} over temperature range of 273-1773 K [33]. A good agreement between *LTEC* (dilatometer) obtained from the present study and value reported by Bose et al.

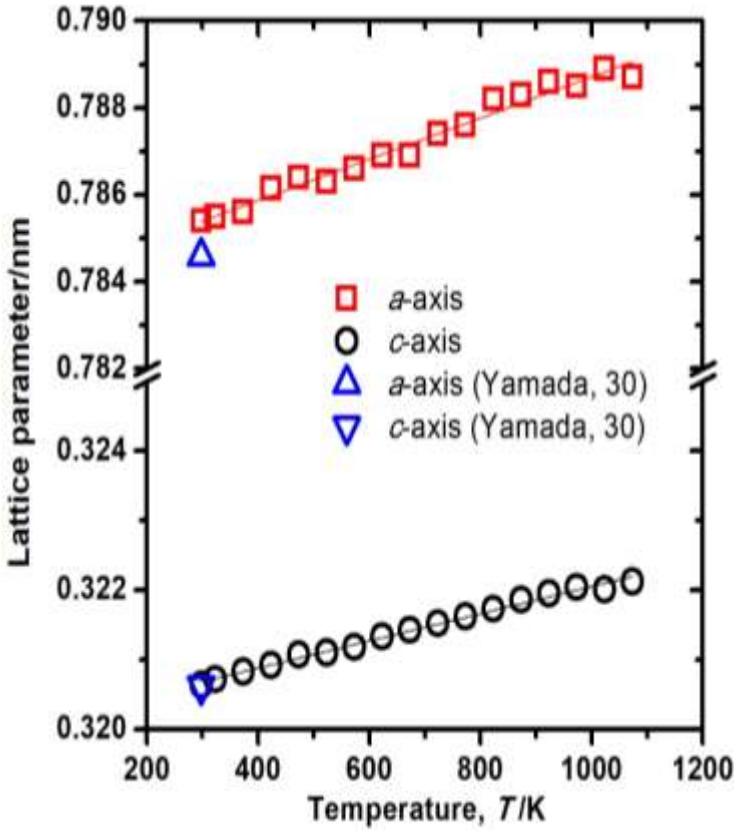

Figure 3.9 Lattice parameters for *a* and *c* axis of α-$MoSi_2$ dependence with temperature.

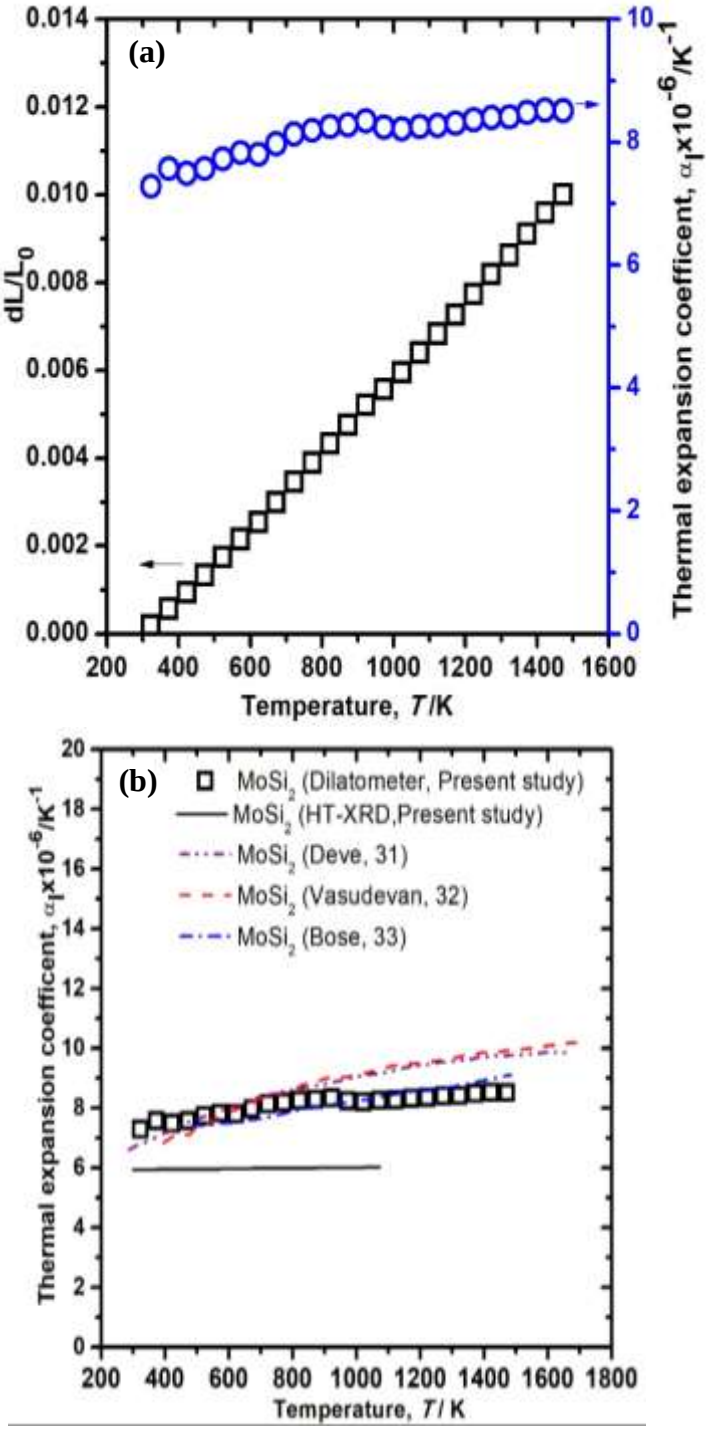

Figure 3.10 (a) Specimen length change and thermal expansion coefficient of α-$MoSi_2$ as a function of temperature. (b) Thermal expansion coefficient compared with values in the literatures.

Elastic constants such as Young's modulus (E), shear modulus (G), bulk modulus (B), Poisson's ratio (ν), and Debye temperature (θ_D) were estimated from the sound velocity measurement from the Equation 2.4~2.9. The average V_L and V_S were 8745 and 5273 ms^{-1}, respectively. The calculated values of V_L and V_S agreed with the values of V_L (8489 ms^{-1}) and V_S (5387 ms^{-1}) determined by the first-principle calculations performed by Sun et al. [34]. The calculated elastic constants values results were presented in the Table 3.2. The shear modulus and bulk modulus are 244 and 172 GPa which is agree with the reported values of 208 and 178 GPa [35]. The Young's modulus is 418 GPa, closed with the value of 417 GPa determined from the first theoretical calculation by Sun et al. [34], however, lower than values of 439 and 459 GPa reported by Nakamura et al. [36] and Dasgupta et al. [37]. The calculated Poisson's ratio is 0.214, larger than reported values of 0.15 [36-38]. The calculated values of θ_D is 742 K which is in a good agreement with the theoretical calculation of 738 K by Sun et al. [34]. The details of the results of Debye temperature is shown together with elastic constants in the Table 3.2.

The specific heat capacity as a function of temperature is shown in Figure 3.11 (a) together with other reported values. From the comparison, our measured data is closed with the other measured values [33, 39, 40] and calculated values [34]. To verify the measured specific heat capacity, the calculation specific heat capacity is performed and the results is shown in the Figure 3.11 (b). The total specific heat capacity is summation of the dilational, harmonic lattice vibration, and electronic terms. The specific heat capacity, C_p at constant pressure is calculated by [37]:

$$C_p = C_e + C_d + C_v \tag{3.6}$$

where C_v is the specific heat capacity at constant volume, C_e is the electronic specific heat capacity and C_d is the dilational specific heat capacity.

Table 3.2 Elastic moduli and Debye temperature of $MoSi_2$ as determined from longitudinal wave velocity and shear wave velocity.

Properties		**Tetragonal**
		α-$MoSi_2$
Longitudinal velocity ($m \cdot s^{-1}$)	V_L	8745
Shear velocity ($m \cdot s^{-1}$)	V_S	5273
Shear modulus (GPa)	G	172
Young's modulus (GPa)	E	418
Bulk modulus (GPa)	B	244
Poisson's ratio	v	0.214
Debye temperature (K)	θ_D	742

The dilational specific heat capacity, Cd expressions is [41] [41]:

$$C_d = (\frac{\beta^2 V}{k_T}) \cdot T \tag{3.7}$$

where β is the volumetric thermal expression define from equation 3.1, V is the molar volume, and k_T is the isothermal compressibility. The electronic term of specific heat capacity has been determined by:

$$C_e = \gamma T \tag{3.8}$$

where γ is the electronic term. Lasjaunias et al. suggested the electronic term for the α-$MoSi_2$ is 0.71 $mJmolK^{-2}$ [42]. Then, the harmonic lattice vibration can be written as:

$$C_v = 9\mathrm{n}k_\mathrm{B}\left(\frac{T}{\theta_\mathrm{D}}\right)\int_0^{\theta_\mathrm{D}/T}\frac{x^4 \mathrm{e}^\mathrm{x}}{(e^x-1)^2}dx \tag{3.9}$$

where n is the Avogadro's number and θ_D is the Debye temperature obtained from the present study determined from equation 2.9, and k_B is the Boltzmann constant. As shown *n* the Fig. 3.11 (b), the harmonic lattice vibration, C_v make significant contribution to the total specific heat capacity over the temperature range of 300-1300 K. Above Debye temperature, C_v is parallel to the Dulong –Petit law values (dashed purple line). However, for the whole temperature range, C_e and C_d did not make significant contribution to the specific heat capacity. The blue solid line is referred to the summation of the specific heat capacity as calculated from the equation 3.12. Thus, the specific heat capacity values measured from DSC almost equal to estimate values as calculated, suggest our measured data is reliable.

Electrical resistivity and ρ and Seebeck coefficient, S of α-$MoSi_2$ dependence with temperature is shown in the Figure 3.12 (a, b). The Seebeck Coefficient increase virtually over the temperature range. Further, the value of Seebeck coefficient of α-$MoSi_2$ is quite small and estimated to exhibit as metallic behavior. In addition, electrical resistivity slightly increased with increasing temperature. The electrical properties obtained from the present study, slightly difference with the values as reported by Yamada et al. [30] may due to the low density (67 % of T.D.) of specimen used for the measurement. However, the electrical resistivity value is same with value presented by Vries et al. [43]and Krontiras et al. [44] .

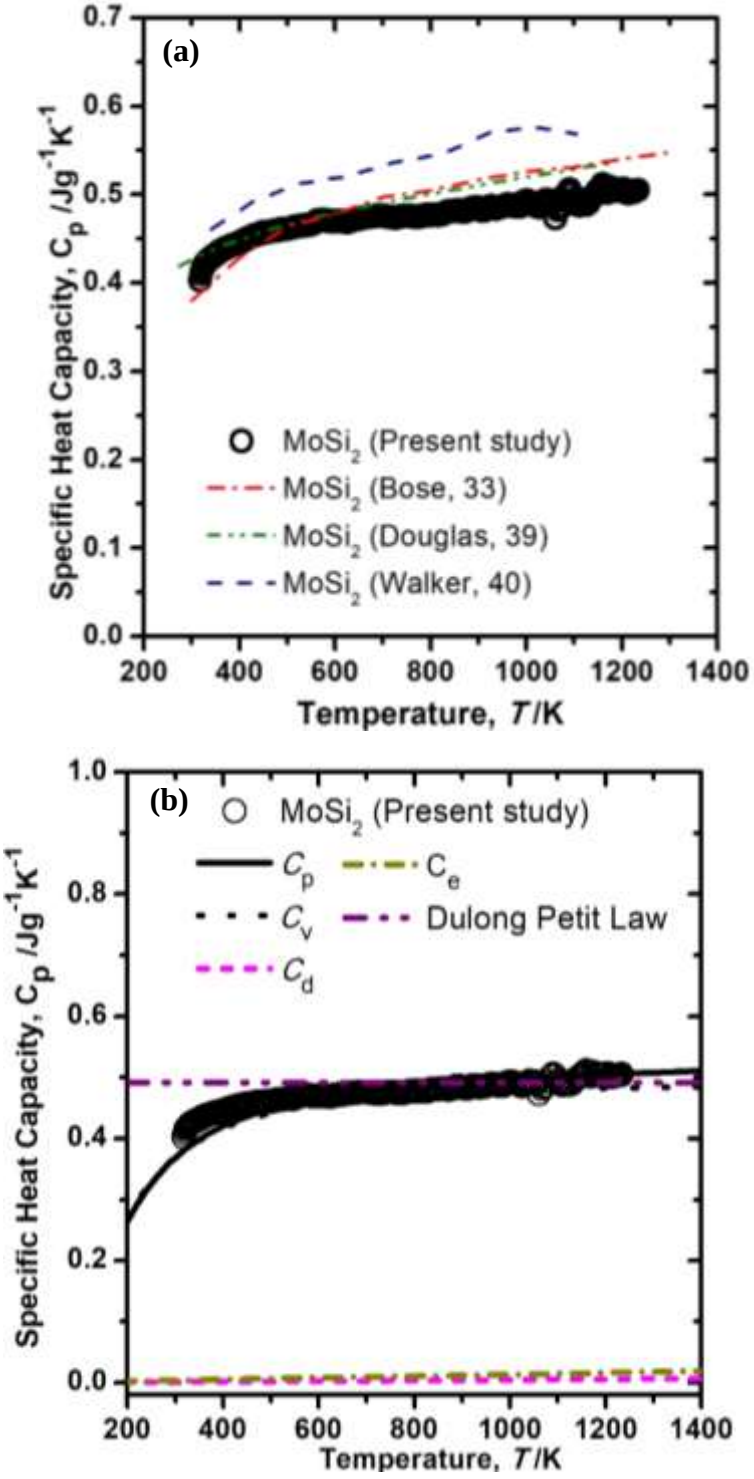

Figure 3.11 (a) Temperature dependence of specific heat capacity of α-$MoSi_2$. (b) Heat capacity of α-$MoSi_2$ as a function of temperature with calculated value. The highlighted line indicated the mechanism that contribute to the ultimate value.

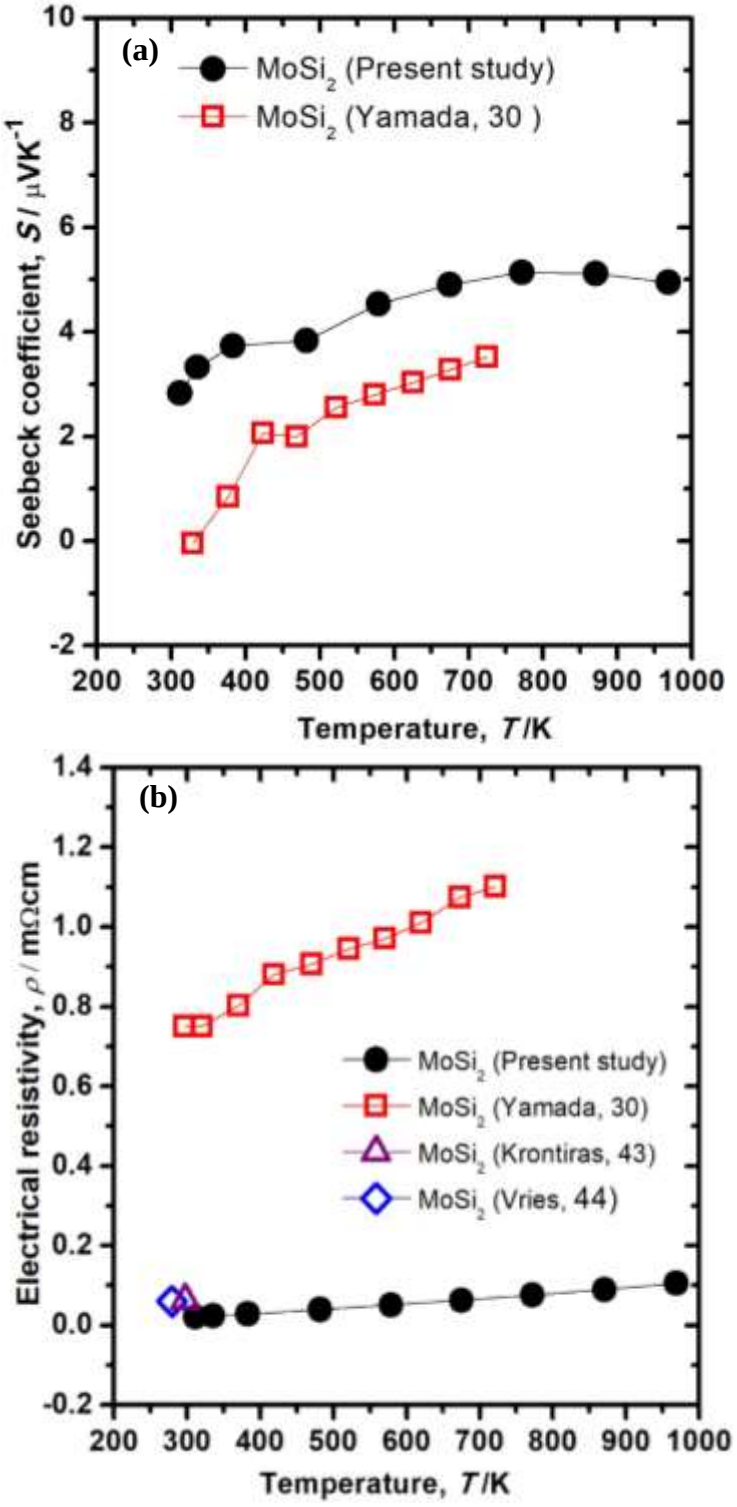

Figure 3.12 Temperature dependence of (a) Seebeck coefficient and (b) Electrical resistivity of α-$MoSi_2$.

Temperature dependence of the thermal conductivity together with available references is shown in the Figure 3.13 (a). From the Fig. 3.13 (a), thermal conductivities of α-$MoSi_2$ decreased with increasing temperature. The measured data show a good agreement with other reported values [32, 33], except reported values from Takami et al., which determined the thermal conductivity values from the calculation using COMSOL software [45]. Generally, for the metallic material, the thermal conductivity corresponds to the lattice and electronic contributions. The total thermal conductivities, λ_{tot} is given as:

$$\lambda_{tot} = \lambda_{ele} + \lambda_{lat} \tag{3.10}$$

where λ_{ele} and λ_{ele} describe as electrical and lattice thermal conductivities, respectively. λ_{ele} is defined using the Weidman-Franz Law [46]:

$$\lambda_{ele} = L \cdot \frac{1}{\rho} \cdot T \tag{3.11}$$

where L is the Lorenz number and ρ is the electrical resistivity measured from the present study. The calculated values of λ_{ele} and λ_{ele} together with λ_{tot} is shown in the Figure 3.13 (b). Electrical contribution seems to be influence in the α-$MoSi_2$ due to the electrical thermal conductivity is higher than lattice thermal conductivity in the whole temperature range. Thus, electrical contribution become dominant in the α-$MoSi_2$ if compared with the lattice contribution. Moreover, the electrical thermal conductivity and lattice thermal conductivity decreased with increasing temperature. This is due to the electron phonon scattering and Umpklapp phonon-phonon scattering.

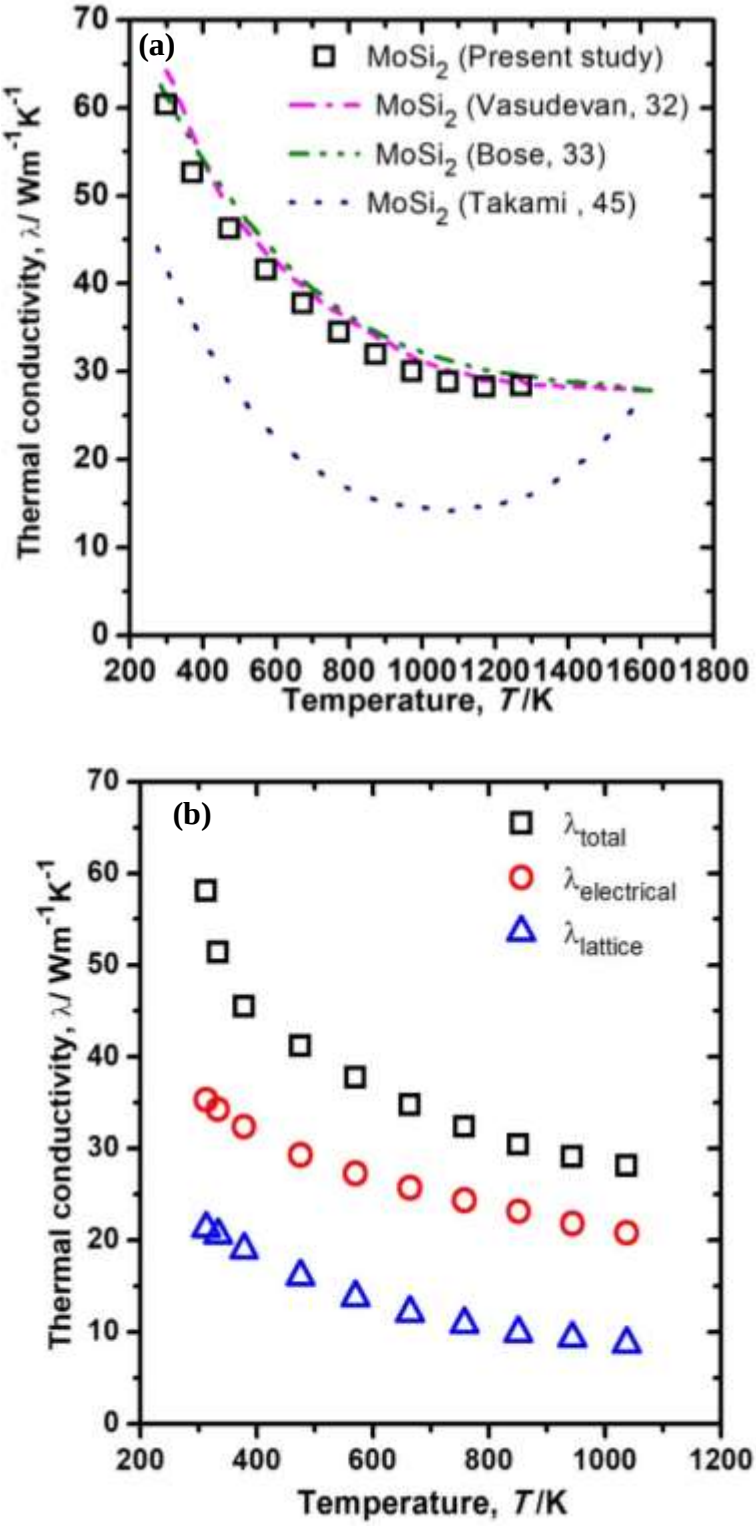

Figure 3.13 (a) Total thermal conductivity of α-$MoSi_2$ dependence of temperature. (b) Total, electrical and lattice thermal conductivity of α-$MoSi_2$ dependence of temperature.

The hardness and fracture toughness can be determined from the indent diagonal and four cracks produced from the center of the indent. The hardness and fracture toughness were expressed as:

$$H_{\mathrm{V}} = 1.854(\frac{F}{d^2}) \tag{3.12}$$

$$K_{\mathrm{IC}} = 0.016(\frac{E}{H})^{1/2}(\frac{F}{c_l^{3/2}}) \tag{3.13}$$

where F [N] is the load applied, d [m] is the diagonal indent, E [GPa] is the Young's modulus, c_l [m] is the four cracks generated from the indent center. The indent diagonal observed from the laser microscopy is shown in the Figure 3.14 (a). The Vickers hardness and fracture toughness dependence of the various load are shown in the Figure 3.14 (b, c). The hardness of $MoSi_2$ are decreased with increasing load. This phenomenon can be ascribed as indentation size effect when increasing load. The hardness values obtained from the present study are closed with other reported values from Shon et al. [47], Wade et al. [48], Harada e al. [49] .However, for the fracture toughness at 9.8 N, the values described from Wade's is lower than our data [48]. In addition, Lawrynowics et al. reported data is closed with value obtained from this study [50]. The reported data is the value evaluate without uncertainty.

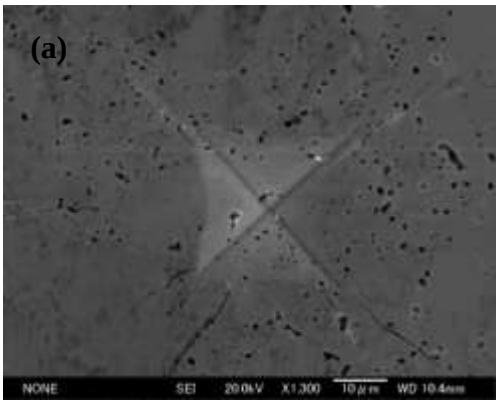

Figure 3.14 (a) Indentation fracture pattern observed from FE-SEM.

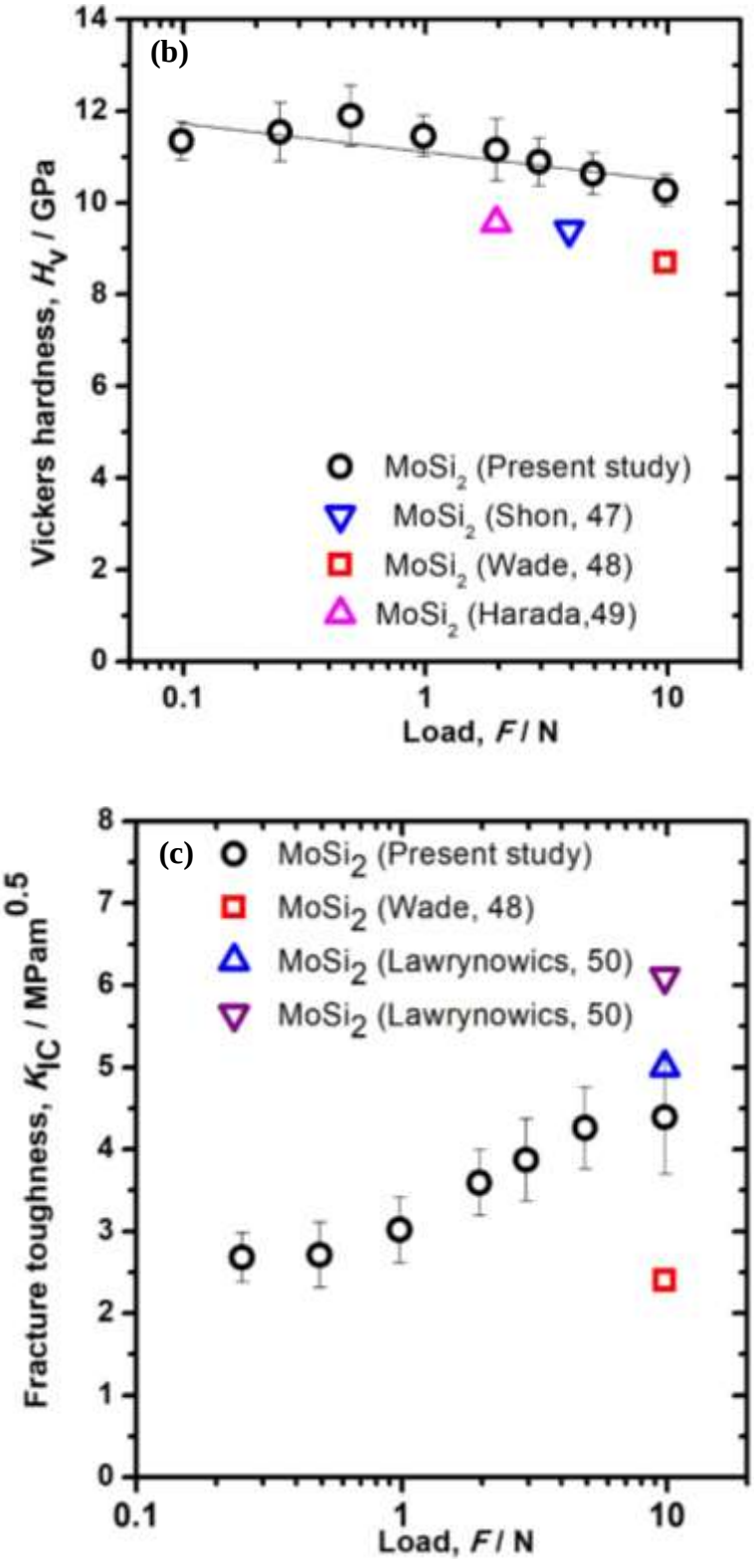

Figure 3.14 (b) Vickers hardness and (c) Fracture toughness as a function of various load.

3.4.2.3 Thermal stress of $MoSi_2$ with Mo

To evaluate either $MoSi_2$ is suitable to coating onto Mo cladding, thermal stress become one of the important parameter. In 3.4.2.2 session, the thermal stress will be evaluated from the obtained parameter in the session 3.4.2.1.

The elastic constants of $MoSi_2$, Mo, and Zr [51] are shown in the Figure 3.15. The Zr alloy references data are also plotted together. Generally, Young modulus is parameter to evaluate a material resistance against the tensions. As shown in the Fig. 3.15 (a), the Young's modulus of $MoSi_2$ is slightly higher than Mo, and also Zr. The bonding between atomic atoms are larger in the $MoSi_2$ if compare to the Mo. Higher elastic modulus means the materials become stiffer and likely to exhibit higher strength. If the stress level of the coating materials and cladding slightly mismatch, high elastic modulus of coating material might compensate the stress level.

Figure 3.16 show the thermal conductivity of $MoSi_2$ together with Mo with temperature dependence. Thermal conductivity of Mo is 40% higher than $MoSi_2$. As Mo is metallic material, generally thermal conductivity is high. Both materials showed a same trend of decreased of thermal conductivity with increasing temperature. This is due to the electron phonon scattering and Umpklapp phonon-phonon scattering. A high thermal conductivity is necessary for the coating and cladding material as this allow the heat release more efficiently.

Thermal expansion coefficient of $MoSi_2$ and Mo is shown in the Figure 3.17. The temperature range of the evaluated thermal expansion are from 300 to 1400 K to address the off-normal conditions of pressure water reactor. The thermal expansion coefficient of $MoSi_2$ is higher than Mo over the whole temperature range. However, the difference of thermal expansion of $MoSi_2$

and Mo is not really large, which is around ~0.86×10^{-6} K^{-1}. Thermal stress, σ of material can be written as:

$$\sigma = \varepsilon E \tag{3.14}$$

where ε is the strain and E is the Young modulus, respectively. The thermal stress of $MoSi_2$ with coating on Mo is shown in the Figure 3.17 with temperature dependence.

To evaluate either the obtain values for $MoSi_2$-Mo is enough as coating materials, the thermal stress of others coating-cladding materials are listed in the Table 3.3. The most famous candidates such as Zry-FeCrAl and Zry-Cr suggests that the thermal stress for these materials are 1090 MPa and 717 MPa, respectively. The obtained values for $MoSi_2$-Mo is lower from both candidates, which means the propose concept is promising.

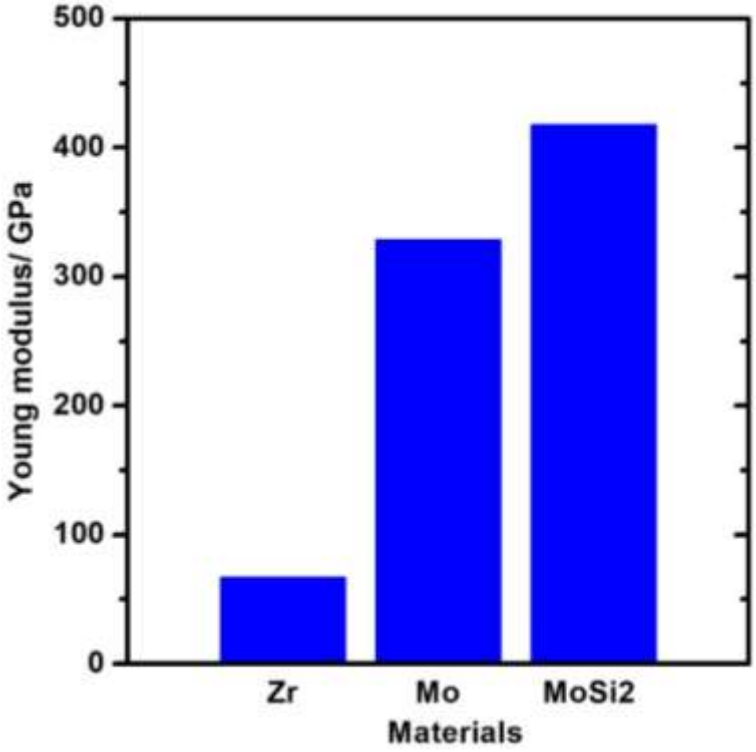

Figure 3.15 Young's modulus of Zr, Mo, and $MoSi_2$.

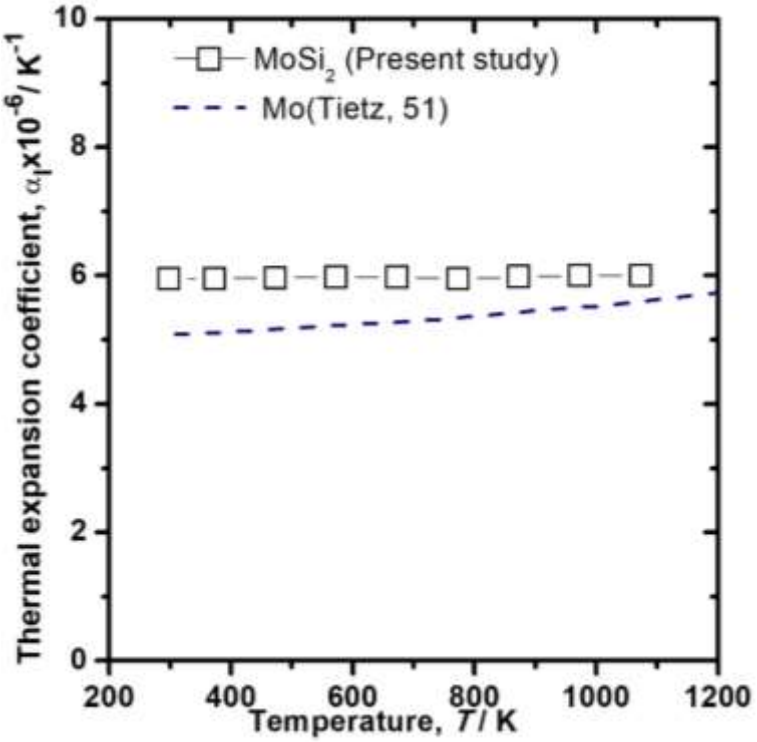

Figure 3.16 Linear thermal expansion coefficient of α-$MoSi_2$ and Mo as a function of temperature.

Table 3.3 Thermal stress value of cladding-coating candidates for ATF.

Material	Thermal stress @1000 K/MPa
Mo-$MoSi_2$	188
Zry-SiC	869
Zry-FeCrAl	1090
Mo-Zry	74
Zry-Cr	717

Chapter 4

Thermophysical properties of U-Si system compounds

4.1 Advanced nuclear fuel material candidates

From the Fukushima nuclear power station severe accident, low thermal conductivity of the uranium dioxide leads to the higher fuel line centreline temperature cause the thermal gradient of the fuel pellet was large. A higher thermal stress could produce cracking on the pellet, which means that the release of the fission product could be happen.

To avoid or prevent this phenomenon occurred again, an alternative nuclear fuels that compose a great thermal conductivity and high uranium density become favourable properties. A high uranium density of fuel could increase the fission density which allows a greater neutron penalty of the cladding material [4]. In addition, a high thermal conductivity of fuels will allow lower fuel centreline temperature, and the cracking of the pellet could be keep from happening or continuing. Recently, composite fuels such as uranium silicide, uranium mono-nitride and uranium carbide become the main primary candidates for the advanced nuclear fuel due to the possess high thermal conductivity and high uranium density [52, 53].

(i) Uranium-mononitride (UN)

Uranium mononitride (UN) exhibit hIgher thermal conductivity and fissile density than current fuel of UO_2. The thermal conductivity of UN is 13 W/mK at 300 K, and increased with increasing temperature [54]. The uranium density of UN is 14.3 g-U/cm3. In addition, a higher melting point of UN, 3123 K also become the advantages of UN [55].

The disadvantage of UN is easy to react with the steam with is unacceptable for the light water reactor [56, 57]. In addition, a high melting point of UN 3123 K [55] cause the sintering process difficult to carry out and obtained density higher than 95% of theoretical density [58].

(ii) Uranium silicide (U-Si)

Historically, Uranium silicide had been use widely for the research and test reactor considering feature a great uranium density and high thermal conductivity [59, 60]. Uranium Silicide consists of 6 compounds such as USi_3, U_3Si, U_3Si_2, USi, U_3Si_5, and USi_2 [61] as shown in the U-Si system phase diagram in the Figure 4.1. However, the most widely studied so far only U_3Si and U_3Si_2 for the research and test reactor due to the favourable properties.

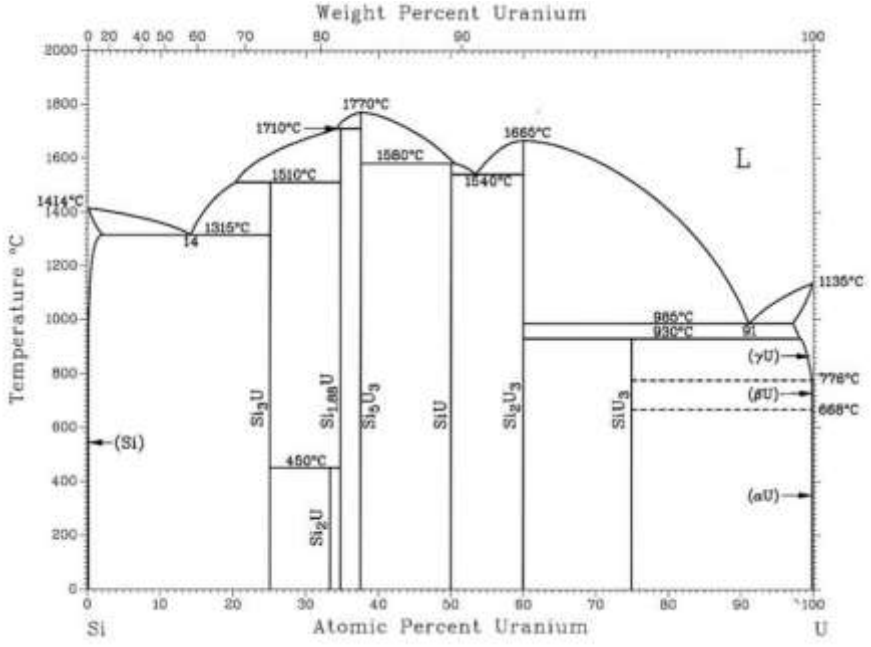

Figure 4.1 U-Si phase diagram.

For the accident tolerant fuel candidates, U_3Si_2 and U_3Si become the most attractive candidates in the U-Si system. The uranium densities of U_3Si_2 and U_3Si are 11.3 and 14.7 g-U/cm^3, respectively, which are higher than current fuel of UO_2 [62]. The thermal conductivities of both compounds exhibit 8.5 and 13.5 W/mK [62], while UO_2 is 9.8 W/mK at 300 K [63]. In addition, if compared with UN, the oxidation resistance of U_3Si_2 is better than UN.

4.2 Purpose of study

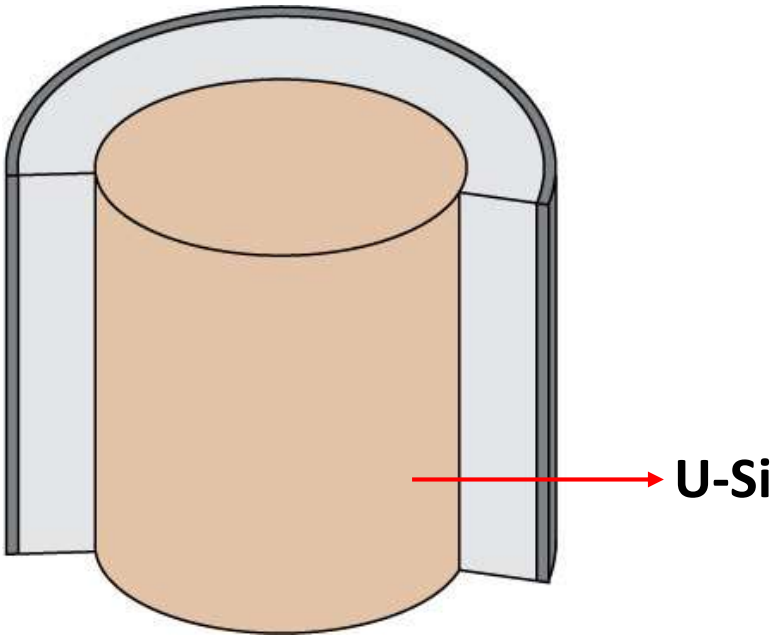

Figure 4.2 Schematic diagram of pellet as proposed in this study.

As explained in the section 4.1, Uranium silicide feature a great thermal conductivity and uranium density if compared with the contemporary fuel, UO_2. Recently, U.S DOE has been intensively study about this system for utilize it as future nuclear fuel for the light water reactor.

For the safety and design of the reactor, a basic property such as thermal and mechanical properties of candidate materials are necessary for the evaluation on the fuel performance.

Presently, there are a few reports that concern about the thermal properties of U_3Si_2 [62], U_3Si [64], U_3Si_5 [65] and USi [66] . However, there are many discrepancies exist in the reported data might be due to the existence of the impurity and low density of the prepared specimens. In addition, the mechanical property of the U-Si compounds still indefinable. Moreover, there is almost no report that concern about the rich Si compound, USi_3. Historically, U_3Si and U_3Si_2 had been used as dispersion fuel for the research and test reactor (RERTR). There are many scatter exist in the reported value, even though it had been utilizing in RERTR. This is due to the reliability of the properties of U-Si as dispersion fuel is not significant. In the other hand, the operating temperature around ~100 ˚C. Thus to utilize U-Si as a fuel in LWR as fuel pin, a reliable data on the basic properties are important for the safety. The fabrication and basic properties will be evaluated and compared with the available references.

Hence, in this study we would like to evaluate thermal and mechanical properties of U_3Si_2, U_3Si and USi_3. To acquire a reliable data, a high density of the specimen and less impurities will be synthesized. The characterization of the thermal properties such as linear thermal expansion, specific heat capacity at low and high temperature, and thermal conductivity with temperature dependence, while for the mechanical property, hardness, fracture toughness, and elastic constants will be evaluated. The obtained data from the present study will be compared with the available references data. Then, the behaviour of the compounds existed in the U-Si system will be study well from mechanical and thermal properties. To establish a source term on the U-Si system that might be utilize in light water reactor, preliminary study on the U-Si system is necessary. From

the obtained experimental data, we will suggest the most desire candidate that suitable to be consider as the alternative fuel in the U-Si system. The schematic diagram of the fuel pellet is shown in the Figure 4.2.

4.3 Experimental method and analysis

The U_3Si, USi_3 and U_3Si_2 samples were prepared from natural uranium (Nuclear Fuel Industries, Ltd.) and silicon (11N purity, KT's craft Co., Ltd.) by arc melting in an Ar atmosphere. In order to compensate the evaporation of Si arc melting, 0.2 wt.% of Si was excessively added for each specimen.

(i) U_3Si_2

The ingot obtained was annealed at 1073 K for 24 h under vacuum with sealed into a SiO_2 tube. To form a fine powder, ball milling was carried out at 200 rpm for 2h using tungsten carbide vials and balls. The sample was prepared in the glove box with Ar flow to prevent the oxidation. The sample was synthesized using spark plasma sintering (SPS) used carbon dye with 10 mm diameter size at 1123 K. A pressure of 75 MPa was applied and hold for 10 minutes at 1123 K (Dr. Sinter SPS-515A, Sumitomo Coal Mining Co., Ltd.). A constant of Ar flow 200 ml/min was retain during the sintering. The pellet size of U_3Si_2 was 10 × 3.5 mm.

(ii) U_3Si

The obtained ingot was sealed into SiO_2 tube in vacuum and annealed at 1073 K for 72h to achieve single phase of the U_3Si. The ingot produced was then cut to the cuboid shape with a size of 10×10×3 mm.

(iii) USi_3

The produce ingot of USi_3 was smashed into fine powder by ball milling at 200 rpm speed for 2h with a tungsten carbide vials and balls. To prevent the oxidation during the milling, the sample was prepared under Ar atmosphere. The sample then synthesize by spark plasms sintering (SPS) technique to 1273 K with holding time of 10 minutes (Dr. Sinter SPS-515A, Sumitomo Coal Mining Co., Ltd.). The pressure applied during synthesize was 100 MPa. The constant Ar flow was carried out during synthesize. The size of pellet was produced at 10 × 1.8 mm.

X-ray diffraction (XRD) analysis was carried out to characterize the bulk U_3Si and powders of USi_3 and U_3Si_2 specimen's crystal structures. The device equipped with a scintillation counter Cu-Kα radiation with a Rigaku Ultima IV X-ray diffractometer. The range of the measurement was perform over the 2θ range of 20° to 80° at room temperature. Least square method was used to determine the lattice parameters from the XRD peaks position. NIST Si was used for angle calibration. The relative density was calculated by times the theoretical (calculated from lattice parameters) and measured density (calculated from weight and dimensions of the sample).

A dilatometer was implement to determine the linear thermal expansion (Bruker AXS, TD5000SA) from 300 to 1050 K for U_3Si, 300 to 1500 K for USi_3, and 300 to 1200 K for U_3Si_2 under Ar flow. An Al_2O_3 reference sample was used for calibration. Low temperature specific heat capacity was performed by a relaxation method from 1.9 to 300 K using a Physical Property Measurement System (PPMS) (Quantum Design). The measurement was carried out on bulk sample of 30 mg (U_3Si) and 32 mg (USi_3). Differential scanning calorimeter, DSC (Jupiter, Netzsch) apparatus was used to determine the specific heat capacity from 300 to 1050 K for U_3Si, and 300 to 1200 K for U_3Si_2 under Ar flow atmosphere. This measurement was calibrated using a sapphire standard sample. Laser flash (LF) method using a LFA-457 (Netzsch) apparatus was carried out to determine the thermal diffusivity. The measurement was done more than one time

to obtain accurate measurement data, and the error was discovered to be less than 3 %. In addition, a comparison of measured thermal diffusivity was also carried out with the measured graphite standard sample (NMIJ RM 1201-a) [67]. The aberration between the measured values and literature were < 3%. From a relationship of density (p), specific heat capacity (C_p) measured by DSC, and thermal diffusivity (D), a measured thermal conductivity could be figure out.

Longitudinal and shear sound velocities values will allow to calculate the elastic constants. Ultrasonic pulse-echo method from the sing around ultrasonic instrument was used at room temperature (ULTRASONIC ENGINEERING CO., LTD. UVM-2). To determine the deviations of the measurement, a standard sample of iron was calibrated and correlate with the reported value [68] . The deviation between these values was < 0.4 %. The measurement for the sound velocity for the prepared specimens were measured 3 times and the uncertainties was written together with the calculated results as shown in the Table 4.1. The Vickers indentation test was carried out using a Vickers hardness tester (Akashi, hardness tester). The applied loads were 9.8 and 49 N for U_3Si and 9.8 N for USi_3 and U_3Si_2. The specimens were held with a loading time of 10 s, and a series of 10 indentations were placed on the surface for statistical averaging.

4.4 Results and discussions

4.4.1 Crystal Structures

XRD patterns for U_3Si_2, U_3Si, and USi_3 after arc-melting, SPS, and annealing are shown in the Figure 4. 3 (a-c). For U_3Si_2, after arc-melting, SPS, and annealing all peaks were corresponded to the tetragonal C11b-structure U_3Si_2 [69]. In the Figure 4.3 (b), after arc-melting the major peaks were indexed to the tetragonal C11b-structure U_3Si_2 [69] and minor peaks were corresponded to the tetragonal I4/*mcm*, β phase U_3Si [70]. However, after annealing all peaks were indexed to the U_3Si. Since the stable phase at the annealing temperature of 1073 K is cubic, the sample appeared to undergo phase transition from cubic to tetragonal during cooling process. For the USi_3, after arc-melting the major peaks were matched to the cubic c*P*4-structured USi_3 [71] and minor peaks were matched to the tetragonal I41/*amd* USi_2 [72]. These minor peaks became negligibly small after SPS, indicating that almost single phase of cubic USi_3 was obtained.

The lattice parameters for U_3Si_2, U_3Si, and USi_3 were defined from the diffraction peak positions and the values were listed in the Table 4.1. The calculated lattice parameters for each specimens (U_3Si_2, U_3Si, and USi_3) are accord with the references data [73]. As estimated from the obtained lattice parameters, the relative density of prepared U_3Si_2, U_3Si, and USi_3 specimens exceeded 96 % and 97% of the theoretical density.

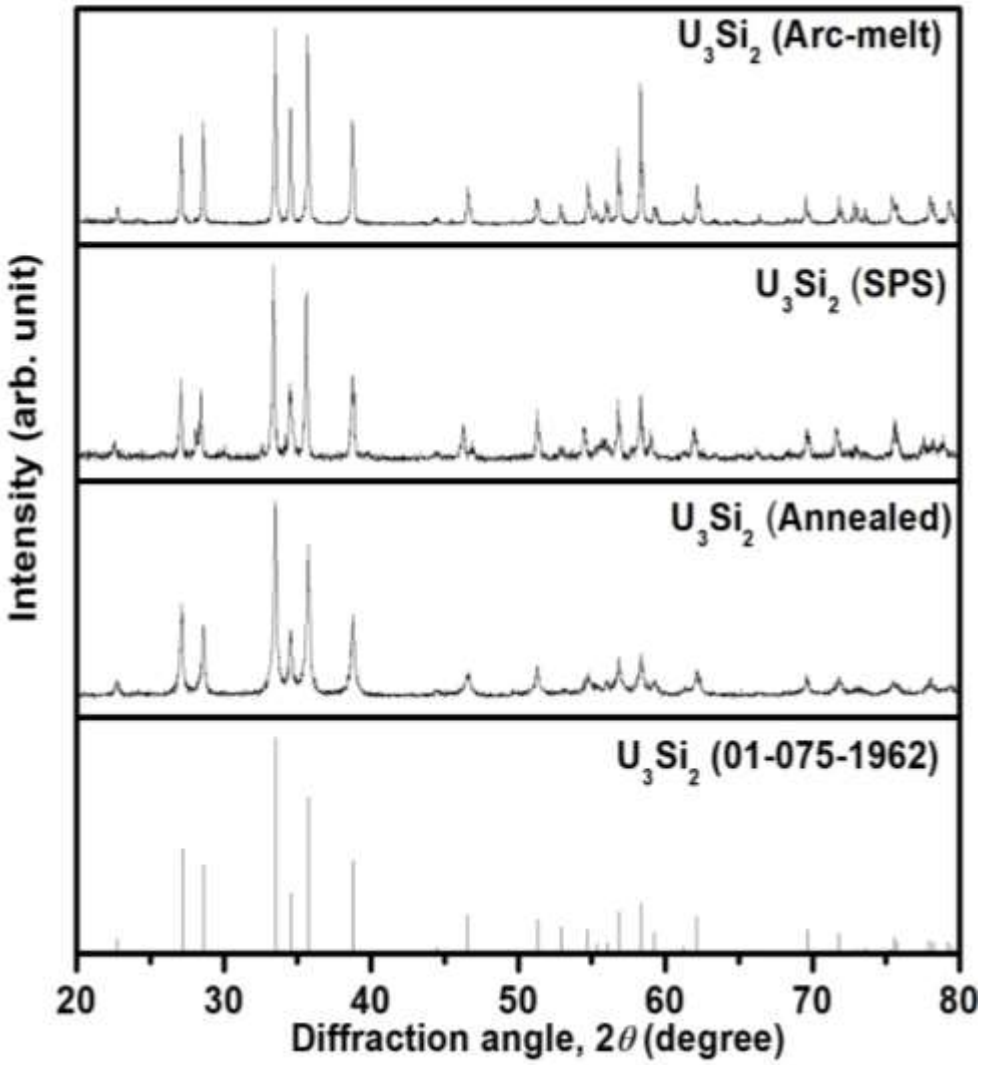

Figure 4.3 (a) XRD analysis of the powder U_3Si_2 after arc melting, SPS and annealing.

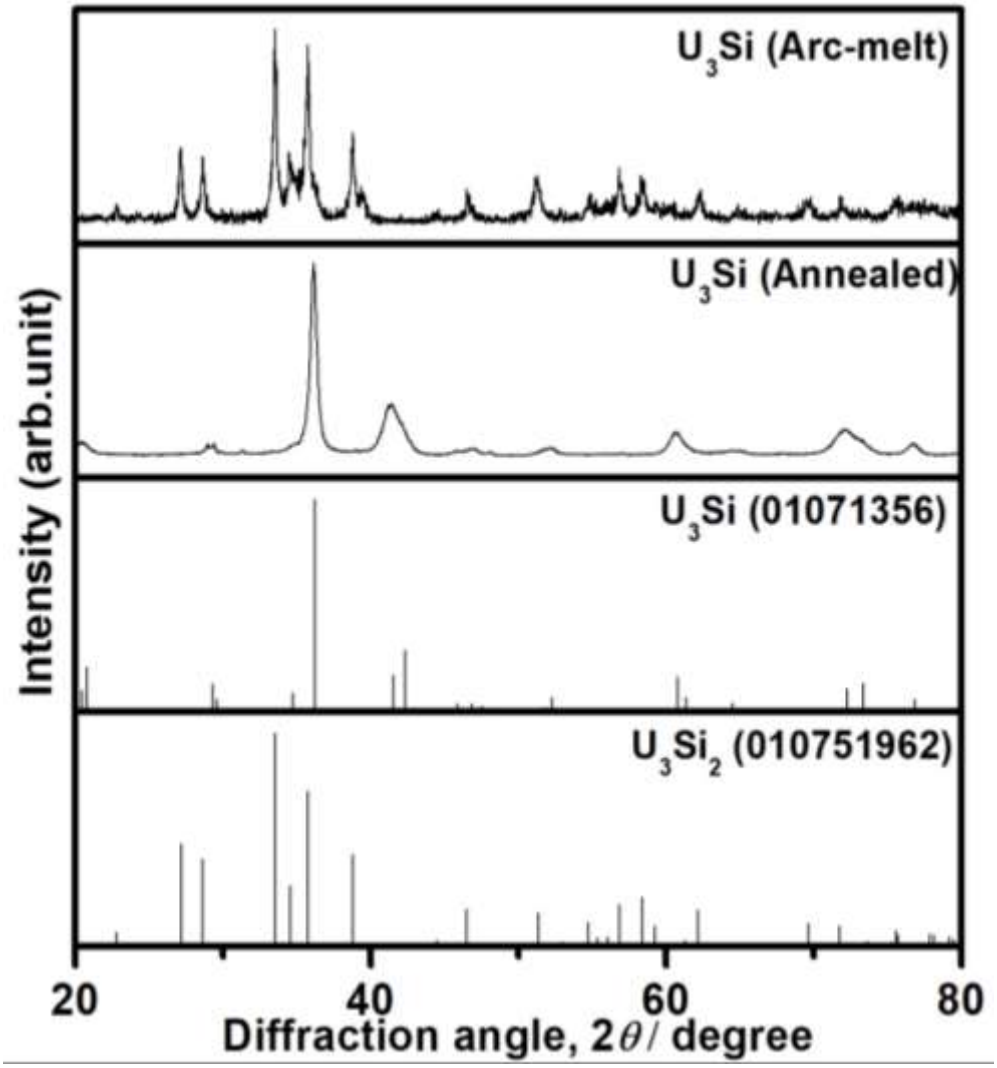

Figure 4.3 (b) XRD analysis of the ingot U_3Si after arc melting and annealing.

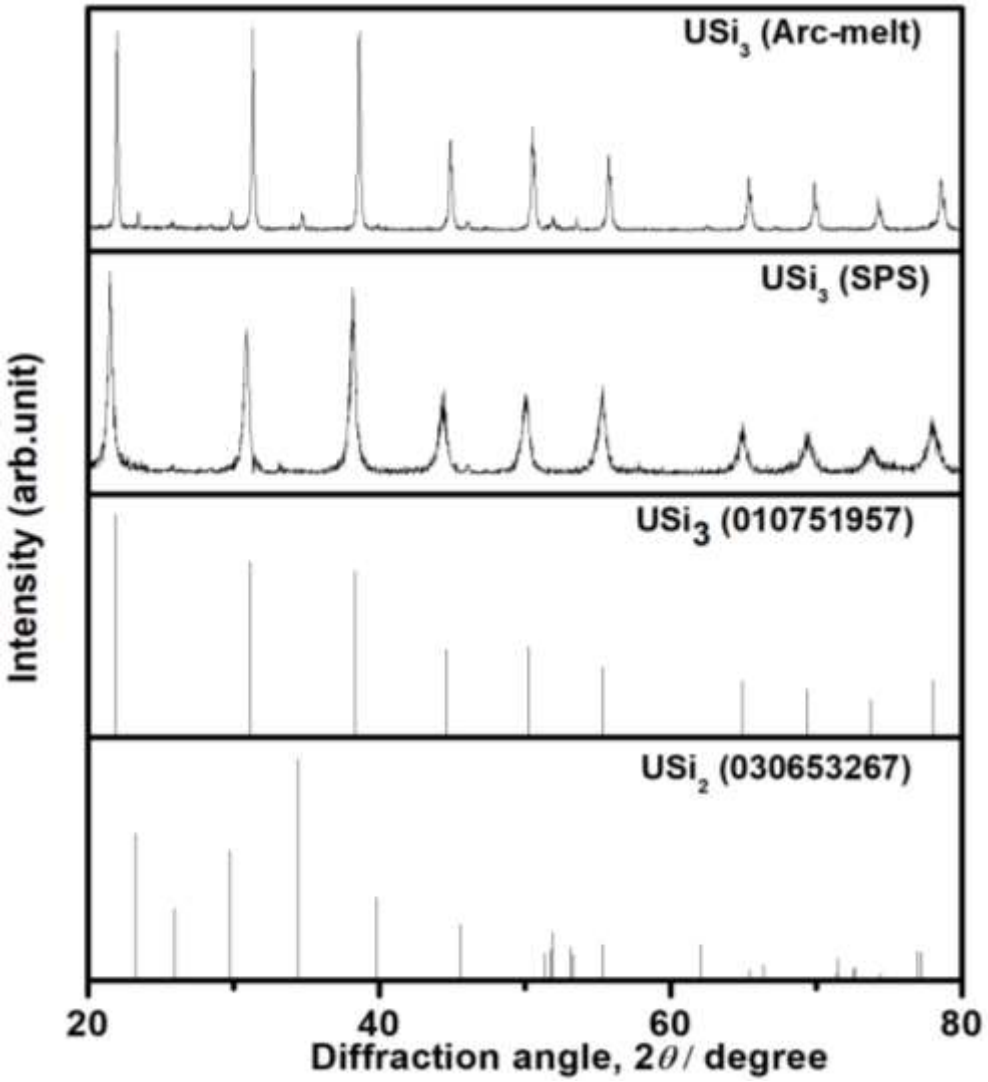

Figure 4.3 (c) XRD analysis of USi_3 powder after arc melting and SPS.

Table 4.1 Lattice parameters of U_3Si_2, U_3Si, and USi_3 obtained from the experiments together with the references value. The relative density also listed together.

Compounds	Experimental /nm		Reference/nm		Relative density/%
	a-axis	c-axis	a-axis	c-axis	
U_3Si_2	0.732±0.014	0.389±0.001	0.733	0.389	96
U_3Si	0.600 ± 0.004	0.877 ±0.011	0.603	0.870	96
USi_3	0.406±0.0002	0.406±0.002	0.404	0.404	97

4.4.2 Mechanical Properties

From the measurement of longitudinal wave velocity (V_L) and shear wave velocity (V_S), elastic constants of U_3Si_2, U_3Si, and USi_3 can be representing. The elastic constants for the Young's modulus (E), shear modulus (G), bulk modulus (B), Poisson's ratio (ν), Debye temperature (θ_D) are estimated from V_L and V_S and written in the Equation 2.4 ~ 2.9. As shown in the Table 4.2, the calculated elastic constants and Debye temperature of U_3Si_2, U_3Si, and USi_3 were listed together. The obtained Debye temperature and elastic constants are closed with theoretical values calculated based on the density functional theory [74, 75]. The resistance of materials against the tensions could be evaluate from the Young's modulus. From the Table 4.2, the Young's modulus values increased with increasing Si content from the U_3Si, U_3Si_2, and USi_3. This result suggested that bonding strength between U-Si atoms increased with increasing Si amount in U-Si system.

The brittleness or ductile behavior of the material could be estimated from the B to G ratio (k) or Poisson's ratio. Following to the "*Pugh's criterion*", if the k value >1.75 the material categorizes as ductile, while k value <1.75the material categorize as brittle [76]. The B/G ratio of U_3Si, U_3Si_2, and USi_3 are 1.80, 1.33, and 1.37. Another parameter signifies brittleness or ductile behavior of material is Poisson's ratio. ν of U_3Si_2 and USi_3 are smaller than <0.25, while U_3Si >0.25. From the both estimation, U_3Si_2 and USi_3 exhibit as brittle, despite, U_3Si exhibit as ductile material. Typically, the material become ductile if the atomic bonds mainly metal, in contradiction with the brittle material where the covalent atomic bond existed. In the U-Si system, the Pugh' criterion showed the material become brittle when the Si amount increased, as the rich U metal only show the ductile material among others.

The hardness of U_3Si_2, U_3Si, and USi_3 are evaluated from the Vickers hardness measurement. The Vickers hardness, H_V is expressed as shown in the Eq. 3.18. The indentation diagonal length was investigated from the FE-SEM for U_3Si_2 as shown in the Figure 4.4 (a) and laser microscopy for U_3Si and USi_3 as presented in the Figure 4.4 (b, c). The Vickers hardness of U_3Si_2, U_3Si and USi_3 at 9.8 N were found to be 7.51±0.41 GPa, 2.17±0.1 GPa and 4.64±0.20 GPa as shown in the Figure 4.5 (a). As estimated from the elastic constant that U_3Si exhibit ductility behavior, the hardness of U_3Si was also carried out at 4.9 N load and found to be 2.28±0.01 GPa. For U_3Si_2, the hardness value obtained from the present study is agree well with the recently reported value [77]. Domagala et al. reported the hardness of U_3Si at 0.49 N was 4.49 GPa which is higher than hardness value at 9.8 N and 49 N [78]. In the Figure 4.5 (a), the hardness of USi is also plot together. At 9.8 N, the H_V value of U_3Si_2 are higher than other U-Si compounds such as U_3Si, USi_3, USi [79], and U_3Si has the lowest hardness. This result suggested the low hardness may due to the U_3Si exhibit as most metal-rich compound in the U-Si system. A higher hardness value of U_3Si_2 at 9.8 N considering the higher melting point of U_3Si_2 among U_3Si, USi_3, USi, which mean the atomic bonding strength of U-Si in the U_3Si_2 is high. In addition, the hardness of UO_2 and UN were also plotted together in the Figure 4.5 (a). The hardness of U_3Si_2 is highest follow by USi_3, UO_2 [80], UN [81], and U_3Si.

The relationship of Vickers hardness of U-Si specimens prepared by the present study are is plotted in the Figure 4.5 (b). The hardness of ductile material (U_3Si) is lower compared to the brittle material (U_3Si_2, USi_3). According to the Young's modulus results, the bonding of USi_3 is larger than U_3Si_2 and U_3Si. Typically, a higher bonding strength among atoms produced higher hardness values. However, the hardness value of U_3Si_2 and USi_3 is against the general theory of

the bonding strength. As the microstructure/defect also affect the hardness value of material, a further analysis on the defect is necessary for each compounds.

The fracture toughness has relationship with the cracks generated from the indentation and the equation is written in the Eq. 3.19. For E and H_V, the values evaluated from the present study were used. However, for the U_3Si, due to the there is no cracks were generated at 9.8 and 49 N, the fracture toughness for this material could not be evaluated. The fracture toughness for U_3Si_2 and USi_3 are found to be 3.25±0.20 $MPam^{0.5}$, respectively at 9.8 N as shown in the Figure 4.5 (c). The fracture toughness of U_3Si_2 obtained from the present study was higher than Metzger et al. reported value [77]. This might be due to the impurities of U_3Si_5 and USi existed in the specimen and affect the measurement values. Considering the precipitates at grain boundary might decline the fracture toughness, the existence of impurities from the Metzger's specimen could affect the reported values [82, 83]. The fracture toughness of UN [81] is highest follow by the USi_3, U_3Si_2 and UO_2 [80].

Table 4.2 Elastic constants and Debye temperature of U_3Si_2, U_3Si, and USi_3 obtained from the experimental together with the data obtained from first-principle calculation.

Crystal system		**Tetragonal**		**Tetragonal**		**Cubic**	
		U_3Si_2 [Experimental]	**U_3Si_2 [Calculation]**	**U_3Si [Experimental]**	**U_3Si [Calculation]**	**USi_3 [Experimental]**	**USi_3 [Calculation]**
Longitudinal velocity (ms^{-1})	V_L	3772±26	3865	3921±10	3791	5640±137	5522
Shear sound velocity (ms^{-1})	V_S	2310±2	2355	2263±11	2100	3523±95	3361
Shear modulus (GPa)	G	62.9±0.1	67	77±3	69	98±4	92
Young's modulus (GPa)	E	151.0±0.9	163	192±5	178	231±3	222
Bulk modulus (GPa)	B	83.9±2.3	92	128±2	134	121±15	125
Poisson's ratio	v	0.20±0.1	0.2	0.25±0.02	0.28	0.18±0.03	0.21
Debye temperature (K)	θ_D	275.5±0.3	280	251	259	455±3	435

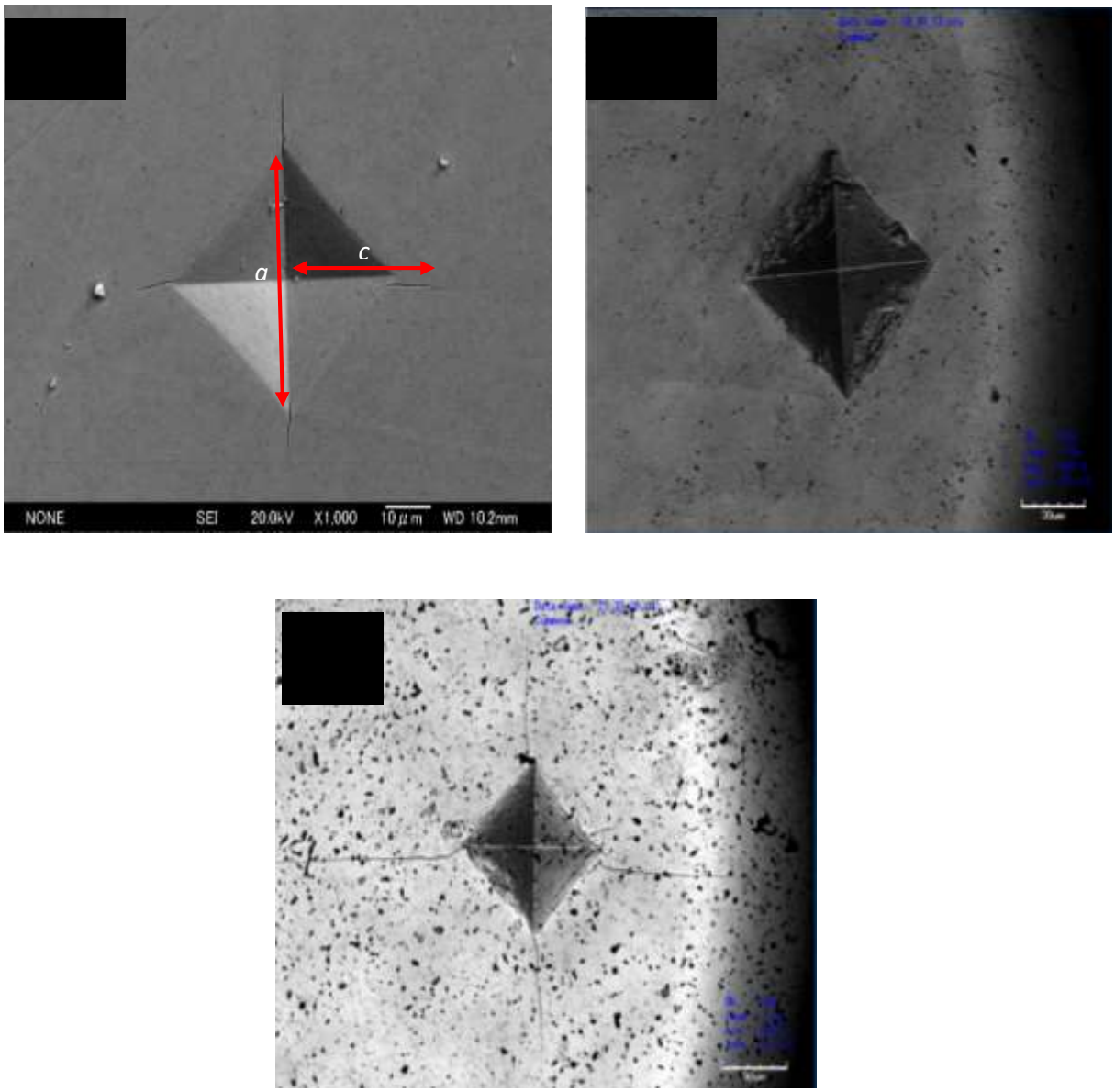

Figure 4.4 The Vickers indentation fracture pattern of (a) U_3Si_2 at 9.8 N imaged by FE-SEM (b, c) U_3Si and USi_3 at 9.8 N imaged by laser microscopy.

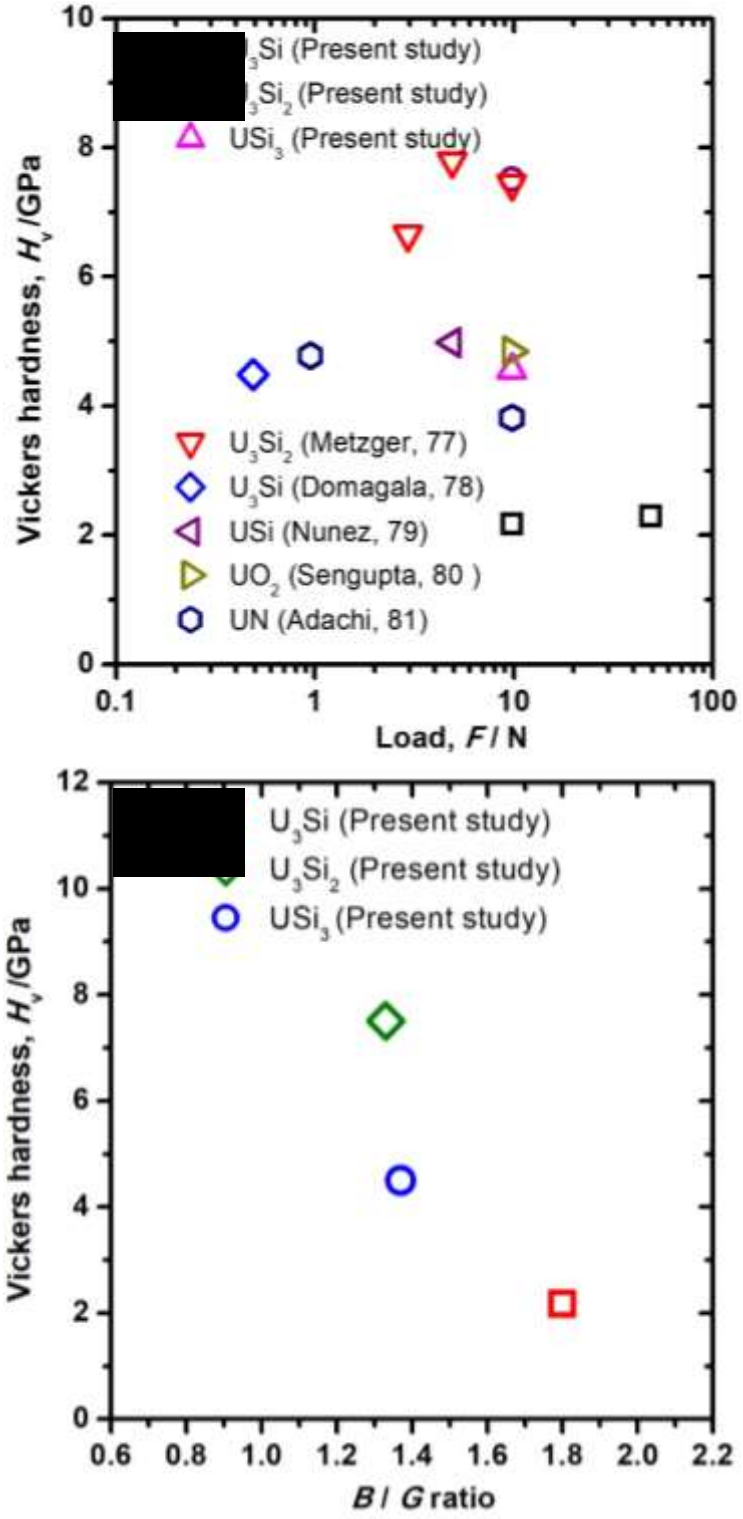

Figure 4.5 (a) Vickers hardness as a function of load (b) Relationship of Vickers hardness with the *B*/*G* ratio.

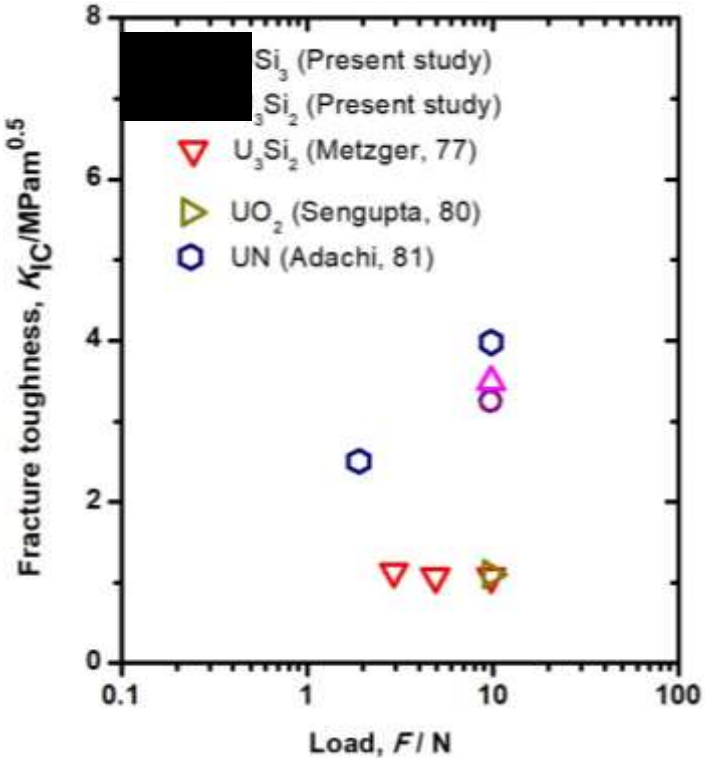

Figure 4.5 (c) Fracture toughness as a function of load.

4.4.3 Thermal Properties

Thermal expansion of U_3Si_2, U_3Si, and USi_3 are evaluated from the length change of specimens with temperature dependence as shown in the Figure 4.6 (a-c). The length changes for each specimen were measured by dilatometer. The length changes of the specimens are written as $(L\text{-}L_o)/L_o$. The linear thermal expansion coefficient (*LTEC*) can be defined from the Equation 2.13. The *LTEC* of U_3Si_2 almost constant from 300 to 800 K. However, above 800 K, the *LTEC* precipitously increased. Below 800 K, the measured *LTEC* from this study is closed with others reported values [62, 84, 85]. Figure 4.6 (b) shows that the *LTEC* of U_3Si measured in the this study was lower than White et al., [64]. The discrepancies existed between present study and White's data might be due to the existence of impurity (U_3Si_2 and UO_2) in the White's specimen or different determine method. We define *LTEC* from the change of sample length at each temperature while

White's define from the gradient of the graph. For USi_3 as shown in the Fig. 4.6 (c), the measured value was lower than the Loch et al. [84] described values over the whole temperature range. The discrepancies exist between this study and Loch et al is unclear due to the no explanation regarding measurement method was explained in Loch's report. The relationship between thermal expansion coefficient and Si/U composition is plotted in the Figure 4.6 (d). The average thermal expansion coefficient of U-metal [86], U_3Si, U_3Si_2, USi [66], U_3Si_5 [65], USi_3, and Si [87] were defined at 1000 K. The average of thermal expansion coefficient of U-Si compounds has decreased tendency with increasing the Si amount in the U-Si system. Generally, the metal produced higher thermal expansion coefficient than ceramics. In addition, with increasing the Si amount in the U-Si system, the covalent bond between U-Si atoms become stronger than atomic atoms of metal. The decreased tendency of the U-Si compounds as shown in the Fig 4.6 (d) is due to the large covalent bond strength between atoms when the Si amount is increased in the U-Si system.

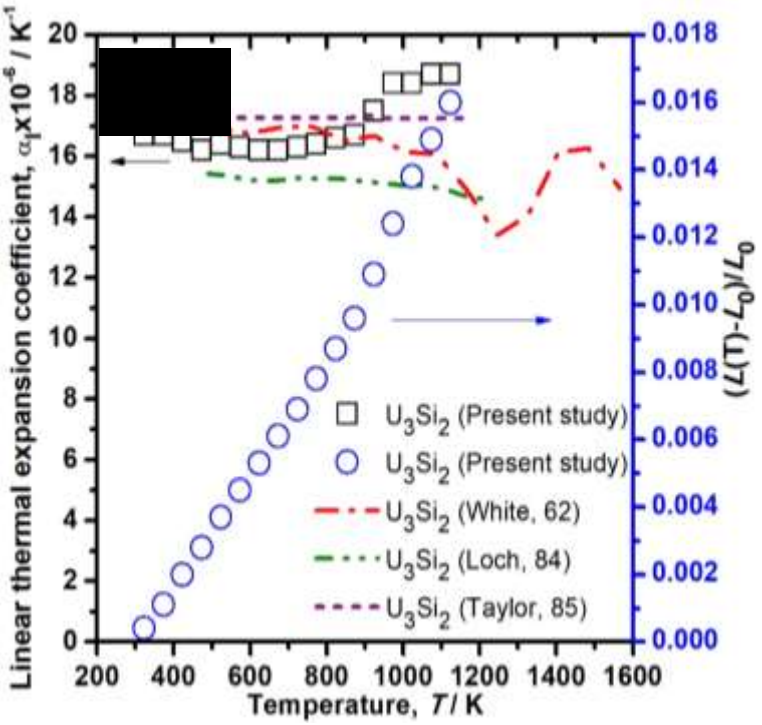

Figure 4.6 Length change and linear thermal expansion of (a) U_3Si_2 as a function of temperature.

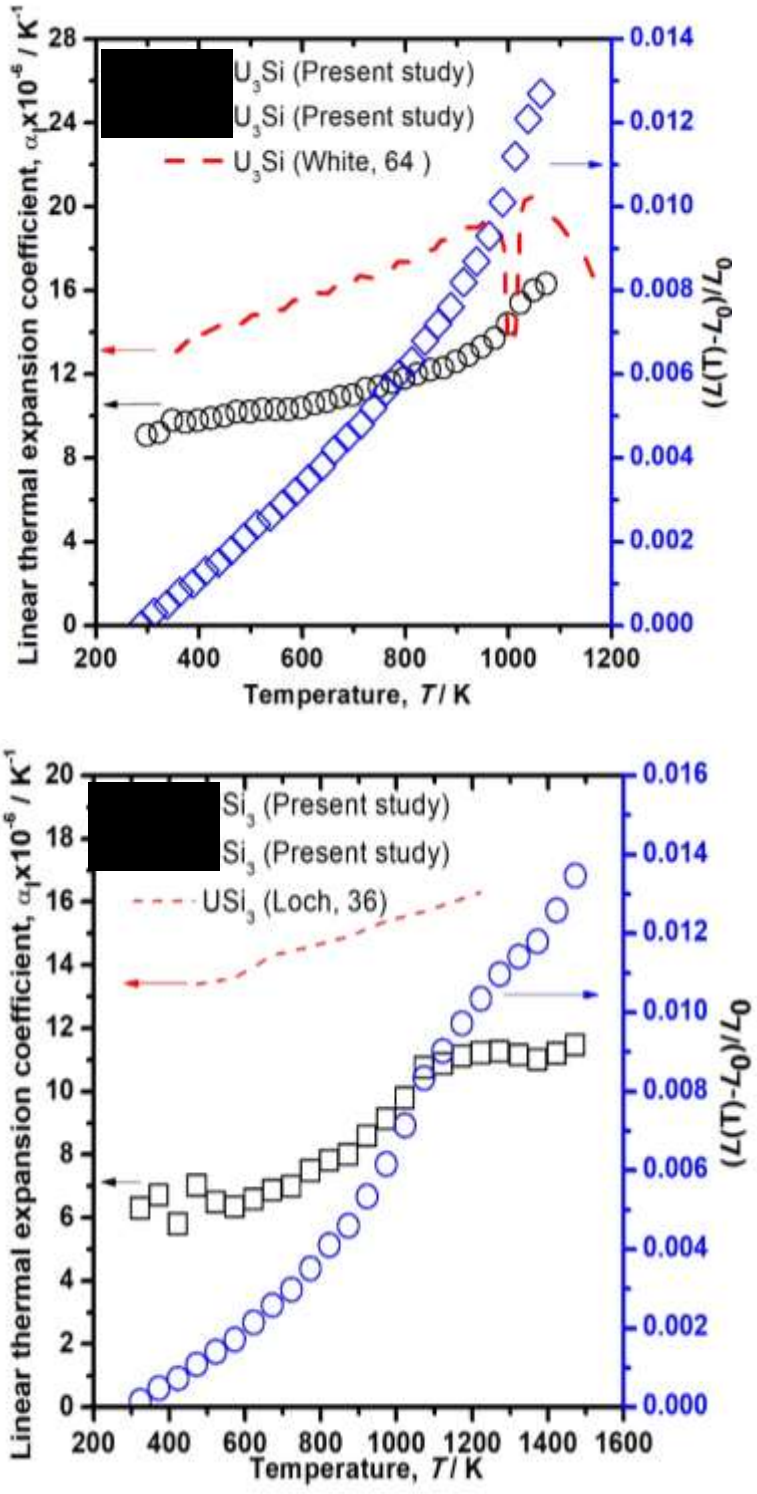

Figure 4.6 Length change and linear thermal expansion of (b) U_3Si, and (c) USi_3 as a function of temperature.

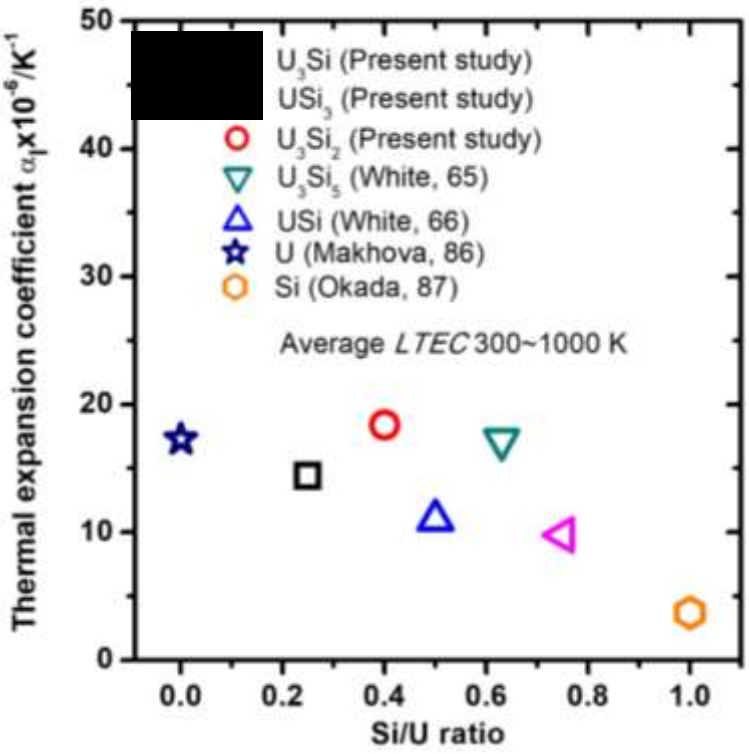

Figure 4.6 (d) Relationship average thermal expansion coefficient with Si/U composition of U-Si system together with Si single crystal and U-metal.

Low and high temperature of specific heat capacity (C_p) were determined by PPMS and DSC, respectively. PPMS measurement for the low specific heat capacity, while DSC for the high temperature specific heat capacity. The measured values of specific heat capacity of U_3Si_2, U_3Si, and USi_3 are presented in the Figure 4.7 (a, b, c). In the Figure 4.7 (a), the C_p values of U_3Si_2 obtained from the present study was lower than other reported values [62, 88, 89] from 300 to 1200 K. Figure 4.7 (b) shows specific heat capacity measured by PPMS evenly connected with those values measured by DSC at 300 K. There is no phase transition was observed at 123 K, as described by Kimmel et al [90]. Since the change in the heat capacity due to this phase transition is small [90], that might be not detected in this study. The specific heat capacity measured by DSC

increased with increasing temperature. However, at 1050 K, it abruptly rises and decreased again. This phenome address as transition phase, which means U_3Si tetragonal phase transform to the cubic phase at this temperature. White et al. reported values is closed with the present study, and the phase transformation also observed from the report [64]. However, there are difference values of C_p above 300 K observed from present study with Snelgrove et al. [91], Shimizu et al. [92], and Flotow et al. [93]. In the Figure 4.7 (c), the USi_3 C_p measured from PPMS connect smoothly with the C_p values taken from database [94] . The discrepancies existed between present study and other reports for the U_3Si_2, U_3Si are unclear. This is due to the impurity and density would not affect the measurement values. A further evaluation of the measured specific heat capacity is carried out as below.

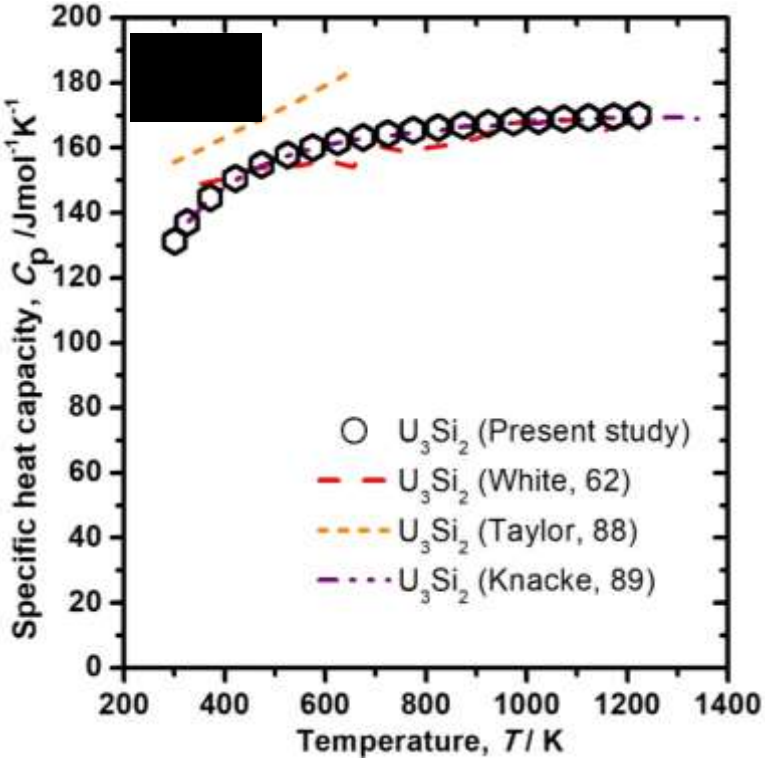

Figure 4.7 Specific heat capacity of (a) U_3Si_2 measured from DSC. The available reference data also plotted together.

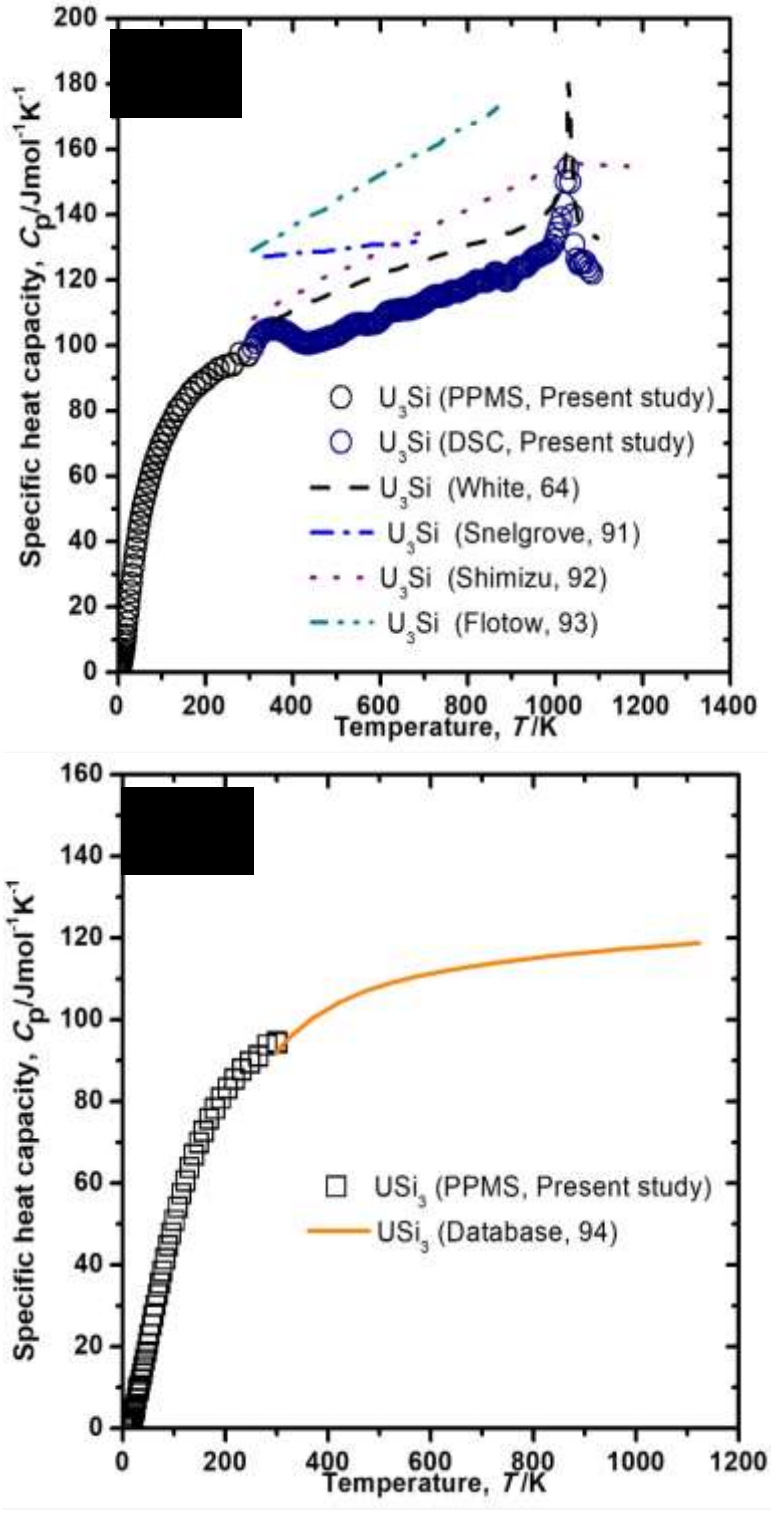

Figure 4.7 Specific heat capacity of (b) U_3Si, and (c) USi_3 measured from PPMS and DSC. The available reference data also plotted together.

The low temperature specific heat capacity consists of electronic term and lattice heat capacity expressed as below:

$$C_p = \gamma T + \beta T^3 \tag{3.1}$$

or the linear fitting representing:

$$\frac{C_p}{T} = \gamma + \beta T^2 \tag{3.2}$$

as shown in the Figure 4.7 (e). The parameters of γ and β are the coefficient of electronic and lattice heat of the specific heat capacity. The coefficient of lattice heat capacity, β is related to the Debye temperature as expressed:

$$\theta_D^3 = n\left(\frac{12\pi^4 N_A \kappa_B}{5\beta}\right) \tag{3.3}$$

According to the equation 3.3, the calculated value of Debye temperature of U_3Si and USi_3 from fitting of PPMS are lists in the Table 4.2. When T=0 K, the linear segments yields the electronic terms. The values of Debye temperature and electronic term are lists together in Table 4.2.

Table 4.2 Calculated values of Debye temperature and electronic term of U_3Si and USi_3.

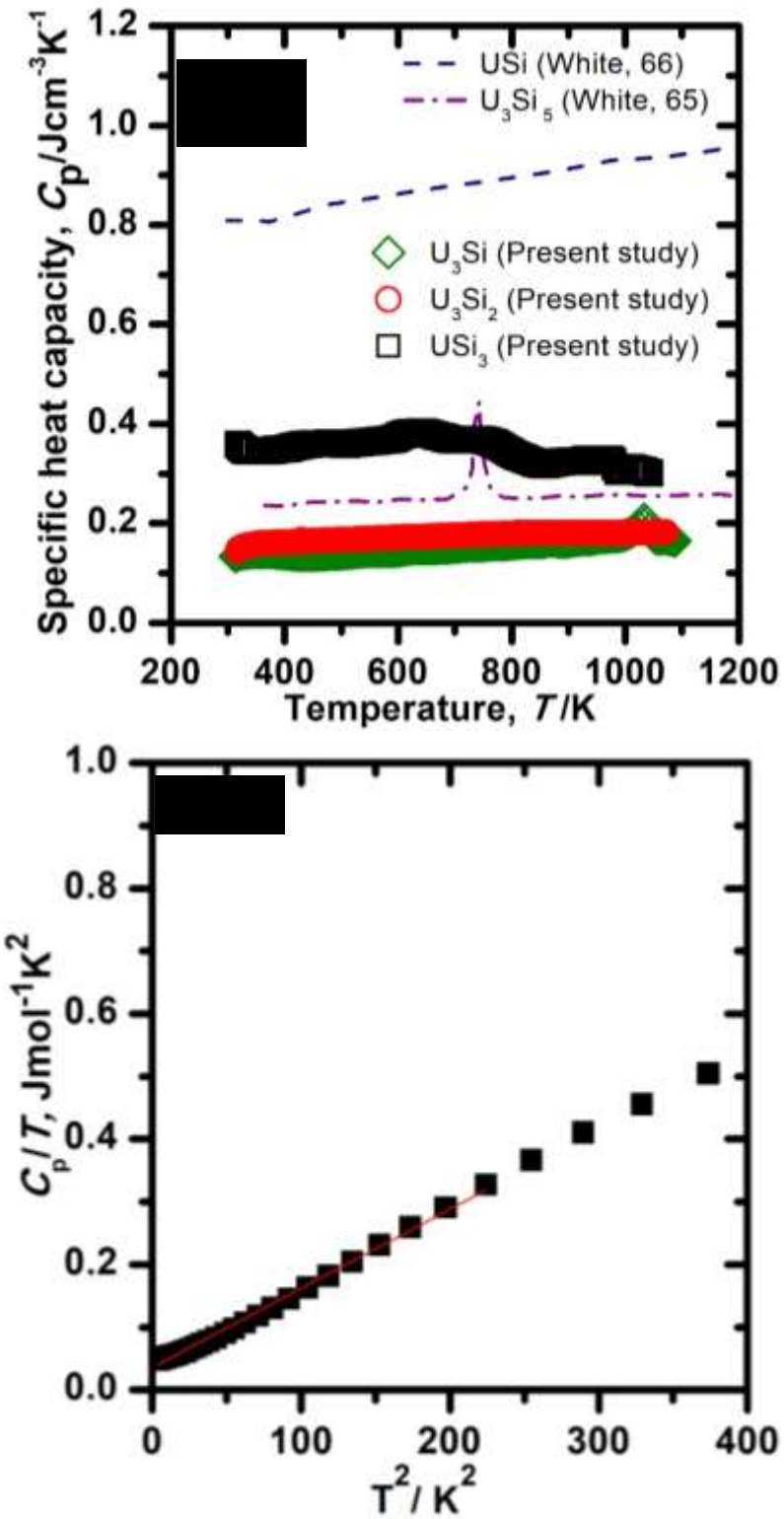

Figure 4.7 (d) Specific heat capacity of U-Si compounds with temperature dependence. (e) Linear fitting of low temperature of specific heat capacity to determine Debye temperature and electronic term.

The Debye temperature determine from the fitting of low temperature specific heat capacity is closed with the values calculated from the sound velocity.

The correlation between measurement and calculation values were carried out to evaluate the validity of the measured data. The theoretical calculation of U_3Si_2, U_3Si, and USi_3 were calculated and are shown in the Figure 4.8 (a, b, c). Generally, constant pressure of specific heat capacity, C_p can be representing by the summation of electronic (C_e), dilation (C_d) and lattice (C_v) as expressed in the Eq. 3.12~3.14. The electronic term, γ used for estimated electronic specific heat coefficient term is 36.5 mJ/molK^2 (U_3Si) and 14.0 mJ/mol·K^2 (USi_3) as obtained from the extrapolation fitting of low temperature of heat capacity (T=0) from the present study. The harmonic lattice vibration term is defined using the Debye temperature and the equation is written in the Eq. 3.15, where θ_D is the Debye temperature for both compounds as calculated from the present study. The addition of C_v, C_e, and C_d components generate the total specific heat capacity, C_p as shown as black solid line in the Figure 4.8 (a, b, c). The calculated specific heat capacity for U_3Si_2 as shown with black solid line was closed with the measured values. Moreover, for U_3Si the calculated values of C_p was constant with the measured C_p from PPMS and DSC values till 800 K. The phase transformation of C_p for U_3Si did not account during calculation, that's mean the difference between calculation and measured values could be observed above 800 K. For USi_3, the calculated C_p and measured values (PPMS and database) were certainly agreed each other. The congruent between calculated and measured values, reveal our measurement data is reliable.

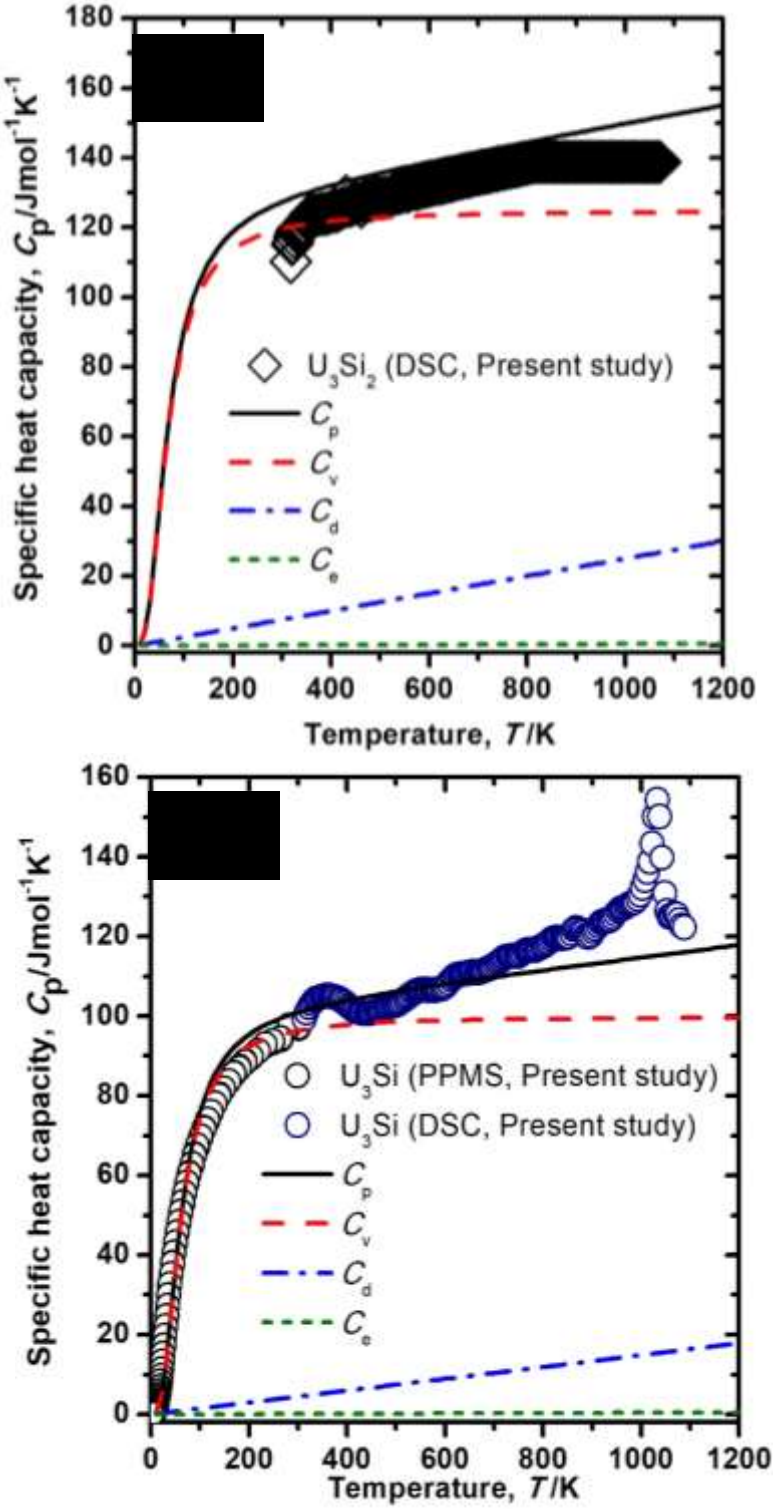

Figure 4.8 Calculated specific heat capacity of (a) U_3Si_2 and (b) U_3Si as a function of temperature. Total specific heat capacity (solid line), lattice vibration term (dash line), dilational term (dash dot line), and electronic term (short dash line) are plotted together.

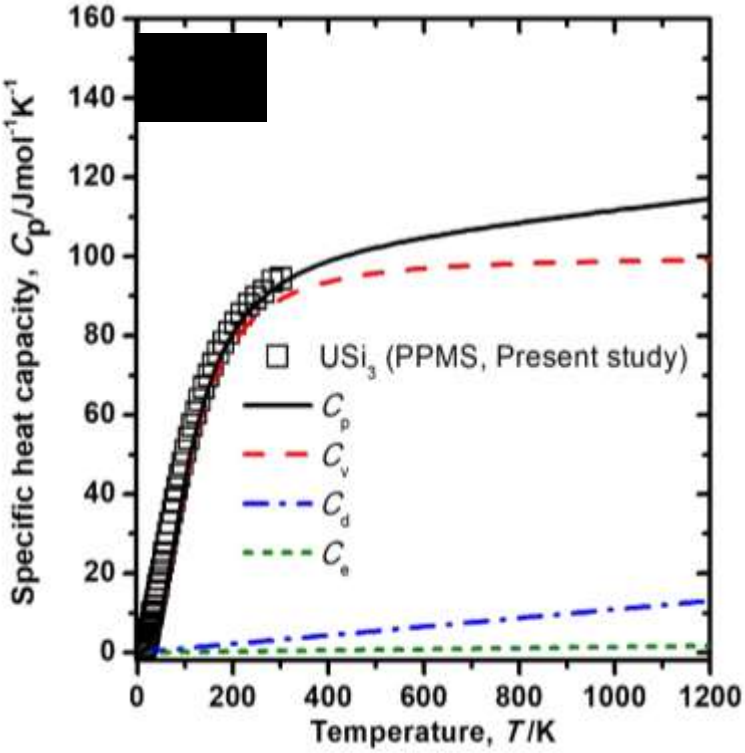

Figure 4.8 (c) Calculated Specific heat capacity of USi_3 as a function of temperature. Total specific heat capacity (solid line), lattice vibration term (dash line), dilational term (dash dot line), and electronic term (short dash line) are plotted together.

From the relationship of thermal diffusivity, specific heat capacity and density, thermal conductivity can be evaluated. This relationship can be written as:

$$\lambda = D \cdot \rho \cdot C_p \tag{3.4}$$

The thermal conductivity of U_3Si_2, U_3Si, and USi_3 are presented in Figure 4.9 (a, b, c). The thermal conductivity of U_3Si_2 increased with increasing temperature. Our measured data is closed with the reported values of White et al. and Shimizu et al. [62, 92]. However, the thermal conductivity of induction cast specimen, that also described by Shimizu's report was lower than others [92]. This

is due to the cracking exist in the specimen where the porosity could lead to the decreased of the thermal conductivity.

In addition, the thermal conductivity of U_3Si increased with increasing temperature to 1050 K. Such temperature dependent behavior is typically observed in metals, suggesting that U_3Si and U_3Si_2 are metallic material. Typically, for the metallic material, the electronic contribution will dominant at high temperature due to the increased of electrical conductivity with temperature. Above 1050 K, thermal conductivity abruptly decreased and increased again. This phenomenon is ascribed as phase transformation. The measured value of U_3Si was closed with Hasting's reported values [95]. However, White's reported value was slightly higher than our data [64]. The specific heat capacity reported by White's (Fig. 4.9 b) is higher than present study, significantly influence calculation values of thermal conductivity.

For USi_3, with increasing temperature the thermal conductivities are decreased, which is a typical behavior for semiconductors and insulators. Generally, the phonon-phonon scattering effect will dominant at high temperature, which lead to the decreased of thermal conductivity with increasing temperature. This seems to be reasonable since USi_3 is a Si-rich compound compared to U_3Si. For USi_3, thermal conductivity measured from the present study was significantly higher than other values described by Yanov et al. [96] and Brixnel et al.[97]. Yanov's data shown in the Fig. 4.9 (c) was the value of arc-melted specimen. There is possibility the prepared of arc melted sample as reported by Yanov et al. has low density, thus porosities in the sample might reduce the thermal conductivity of the measured specimen. Brixnel et al. determined the thermal conductivity with a steady state method. As this method, the surface area of the specimens influences the obtained values, we suggest that the large surface area of specimens reduce the thermal conductivity as reported. The size of the prepared specimen is 19 mm diameter and 25 mm long.

In the Figure 4.9 (d), the thermal conductivities of U_3Si, USi_3, U_3Si_2, USi [66], U_3Si_5 [65], are lists together for the comparison. Among U-Si compounds, USi_3 possess highest thermal conductivity follow by U_3Si, U_3Si_2, USi, and U_3Si_5. The Si thermal conductivity is also plotted together in the Fig 4.9 (d). USi_3 show the same behavior of decreased thermal conductivity with increasing temperature [98]. Thus, this result suggested that USi_3 generate semiconductor behavior same as Si. In addition, the rich Uranium content of U_3Si thermal conductivity is closed with the U metal thermal conductivity [99]. Others compound such as U_3Si_2, USi, and U_3Si_5 exhibit metallic material due to the increased of thermal conductivity with increasing temperature. Thermal conductivities with temperature dependence of UO_2 is also lists together in Fig. 4.9 (d). UO_2 thermal conductivity was decreased with increasing temperature UO_2 [100]. In addition, UO_2 thermal conductivity was the lowest from 700 to 1500 K, compared with others materials that lists in the Fig 4.9 (d).

The phenomena of thermal conductivity of U_3Si, U_3Si_2, USi, U_3Si_5 contribute to the electronic contribution. The correlation between thermal conductivity at 300 K with U/Si ratio is plot as shown in the Figure 4.9 (e) to estimate the electrical contribution in these compounds.

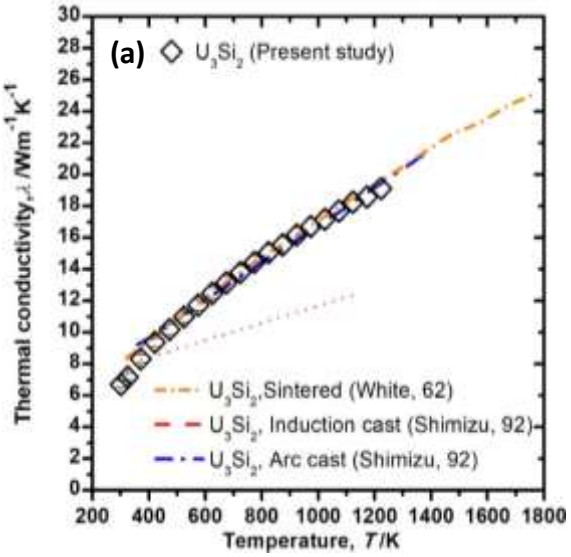

Figure 4.9 Thermal conductivities of (a) U_3Si_2 a function of temperature.

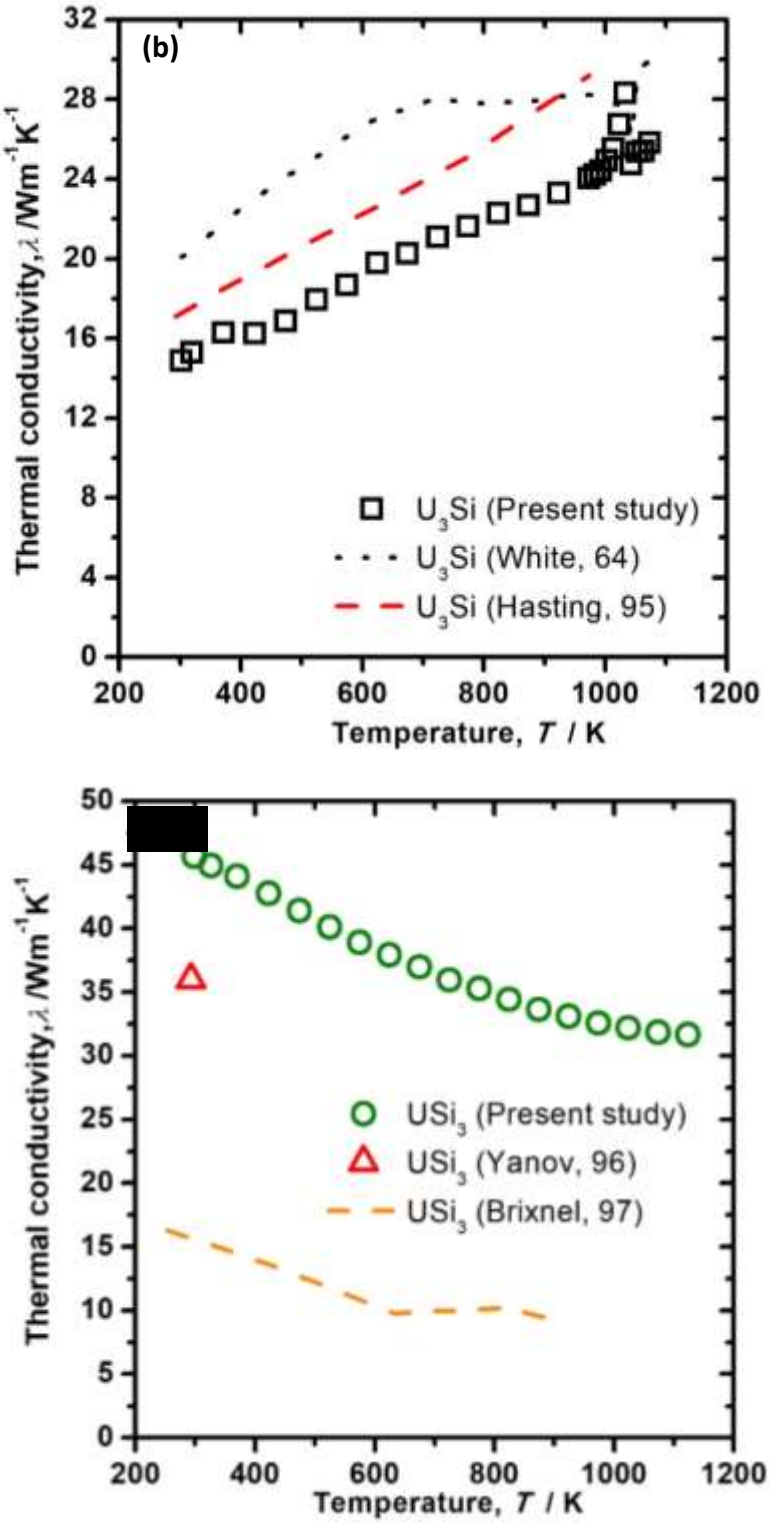

Figure 4.9 Thermal conductivities of (b) U_3Si and (c)USi_3 as a function of temperature.

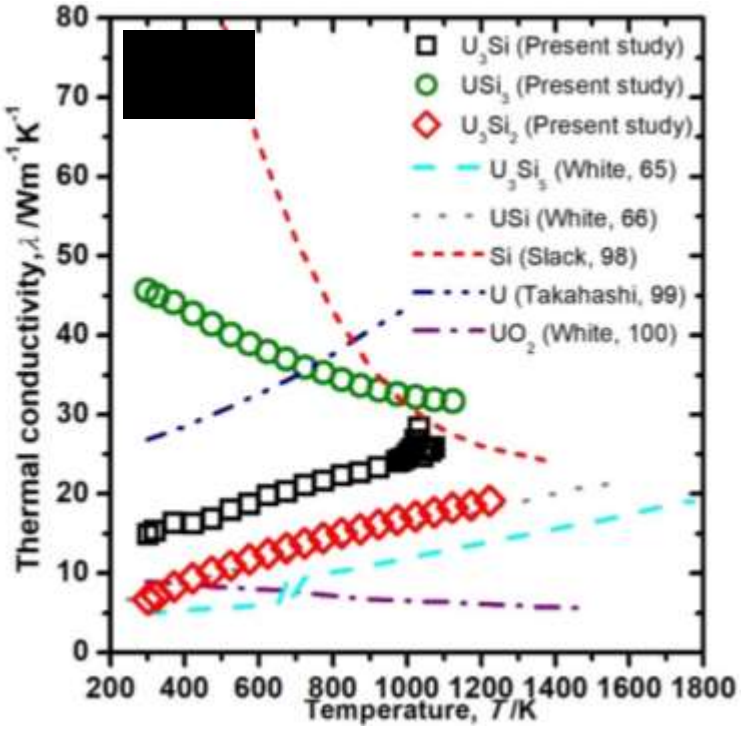

Figure 4.9 (d) Thermal conductivities of U-Si compounds together with UO_2, Si, and U as a function of temperature.

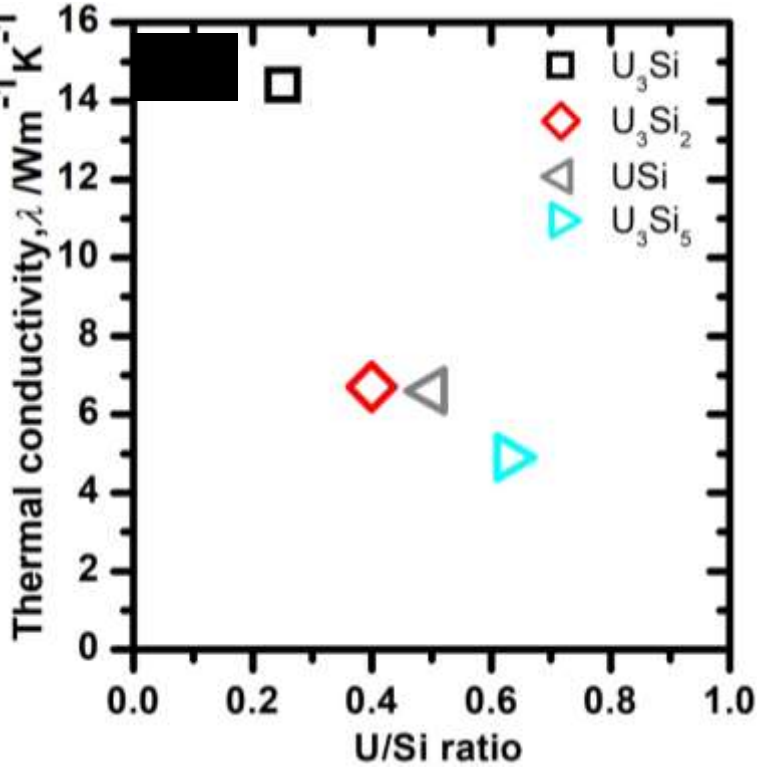

Figure 4.9 (e) Thermal conductivities of U-Si compounds as a function of U/Si ratio.

The higher thermal conductivity is observed for the higher uranium content. With decreasing U ratio in Si, the thermal conductivities are decreased. This phenomena attribute to the electronic contribution. The electronic contribution relationship with thermal conductivity can be expressed with Wiedemann-Franz Law:

$$\lambda_{ele} = L\sigma T \tag{3.5}$$

where σ is the electrical conductivity, L is the Lorenz number and T is the temperature. From this equation, the electrical thermal conductivity is proportional to the electrical conductivity. Thus, the phenomena of thermal conductivity with temperature dependence showed by these compounds attribute to the increase of electrical conductivity which is constant with the phenomena showed by the metallic material.

4.4.4 Desired compounds

From the thermophysical properties explain in the section 4.4.2 and 4.4.3, the desired compounds are selected based on the important parameters such as uranium density, specific heat capacity, and thermal conductivity. Our investigation suggested that U_3Si_2 and USi_3 exhibit promising properties among other compounds exist in U-Si system. This is due to the U_3Si and U_3Si_5 show the phase transformations are observed from the thermal properties, which is not favour for utilize in reactor. As U_3Si_2 own second highest Uranium density in U-Si system, in the other hand, also higher thermal conductivity, this compound might be good candidate for ATF. Surprisingly, rich Si content of USi_3, also show a good behaviour as ATF candidate. Considering very high thermal conductivity of USi_3 in U-Si system, and own same fissile density of Uranium with UO_2 resulted from this compound, make this compound also become one of the desire candidate for ATF. Thus, from the measured thermophysical properties of U_3Si, U_3Si_2, and USi_3,

together with reported data of U_3Si_5 and USi, we found that U_3Si_2 and USi_3 exhibit promising properties among others.

4.4.5 Thermal stress

During reactor operation, thermal conductivity of Uranium dioxide is very low, there is large thermal gradient in UO_2 pellet, causing high centreline temperature, and introducing thermal stress, which lead to extensive fuel pellet cracking. The thermal stress of the pellet can be defined as:

$$\sigma_t = \frac{E\alpha q}{16\pi\lambda(1-v)} \tag{3.6}$$

where, α is the average thermal expansion coefficient at 1000 K [K^{-1}], q is the linear heat rate [W/m], λ is the integrated thermal conductivity from 300 to 1000 K [W/mK], E is the Young's modulus [GPa] and v is the Poisson's ratio determined from this study at room temperature. The q value used for this calculation is the value of linear heat rate of fuel operated under normal operation which is 30000 W/m. The estimated thermal stress of U_3Si_2 and USi_3 are listed in the Table 4.3 together with the UO_2. The thermal stress of USi_3 is very low if compared to U_3Si_2 and UO_2. The thermal gradient of the fuel can be determined as:

$$\Delta T_{fuel} = T_c - T_s = \frac{q}{4\pi\lambda} \tag{3.7}$$

where T_c is the centreline temperature and T_s is the surface temperature. The calculated value of temperature gradient also listed in the Tab. 4.3. The temperature gradient of UO_2 is larger than U-Si due to the low value of thermal conductivity. The value of thermal conductivity gives a large impact to the thermal gradient of the fuel which contribute to the cracking of the pellet.

Table 4.3 Thermal conductivity, Young's modulus, Poisson's ratio, *LTEC*, and thermal stress of U_3Si_2, USi_3, and UO_2 at elevated temperature.

Material	Thermal conductivity [$Wm^{-1}K^{-1}$]	Young modulus [GPa]	Poisson's ratio	*LTEC* [$\times 10^{-6} K^{-1}$]	Thermal stress [MPa]	ΔT [K]
U_3Si_2	17.7	151	0.2	16.1	69	139
USi_3	32.2	231	0.2	11.0	39	74
UO_2	3.3	205	0.3	10.5	345	708

Chapter 5

Conclusions

The present study has investigated a new silicide-based material for the accident tolerant fuel. For the candidate assessment, the selected candidate's materials behaviour performances were focussed in present study. First, we proposed a new material for replace Zr alloy cladding with Mo alloy. As the challenging to utilize Mo as cladding material is it could react with steam/oxygen, we suggest a coating on the outer surface of the Mo cladding with $MoSi_2$ might improve the reaction. As the beginning stage of the development of $MoSi_2$ as coating material on Mo, (i) oxidation resistance of $MoSi_2$ under steam atmosphere (ii) compatibility of both compounds such as thermal stress are investigated. The TG analysis shows no reaction is observed for the $MoSi_2$ when exposed to the steam at 1100 ℃ within 90 minutes. If compared with Zry, the oxidation resistance of $MoSi_2$ is better than Zry. Moreover, the value of the thermal stress between Mo-$MoSi_2$ is 188 MPa, which is promising than well-known candidates such as FeCrAl and Cr. From this evaluation, $MoSi_2$ show an excellent property as a coating material. For the $MoSi_2$-Mo system, a coating method such as chemical and physical vapour deposition and plasma spray can be considered for the manufacturing.

Secondly, for the fuel, U-Si system was selected to replace UO_2. The reliable data on the basic properties of U-Si system is necessary due to the many variables and scarcely data. The basic properties such as thermal and mechanical properties of U-Si compounds were evaluated. We

found that, the highest Si ratio in U/Si system exhibit large atomic bonding from the Young's modulus and thermal expansion coefficient evaluation. In addition, U_3Si_2 had the highest hardness among others might be due to the highest melting point own by it. The thermal conductivity of U-Si system shows only USi_3 exhibit as semiconductor behaviour while U_3Si, U_3Si_2, USi, and U_3Si_5 exhibit as metallic behaviour. The U-Si system compounds show higher thermal conductivity above 700 K if compared to that the current UO_2.

Thirdly, for the fuel selection in U-Si system, we found that U_3Si_2 and USi_3 exhibit excellent properties among other compounds in U-Si system. This is due to the U_3Si_2 possess high uranium density, thermal conductivity, and fracture toughness compare to UO_2. The most surprisingly, not well-known rich Si content of USi_3 also show excellent properties of thermal conductivity and toughness. In our investigation, we found that U_3Si_2 and USi_3 exhibit excellent criteria as candidate for ATF advanced fuel. Then, the thermal stress value is determined to estimate the cracking of the pellet. UO_2 thermal stress is higher than U-Si due to the low value of thermal conductivity. This investigation suggest that the value of thermal conductivity give a large impact to the cracking of the pellet.

Definitely, uranium density of U_3Si_2 was higher than UO_2 which become advantage in term of the economy impact as well as retention of the fission product. In addition, the thermal conductivity as the main key for the fuel, show the thermal conductivity of U_3Si_2 and USi_3 are higher than current fuel of UO_2. A higher thermal conductivity is necessary to reduce the thermal gradient in fuel; which become origin to the centreline temperature. A pellet cracking might be preventing if higher thermal conductivity of fuel was selected.

Thus, in Ph.D. dissertation, I would like to propose a new concept of silicide based of $MoSi_2/Mo/U_3Si_2$ or $MoSi_2/Mo/USi_3$ system concepts for the accident tolerant fuel. Of course,

there are many different ATF concepts that was suggested from others, but it is not possible to consider all of them to a level of reactor testing. This will allow greater-down selection in other to prioritise resources for the further development.

Fukushima (Problem)	Approach-Enhance ATF	Clarification
(1) Rapid oxidation of Zry cladding under steam ○ Degradation occur	**Replace with Mo cladding** 1) The mechanical properties better than Zry 2) Stability under irradiation **Problem** 1)React with oxygen/steam • Coating with $MoSi_2$ 2) High neutron absorption cross-section • Select high uranium density of fuel	• Good oxidation resistance under steam compared to Zry • Thermal stress between Mo-$MoSi_2$ is promising (188 MPa)
(2) Low thermal conductivity of UO_2 ○ Large temperature gradient, which introducing thermals stress and lead to the pellet cracking	**Replace with U-Si** 1)Higher uranium density 2)Higher thermal conductivity **Problem** 1)Variables and scarcely of data in U-Si system • Obtained a reliable data for the basic properties of U-Si compounds	U_3Si_2 and USi_3 exhibit as the most desire candidate among others • Higher thermal conductivity • Higher uranium density • Higher fracture toughness • Resistance to cracking

References

1. P. Y. Lipscy, K.E. Kushida, T. Incerti, Environmental science & technology, **47-12** (2013) 6082-6088.
2. R. M. D. Powers, U. S. NRC report NUREG-0630, 1980.
3. S. J. Zinkle, K. A. Terrani, J. C. Gehin, L. J. Ott, L. L. Snead, Journal of Nuclear Materials, **448** (2014) 374-379
4. B. J. Lewis, E.N.Onder, A. Andrew, Fundamentals of Nuclear Engineering, John Wiley & Sons, March 2017.
5. L. Braase, Enhanced Accident Tolerant LWR Fuels-National Metrics Report, January 2013
6. S. Bragg-Sitton, B. Merrill, M. Teague, L. Ott, K. Robb, M. Brown, U. S. DOE LWR ATF Performance Metrics Report, 2014
7. K. A. Terrani, L. L. Snead, J. C. Gehin, Journal of Nuclear Materials, **427** (1-3) (2012) 209-224.
8. B. A. Pint, K. A. Terrani, M. P. Brady, T. Cheng, J. R. Keiser, Journal of Nuclear Materials, **440** (1-3) (2013) 420-427.
9. J. V. Cathcart, R. E. Pawel, R. A. McKee, R. E. Druschel, G. J. Yurek, J. J. Campbell, S. H. Jury, ORNL/NUREG-17, Oak Ridge National Laboratory**, (**1977).
10. G. A. Rankin, H. E. Merwin, Journal American Ceramic Society, **38 (**1916) 568.
11. A. Kawabata, M.Yoshinoka, K. Hirota, O. Yamaguchi, Journal American Ceramic Society, **78 (**1995) 2271.
12. I. A. Aksay, J. A. Pask, R. F. Davis, Journal American Ceramic Society, **62** (7-8) (1979) 332-336.
13. C .R .F Azevedo, Engineering Failure Analysis, **18** (2011) 1943-1962.
14. A. T. Nelson, E. S. Sooby, Y. J. Kim, B. Cheng, S. A. Maloy, Journal of Nuclear Materials, **448** (2014) 441-447.
15. J. W. McMurray, R. Hu, S. V. Ushakov, D. Shin, B. A. Pint, K. A. Terrani, A. Navrotsky, Journal Nuclear Material, **492** (2017) 128-133.
16. E. A. Gulbransen, K. F. Andrew, Journal Electrochemical Society, **106** (1959) 94.

17. R. B. Rebak, Nuclear Science Technology, **3** (2017) 34.
18. A. Strasser, J.Santucci, K. Lindquist, W. Yario, G. Stern, L. Goldstein, Technical Report EPRI-NP-2642, (1982).
19. R. E. Stachowski, R. B. Rebak, W. P. Gassmann, J. Williams, Proceeding in TopFuel 2016, (2016).
20. K. A. Terrani, S. J. Zinkle, L. L. Snead, Journal Nuclear Material, **448** (2014) 420-435.
21. F. W. Zok, America Ceramic Society Bulletin, **95** (2016) 22-28.
22. E. J. Opila, R. E. Hann, Journal American Ceramic Society, **80** (1997) 197-205.
23. K. L. Murty, I. Charit, Journal of Nuclear Materials, **383** (1-2) (2008) 189-195.
24. J. Shields, Material and Proceeding, **142** (1992) 28-36.
25. K. Abe, T. Takeuchi, M. Kikuchi, S. Morozumi, Journal Nuclear Material, **99** (1981) 25-37.
26. B. Cheng, P. Chou, Y. J. Kim,Proceeding of Technical Report IAEA-TECDOC-1797, (2016) 66-78.
27. F. D. Gac, J. J. Petrovic, Journal American Ceramic Society, **68** (8) (1985) C 200-201.
28. D. H. Carter, G. F. Hurley, Journal American Ceramic Society, **70** (4) (1987) C 79-81.
29. W. S. Gibbs, J. J. Petrovic, R. E. Honnell, Engineering Science Proceeding, **8** (1987) 645-648.
30. T. Yamada, H. Yamane, Intermetallics, **19** (7) (2011) 908-912.
31. H. E. Dève, C. H. Weber, M. Maloney, Materials Science and Engineering: A, **153**(1) (1992) 668-675.
32. A. K. Vasudévan, J. J. Petrovic, Materials Science and Engineering: A, **155** (1) (1992) 1-17.
33. S. Bose, R. J. Hecht, Journal of Materials Science, **27** (10) (1992) 2749-2752.
34. S. P. Sun, X. P. Li, H. J. Wang, Y. Jiang, D. Q. Yi, Journal of Alloys and Compounds, **652** (2015) 106-115.
35. Y. Chen, T. Hammerschdmidt, D. G. Pettifor, J.X. Shang, Y. Zhang, Acta Materialia, **57** (9)(2009) 2657-2664.
36. M. Nakamura, S. Matsumoto, T. Hirano, Journal of Materials Science, **25** (7) (1990) 3309-3313.
37. T. Dasgupta, A. M. Umarji, Intermetallics, **16** (6) (2008) 739-744.

38. F. Chu, M. Lei, S. A. Maloy, J. J. Petrovic, T. E. Mitchell, Acta Materialia, **44** (8) (1996) 3035-3048.
39. T. B. Douglas, W. M. Logan, Journal of Research of the National Bureau of Standards, **53** (1954) 91-93
40. B. E. Walker, J. A. Grand, R .R. Miller, Journal of Physical Chemistry, **60** (2) (1956) 231-233.
41. W. N. Lindemann, F. A. Z, Electrochemical, **17** (1911) 817-827.
42. J .C. L asjaunias, M. S. Paul, O. Laborde, O. Thomas, J. P. Senateur, R. Madar, Physical Review B, **37** (17) (1988) 10364-10366.
43. C. Krontiras, I. Suni, F. M. Heurle, F. K. LeGoues, R. Joshi, Journal of Physics F: Metal Physics, **17** (9) (1987) 1953.
44. J. W. C. de Vries, A. H. Ommen, Journal of Applied Physics, **64** (2) (1988) 749-752.
45. K. M. Takami, Proceeding The 48th Scandinavian Conference on Simulation and Modelling, (2007).
46. M. Jonson, G. D. Mahan, Physical Review B, **21B** (1980) 4223.
47. I. J. Shon, Z. A. Munir, K. Yamazaki, K. Shoda, Journal of the American Ceramic Society, **79** (7) (1996) 1875-1880.
48. R .K. Wade, J. J. Petrovic, Journal of the American Ceramic Society, **75** (6) (1992) 1682-1684.
49. Y. Harada, M. Morinaga, D. Saso, M. Takata, M. Sakata, Intermetallics, **6** (6) (1998) 523-527.
50. D. E Lawrynowicz, J. Wolfenstine, E. Lavernia, S. R. Nutt, D. Bailey, A. Sickinger, A. M. Hirt, MRS Proceedings, **364** (1994).
51. Y. Lee, J. I. Lee, H.C. No, Nuclear Engineering and Technology, **49** (5) (2017) 1031-1043.
52. J. Carmack, F. Goldner, S. M. Bragg-Sitton, L. L. Snead, Top Fuel 2013, (2013).
53. A. T. Nelson, J. T. White, D. D. Byler, J. T. Dunwoody, J. A. Valdez, K. J. McClellan, Transactions of the American Nuclear Society, **110** (2014) 987-989.
54. S. L. Hayes, , J. K. Thomas, K. L. Peddicord, Journal of Nuclear Materials, **171** (2) (1990) 262-270.
55. W. M. Olson, R. N. R. Mulford, Journal of Physical Chemistry, **68** (5) (1964) 1048-1051.
56. S. Sunder, N. H. Miller, Journal of Alloys and Compounds,. **271-273** (1998) 568-572.

57. R. M. Dell, V. J. Wheeler, E. J. McIver, Transactions of the Faraday Society,. **62** (1966) 3591-3606.
58. Y. Arai, S. Fukushima, K. Shiozawa, M. Handa, Journal of Nuclear Materials, **168** (3) (1989) 280-289.
59. J. L. Snelgrove, Nuclear Engineering and Design,. **178**(1) (1997) 119-126.
60. M. R. Finlay, G. L. Hofman, J. L. Snelgrove, Journal of Nuclear Materials, **325**(2) (2004) 118-128.
61. S. C. Middleburgh, R. W. Grimes, E. J. Lahoda, C. R. Stanek, D. A. Anderson, Journal of Nuclear Materials, **482** (2016) 300-305.
62. J. T. White, A. T. Nelson, J. T. Dunwoody, D. D. Byler, D. J. Safarik, K. J. McClellan, Journal of Nuclear Materials, **464** (2015) 275-280.
63. J. K. Fink, Journal of Nuclear Materials, **279** (1) (2000) 1-18.
64. J. T. White, A. T. Nelson, D. D. Byler, J. A. Valdez, K. J. McClellan , Journal of Nuclear Materials,. **452** (1) (2014) 304-310.
65. J. T. White, A.T.Nelson, D. D. Byler, D. J. Safarik, J. T. Dunwoody, K. J. McClellan, Journal of Nuclear Materials, **456** (2015) 442-448.
66. J. T. White, A.T.Nelson, J. T. Dunwoody, D. D. Byler, K. J. McClellan, Journal of Nuclear Materials, **471** (2016) 129-135.
67. National Metrology Institute of Japan, Certificate of Analysis Standard Reference Material NMIJ RM 1201-a-Isotrophic Graphite for Thermal diffusivity Measurement, 2010.
68. D. R. Lide, CRC Handbook of Chemistry and Physics, 71 ed, CRC Press, Boston, (2016) 1990-1991
69. PDXL No-01-075-1962
70. PDXL No-01-071-356
71. PDXL No-010751957.
72. PDXL No-030653267.
73. K. Remschnig, T. L. Bihan, H. Noel, P. Rogl, Journal of Solid State Chemistry, **97** (2) (1992) 391-399.
74. T. Wang, N. Qiu, X. Wen, Y. Tian, J. He, K. Luo, X. Zha, Y. Zhou, Q. Huang, J. Lang, S. Du, Journal of Nuclear Materials, **469** (2016) 194-199.
75. J. Yang, J. Long, L. Yang, D. Li, Journal of Nuclear Materials, **443** (2013) 195-199.

76. S. F. Pugh, Philosophical Magazine, **45** (7) (1954) 823-843.
77. K. E. Metzger, T. W. Knight, E. Roberts, X. Huang, Progress in Nuclear Energy, **99** (2017) 147-154.
78. R. F. Domagala, T.C.W., H. R.Thresh, Proceeding International Metallurgy on Reduced Enrichment for Research and Test Reactors, (1984) 47-60.
79. U.C. Nunez, M. S. Elbakhshwan, N. A. Mara, J. T. White, A. T. Nelson, Journal Of Materials, **70** (2) (2018) 203-208.
80. A. K. Sengupta, C. B. Basak, T. Jarvis, R. K. Bhagat, V. D. Pandey, S. Majumdar, Journal of Nuclear Materials, 325 (2004)141-147.
81. J. Adachi, K. Kurosaki, M. Uno, S. Yamanaka, M. Takano, M. Akabori, K. Minato, Journal of Nuclear Materials, 384 (2009) 6-11.
82. F. C. Campbell, ASM International, Materials Park, United States of America, 2012.
83. K. S. Ravichandran, *Fracture Resistance of Structural Alloys* ASM Handbook, (1996) 381-392.
84. L. L. D. Loch, G. B. Engle, M. J. Snyder, W. H. Duckworth, *Technical Report BMI-1124, August 1956.*.
85. K. M. Taylor, C. H. McMurty, Technical Report ORO-400, February 1961.
86. V. A. Makhova, L. I. Gomozov, Soviet Atomic Energy, **33** (5) (1972) 1069-1072.
87. Y. Okada, Y. Tokumaru, Journal of Applied Physics, **56**(2) (1984) 314-320.
88. R. E. Taylor, J. A. Cape, Technician Report AD-255894, April 1961.
89. O. Knacke, O. Kubaschewski, K. Hesselmann, Thermochemical properties of inorganic substances, Springer, Berlin Heilderberg, (1991) 1-2541.
90. G. Kimmel, B. Sharon, M. Rosen, Acta Crystal, **B36** (1980) 2386-2389.
91. J. Snelgrove, R. D. Graham, G. Hofman, T. Wiencek, G. Copeland, R. Hobbs, R. Senn, Technical Report ANL/RERTR/TM-11, Argonne National Laboratory, (October 1987).
92. H. Shimizu, Technical Report NAA-SR-10621, (July 1965).
93. H. Flotow, D. W. Lyon, F. Grandjean, D. Fredrickson, I. Hastings, Journal of Chemical Thermodynamics, 9 (5) (1977) 473-481.
94. Database, (www.factsage.com).
95. J. Hastings, J. R. Macewan, L. R. Bourque, Journal of the American Ceramic Society, 55 (1972) 240-242.

96. V. S. Y. Yanov, A. l. Yevstyukhin, The Metallurgy of Nuclear Fuel ,Properties and Principles of the Technology of Uranium, Thorium and Plutonium:1st Edition, (1969) 164.
97. L. H. Brixner, Journal Inorganic Nuclear Chemistry, 25 (1963) 783-787.
98. C. J. Glassbrenner, G. A. Slack, Physical Review, 134 (1964) A1058-A1069.
99. Y. Takahashi, M. Yamawaki, K. Yamamoto, Journal of Nuclear Materials, 154 (1988) 141-144.
100. G. K.White, F. W. Sheard, Journal of Low Temperature Physics, 14 (1974) 445-457.

Acknowledgements

I would like to expressed my appreciation to Professor Emeritus Shinsuke Yamanaka for beneficial advices, informative support, guidance and priceless suggestion on my Ph.D. study. I am grateful to Dr. Ohishi Sensei to lend me support, guidance, and fruitful discussion for my Ph.D. study within 3 years. I can't admit that he guides me from A to Z in nuclear field. Also not forgot Professor Hiroaki Muta and Professor Ken Kurosaki for guidance too. My honest thank is to the thesis committee, Professor Takao Yamamoto and Professor Takanori Kitada for their helpful comment and suggestion for my thesis and defend.

I would like to acknowledge my appreciation to Dr. Seongho Choi and Dr. Fumihiro Nakamori who provide helpful advice. Not forget my best international students friend such as Toto, Ploy, Wang, Lin, Yining and Saori for provide support when I need emotional support.

My thankful is also extended for the Malaysian Japan Higher Education Program who provide 3 years' scholarship during my study in Japan. Finally, I would like to thank my family for their great supports in infinite ways.

Achievements

Thesis related journal

1. **Thermal and Mechanical Properties of α-$MoSi_2$ as a high temperature material**
   Physica Status Solidi b, **255**, 1700448 (2017).
   Afiqa Mohamad, Yuji Ohishi, Hiroaki Muta, Ken Kurosaki, and Shinsuke Yamanaka

2. **Thermal and mechanical properties of polycrystalline U_3Si_2 synthesized by spark plasma sintering**
   Journal of Nuclear Science and Technology, 55 (10), 1141-1150 (2018).
   Afiqa Mohamad, Yuji Ohishi, Hiroaki Muta, Ken Kurosaki, and Shinsuke Yamanaka

3. **Thermophysical properties of U_3Si and USi_3**
   Annals of Nuclear Energy (Under review)
   Afiqa Mohamad, Yuji Ohishi, Hiroaki Muta, Ken Kurosaki

Others journal

4. **Thermoelectric Properties of $Cr_{1-x}W_xSi_2$**
   Materials Transactions, 57 (7), 1059-1065 (2016).
   Afiqa Mohamad, Yuji Ohishi, Yoshinobu Miyazaki, Hiroaki Muta, Ken Kurosaki, and Shinsuke Yamanaka

5. **Thermoelectric Properties of $Cr_{1-x}Mo_xSi_2$**
   Journal of Physics and Chemistry of Solids, 87, 153-157 (2015).
   Yuji Ohishi, Afiqa Mohamad, Yoshinobu Miyazaki, Hiroaki Muta, Ken Kurosaki, and Shinsuke Yamanaka

Conferences

Oral:

- **The 12th Thermoelectric Society Japan Conference**, Kyusyu Japan, September 2015, "*Thermoelectric properties of $Cr_{1-x}Mo_xSi_2$*"
- **2016 International Conference Thermoelectric,** Wuhan China, May 2016, *"Thermoelectric properties of congener substitution on $CrSi_2$"*
- **2017 Asia Nuclear Fuel Conference**, Jeju Island South Korea, September 2017, "*Thermal and mechanical properties of U_3Si_2*"
- **2017 Autumn Meeting of the Atomic Energy Society of Japan**, Hokkaido Japan, September 2017, "*Thermal and mechanical properties of U_3Si_2*"
- **2017 Autumn Meeting, Material Research Society, Boston,** USA, November 2017, "*Thermal and mechanical properties of U_3Si_2*"
- **2018 Spring Meeting of the Atomic Energy Society of Japan**, Osaka Japan, March 2018, "Surface analyses of Sr compound onto stainless steel"
- **2018 Autumn Meeting of the Atomic Energy Society of Japan**, Okayama Japan, September 2018, "Chemical interaction of Sr compounds with Zircaloy"
- **2018 Kansai Nuclear Power Plant Meeting,** Osaka, Japan, November 2018, "Preliminary study on the U-Si system compounds as candidates for accident tolerant fuel (ATF)

Poster:

- **2016 International Conference Thermoelectric,** Wuhan China, May 2016, *"Thermoelectric properties of congener substitution on $CrSi_2$"*
- **2017 Fukushima Reactor Conference**, Tomioka Japan, July 2017, *"Thermal and mechanical properties of U_3Si_2"*
- **2018 The Nuclear Materials Conference, Seattle, USA, October 2018** *"Studies on thermal and mechanical properties of tetragonal triuranium silicide prepared by arc melting"*
- **2018 The Nuclear Materials Conference, Seattle, USA, October 2018** *"High temperature chemical reaction of Strontium vapor species with Stainless steel"*

Award:

- Best Oral Presenter Award at Asia Nuclear Fuel Conference 2017
- Best Oral Presenter Award at Atomic Energy Society of Japan Conference, Autumn 2017
- Best Poster Award at Nuclear Material Conference 2018
- Best Oral Presenter at Kansai Nuclear Power Plant Meeting 2018